

## Copyright Warning & Restrictions

The copyright law of the United States (Title 17, United States Code) governs the making of photocopies or other reproductions of copyrighted material.

Under certain conditions specified in the law, libraries and archives are authorized to furnish a photocopy or other reproduction. One of these specified conditions is that the photocopy or reproduction is not to be “used for any purpose other than private study, scholarship, or research.” If a user makes a request for, or later uses, a photocopy or reproduction for purposes in excess of “fair use” that user may be liable for copyright infringement,

This institution reserves the right to refuse to accept a copying order if, in its judgment, fulfillment of the order would involve violation of copyright law.

**Please Note: The author retains the copyright while the New Jersey Institute of Technology reserves the right to distribute this thesis or dissertation**

Printing note: If you do not wish to print this page, then select “Pages from: first page # to: last page #” on the print dialog screen

The Van Houten library has removed some of the personal information and all signatures from the approval page and biographical sketches of theses and dissertations in order to protect the identity of NJIT graduates and faculty.

## ABSTRACT

### MULTI-MODE CAVITY EFFECTS ON THE MICROWAVE HEATING OF A CERAMIC SLAB

by  
Stuart J. Walker

In order to gain insight into hot spot development in microwave heated ceramics, a partially insulated, two dimensional ceramic slab situated in a  $TE_{M01}$  cavity is modeled in the small Biot number limit. If the electrical conductivity is an exponential function of temperature and  $E_0$  is the strength of the incident mode, then the relationship between the spatially uniform, steady state leading order temperature,  $v_s$ , and  $E_0^2$  is characterized by the well known bi-stable, or  $S$  shaped, response curve. The steady state second order temperature,  $v_1$ , is described by a boundary value problem consisting of a Poisson equation with a non linear source term and non linear boundary flux conditions at two of the slab faces; the remaining two slab faces are assumed to be insulated. The source term depends on the electrical conductivity function and the spatially dependent leading order electric field, both of which are parametrized by  $v_s$ . The boundary conditions demonstrate fourth power dependence on  $v_s$  as a result of radiated heat loss. It is the spatial dependence of  $v_1$  that is the source of temperature non-uniformities that can cause deleterious density fluctuations in a sintered ceramic.

The main results are as follows: First, for cavities of increasing width (i.e., increasing  $M$ ) with  $v_s$  chosen on the lower branches of their corresponding  $S$  curves where the  $TE_{M01}$  mode remains dominant, it is shown that detuning of the cavity is the primary reason for the decrease of electric field strengths from their initial resonant values. For  $v_s$  values chosen on the upper branches of the  $S$  curves where the  $TE_{M01}$  mode ceases to be dominant, it is demonstrated that skin effect shielding is the primary reason for the decrease of electric field strengths, while cavity detuning

plays a secondary role as evidenced by the distortion of the electric field pattern. This distortion results from the prominent influence of other field modes.

Secondly, it is shown that, for lower branch values of  $v_s$ , the dominant  $TE_{M01}$  mode determines a similar sinusoidal mode structure for  $v_1$ . As the value of  $M$  increases for  $M \geq 3$ , the steady state second order temperature transitions from a state in which its double maxima are located near the insulated edges of the slab for  $M = 3$  to a state in which a single maximum is located in the center of the slab for  $M \geq 7$ . Preliminary data indicate that this trend is not observed for upper branch  $v_s$  values due to the unpredictable behavior of the electric field. Finally, data are presented which suggest a trend toward uniformity of temperature for lower branch  $v_s$  values. This supports the experimental observation that the temperature of a microwave heated object becomes more uniform as the number of electric field modes propagating within the object increases.

**MULTI-MODE CAVITY EFFECTS ON THE MICROWAVE  
HEATING OF A CERAMIC SLAB**

by  
**Stuart J. Walker**

**A Dissertation  
Submitted to the Faculty of  
New Jersey Institute of Technology  
and Rutgers, The State University of New Jersey-Newark  
in Partial Fulfillment of the Requirements for the Degree of  
Doctor of Philosophy in Mathematical Sciences**

**Department of Mathematical Sciences  
Department of Mathematics and Computer Science, Rutgers-Newark**

**January 2001**

Copyright © 2001 by Stuart J. Walker

ALL RIGHTS RESERVED

**APPROVAL PAGE**

**MULTI-MODE CAVITY EFFECTS ON THE MICROWAVE HEATING OF A  
CERAMIC SLAB**

**Stuart J. Walker**

---

Dr. Gregory A. Kriegsmann, Dissertation Advisor Date  
Distinguished Professor, Department of Mathematical Sciences, NJIT

---

Dr. David C. Stickler, Committee Member Date  
Professor, Department of Mathematical Sciences, NJIT

---

Dr. Jonathan H. C. Luke, Committee Member Date  
Associate Professor, Department of Mathematical Sciences, NJIT

---

Dr. Peter G. Petropoulos, Committee Member Date  
Associate Professor, Department of Mathematical Sciences, NJIT

---

Dr. Edip Niver, Committee Member Date  
Associate Professor, Electrical and Computer Engineering Department, NJIT

## BIOGRAPHICAL SKETCH

**Author:** Stuart J. Walker  
**Degree:** Doctor of Philosophy  
**Date:** January 2001

### Undergraduate and Graduate Education:

- Doctor of Philosophy in Mathematical Sciences  
New Jersey Institute of Technology, Newark, NJ, January 2001
- Master of Science in Applied Mathematics  
University of Illinois at Chicago, Chicago, IL, May 1994
- Bachelor of Arts in Mathematics  
Northwestern University, Evanston, IL, June 1987

**Major:** Applied Mathematics

### Presentations and Publications:

- C. Bouton, S. Walker, R. Wieman, D. Xu, A. Minut and C. Peterson,  
*“Modeling compton scattering and photoelectric absorption of x-rays in media containing heavy elements,”*  
Proceedings of the Fifth Industrial Mathematics Modeling Workshop for Graduate Students, Center for Research in Scientific Computation Technical Report no. 17, North Carolina State University, Raleigh, NC, pp. 8-17, May 2000.
- G. Kriegsmann and S. Walker,  
*“Multi-mode cavity effects on the microwave heating of a ceramic slab,”*  
Journal of Engineering Mathematics, in preparation, May 2001.

To Bo and Uncle Raymond for their wisdom and foresight  
    To Mom for her unwaivering faith  
    To Aunt Lee for her absolute confidence in destiny  
To Dad for his unbridled enthusiasm in life and learning  
    To Heather for her loving patience and companionship  
    And to those who said “Just do it!”

## ACKNOWLEDGMENT

I would like to express my most sincere gratitude to Professor Gregory A. Kriegsmann for his inspiration, his boundless enthusiasm, his patient encouragement and his sage advice. He not only taught me valuable lessons about how to answer scientific questions, but, just as importantly, about how to ask them. I would also like to thank each of my committee members, Dr. David C. Stickler, Dr. Jonathan H.C. Luke, Dr. Peter G. Petropoulos and Dr. Edip Niver for their thoughtful insights and suggestions. Special thanks are due to Dr. Lambert Feher for his review of my dissertation proposal, his thought provoking discussions and his friendship.

I offer a heartfelt thank you to Roseanne Rowan for her friendship, assistance and support. Many of my fellow graduate students, too numerous to name, are also deserving of recognition for their collegiality and advice offered over the years. Finally, I wish to thank all those who came before me.

## TABLE OF CONTENTS

Chapter	Page
1 INTRODUCTION . . . . .	1
2 LITERATURE SURVEY OF METHODS TO DETERMINE CAVITY ELECTROMAGNETIC FIELDS . . . . .	5
2.1 Numerical Approaches . . . . .	5
2.2 Analytical Approaches . . . . .	6
2.3 Recent Developments . . . . .	8
2.3.1 Hybrid Method . . . . .	8
2.3.2 “Gridless” Method . . . . .	9
3 INITIAL-BOUNDARY VALUE PROBLEM FORMULATION . . . . .	10
3.1 Electromagnetic Formulation . . . . .	11
3.2 Thermal Formulation . . . . .	15
3.3 Non-dimensionalization . . . . .	17
4 THERMAL CONSIDERATIONS . . . . .	20
5 ELECTROMAGNETIC CONSIDERATIONS . . . . .	23
5.1 Empty Two Dimensional Cavity . . . . .	23
5.1.1 Boundary Value Problem For Electric Field . . . . .	23
5.1.2 Scattering Matrix Formulation . . . . .	24
5.1.3 Solution of Linear System for Propagating Mode Amplitudes and Resonant Length Determination . . . . .	27
5.2 Slab Loaded Two Dimensional Cavity . . . . .	32
5.2.1 Boundary Value Problem For Electric Field . . . . .	33
5.2.2 Scattering Matrix Formulation for Cavity Electric Field . . . . .	35
5.2.3 Solution of Linear System for Propagating Mode Amplitudes and Resonant Length Determination . . . . .	38
5.2.4 Solution for Leading Order Electric Field in Slab . . . . .	38

**TABLE OF CONTENTS**  
**(Continued)**

<b>Chapter</b>	<b>Page</b>
5.3 Future Work .....	40
5.3.1 Large Cavity Widths ( $a \gg 1$ ) .....	40
5.3.2 Inclusion of Evanescent Modes .....	41
<b>6 SLAB TEMPERATURE AND ELECTRIC FIELD ANALYSIS .....</b>	<b>42</b>
6.1 Analysis of Steady State Leading Order Temperature and its Effect on the Electric Field .....	42
6.1.1 Cases of $M = 1$ and $M = 2$ .....	45
6.1.2 Case of $M \geq 3$ .....	46
6.1.3 Future Work .....	55
6.2 Analysis of Effect of Leading Order Temperature and Electric Field Distribution on Second Order Temperature Distribution. ....	55
6.2.1 Case of $a = 1$ .....	57
6.2.2 Cases of $M \geq 3$ .....	61
<b>APPENDIX A DERIVATION OF REFLECTION AND TRANSMISSION         COEFFICIENTS FOR INFINITE STEPPED WAVEGUIDE .....</b>	<b>72</b>
<b>APPENDIX B DERIVATION OF REFLECTION AND TRANSMISSION         COEFFICIENTS FOR DIELECTRIC CERAMIC SLAB IN INFINITE         WAVEGUIDE .....</b>	<b>79</b>
<b>APPENDIX C SOLUTION OF PARTIAL DIFFERENTIAL EQUATION         FOR SECOND ORDER TEMPERATURE .....</b>	<b>84</b>
<b>REFERENCES .....</b>	<b>91</b>

## LIST OF FIGURES

Figure	Page
3.1 Left: 3-D loaded cavity. Right: 2-D loaded cavity. . . . .	10
3.2 Planar view of 2-D loaded cavity depicting electric field modal amplitudes outside slab and electric field $U$ inside slab. . . . .	11
5.1 Empty 2-D cavity depicting propagating modal amplitudes. . . . .	25
5.2 Electric field pattern in $TE_{103}$ cavity with $l = l_r^{max} = 2.0863$ . . . . .	28
5.3 Electric field pattern in $TE_{103}$ cavity with $l = l_r^{min} = 2.4872$ . . . . .	29
5.4 $M = 3$ : Mode amplitudes vs. cavity length near resonant maximum length, $l_r^{max} = 2.0982$ . . . . .	31
5.5 Dominant $TE_{301}$ mode for $l_r^{max} = 2.0982$ . . . . .	31
5.6 $M = 3$ : Mode amplitudes vs. cavity length near resonant minimum length, $l_r^{min} = 2.0944$ . . . . .	32
5.7 Dominant $TE_{103}$ mode for $l_r^{min} = 2.0944$ . . . . .	32
5.8 Two dimensional configuration depicting propagating modal amplitudes in the cavity and modal amplitudes in the slab. . . . .	34
6.1 $S$ curves for $TE_{103}$ cavities of increasing width when $M = 1, 2$ . . . . .	44
6.2 $S$ curves for $TE_{103}$ cavities of increasing cavity width when $M = 2$ . . . . .	44
6.3 Cross sectional illustration of skin effect on electric field within a slab of width $a = 1$ heated to a steady state temperature $v_s = 12$ on the upper branch of the $S$ curve shown in Figure (6.1). . . . .	46
6.4 $S$ curves for $TE_{J01}$ cavities with $J = M$ . . . . .	47
6.5 $S$ curves of Figure (6.4) near origin. . . . .	47
6.6 Contour plot of magnitude of leading order electric field in loaded lossless $TE_{901}$ cavity. Slab edges at $z = q = 3.0185$ and $z = q + d = 3.4895$ . $l = l_r^{max} = 6.520$ and $a = 6.0369$ . . . . .	48
6.7 Contour plot of magnitude of leading order electric field in loaded $TE_{301}$ cavity with $v_s = 10$ . Slab edges at $z = q = 1.0541$ and $z = q + d = 1.5226$ . $l = l_r^{max} = 2.5225$ and $a = 2.1082$ . . . . .	52
6.8 Three dimensional version of Figure (6.7). . . . .	52

<b>Figure</b>	<b>Page</b>
6.9 Contour plot of magnitude of leading order electric field in loaded TE <sub>301</sub> cavity with $v_s = 2$ . Slab edges at $z = q = 1.0541$ and $z = q + d = 1.5226$ . $l = l_r^{max} = 2.5225$ and $a = 2.1082$ . . . . .	53
6.10 Three dimensional version of Figure (6.9). . . . .	53
6.11 Magnitude of leading order electric field in lossy slab of Figures (6.7) and (6.8) with $v_s = 10$ . . . . .	54
6.12 Electric field strength within a slab of width $a = 1$ heated to a steady state temperature $v_s = .5$ on the lower branch of the $S$ curve shown in Figures (6.1) and (6.4). . . . .	58
6.13 Second order temperature, $v_1$ , corresponding to Figure (6.12). . . . .	58
6.14 Three dimensional version of Figure (6.13). . . . .	59
6.15 Electric field strength within a slab of width $a = 1$ heated to a steady state temperature $v_s = 12$ on the upper branch of the $S$ curve shown in Figures (6.1) and (6.4). . . . .	60
6.16 Second order temperature corresponding to Figure (6.15). . . . .	60
6.17 Magnitude of leading order electric field in slab for $M = 3, a = l_{cc} = 2.1082, v_s = 2$ . . . . .	62
6.18 Three dimensional version of Figure (6.17). . . . .	63
6.19 Second order temperature in slab for $M = 3, a = l_{cc} = 2.1082, v_s = 2$ . Maxima are located at $Zslab = 1.29, Xslab = \pm .65$ . . . . .	64
6.20 Three dimensional version of (6.19). . . . .	64
6.21 Cross section of (6.20) in $v_1$ -Xslab plane. . . . .	65
6.22 Magnitude of leading order electric field in slab for $M = 3, a = l_{cc} = 2.1082, v_s = 10$ . Maxima are located at $Zslab = 1.08, Xslab = \pm .50$ . . . . .	66
6.23 Second order temperature in slab for $M = 3, a = l_{cc} = 2.1082, v_s = 10$ . Maxima are located at $Zslab = 1.19, Xslab = \pm 1.0$ . . . . .	66
6.24 Three dimensional version of Figure (6.23). . . . .	67
6.25 Cross section of Figure (6.27) in $v_1$ -Xslab plane. . . . .	68
6.26 Cross section of leading order electric field magnitude in $ u_0 $ -Xslab plane for $M = 5$ . . . . .	68
6.27 Second order temperature in slab for $M = 5, a = l_{cc} = 3.3993, v_s = 2$ . . . . .	69
6.28 Second order temperature in slab for $M = 7, a = l_{cc} = 4.7140, v_s = 2$ . . . . .	70

<b>Figure</b>	<b>Page</b>
A.1 Infinite stepped waveguide junction. A: Incident wave from left. B: $j^{th}$ incident wave from right. . . . .	72
B.1 Ceramic slab in infinite waveguide of uniform width. A: incident wave from left. B: incident wave from right. . . . .	79

# CHAPTER 1

## INTRODUCTION

The word *ceramic* derives from the Greek *keramos* and Latin *cremare* meaning “to burn” and is notoriously difficult to define concisely. In general a ceramic has been defined as any inorganic or non-metallic material rendered hard and heat resistant by heating at temperatures of 1000 degrees Fahrenheit or above. Most ceramics consist of complex oxides and silicates although there are several exceptions including carbon itself due to its highly refractory nature[1]. For our purposes, it will be sufficient to define a ceramic as a material suitable for heat processing and characterized by a low thermal conductivity.

The ever increasing demand for specialized ceramic materials in the industrial and high tech worlds has initiated investigation into more effective methods for creating them. To this end microwave and millimeter wave heating of ceramics has become the subject of experimental and theoretical research with a goal to design applicators suitable for the effective processing of ceramics in accordance with stringent industrial specifications. In order for the desired processing method to be effective, it is necessary to heat the sample within an applicator such that temperature gradients within the material are controlled. For example, joining of ceramics requires localized heating (and often melting) at the interface; in contrast, sintering, a firing process which increases a ceramic's density by increasing grain size and decreasing porosity without melting, requires uniform heating in an attempt to minimize significant density fluctuations and subsequent structural weakening of the sample as it contracts[2].

In order to achieve more uniform heating, the volumetric nature of micro- and millimeter wave sintering has made it preferable to conventional sintering, in which heat diffuses from the sample surface inward, often resulting in deleterious density fluctuations. Furthermore, the typically low thermal conductivities of ceramics

demand much more time to reach thermal equilibrium by conventional sintering than by micro- or millimeter wave sintering. Ayappa et al. report that experiments have shown densification and densification rates for certain ceramics are greater when using microwave sintering as compared to conventional sintering. In order to compare densification and grain growth predicted for microwave sintering with those predicted by conventional sintering, they numerically solve the evolution equations for grain growth and porosity developed in [3] for the late stages of sintering coupled to the heat and time harmonic electric field equations in one dimensional ceramic slabs composed of  $\text{Al}_2\text{O}_3$  and SiC respectively. They fix the slab thickness and control the heat flux at the slab surface so as to establish a small convective Biot number regime in which the time scale for heat convection is much greater than that for heat diffusion. This situation approximates a sintering technique in which a lossy material such as SiC is used as a susceptor or lining to indirectly heat a low loss material such as  $\text{Al}_2\text{O}_3$ . The SiC insulates the low loss material, thereby reducing the effects of non uniform heating.[4] Unfortunately, even with a volumetric heat source, this sintering process evolves on the long convective time scale, which exacerbates the computational requirement of a numerical simulation [7].

In a systematic effort to understand the governing physics of microwave heating of ceramics on the macroscopic level, Kriegsmann has conducted small Biot number asymptotic analyses of the coupled non-linear system of the time harmonic electric field equation and the heat equation for (1) an infinite one dimensional ceramic slab of finite thickness on the order of a slab wavelength located in free space[5] and (2) for a two dimensional slab of similar thickness situated in a  $\text{TE}_{103}$  applicator with adjustable iris [7]. By avoiding extensive numerical computation in his analysis, he is able to conduct parameter studies efficiently in order to observe trends and to analytically establish functional relationships between various geometrical, thermal and electrical quantities.

In case (1), he offered a plausible explanation for the catastrophic phenomenon of thermal runaway in which a sample's temperature can rapidly increase to its melting point for a slight increase in the microwave power level. For an exponential electrical conductivity function, he deduced a bistable (S-shaped) response curve relating the leading order steady state slab temperature to the incident power. This steady state is achieved when the power generated within the slab balances the power lost at the surfaces. In particular, the existence of the upper branch of the curve was attributed to the skin effect wherein the interior of the slab is shielded from the microwaves, thereby quenching the electric field in the sample. Temperatures residing on this upper branch are potentially high enough to cause melting of the ceramic.

In case (2), he again obtained a bistable response curve and demonstrated how the shape of the curve depends upon the coupling of the microwave to the cavity and upon the effect of the subsequent heating on this coupling. By considering various aperture sizes, he showed that for large aperture openings, the shape of the S-curve is similar to that for case (1) with the existence of the upper branches again due to skin effect shielding, while for certain smaller openings, the upper branches are the result of cavity detuning as opposed to the skin effect.

The non linear nature of the heating process creates temperature non uniformities or hot spots within a sample. The location and intensity of these hot spots depend on the incident power level, the geometry of the cavity, and the geometrical, thermal and electrical properties of the sample. The primary focus of our study will be to investigate the development of these hot spots within a rectangular ceramic slab situated in a  $TE_{M01}$  cavity by conducting a small Biot number asymptotic analysis of the governing thermal-electric system of equations. Specifically, we will investigate the effects of varying cavity dimensions on the second order temperature distribution. While the leading order temperature is spatially uniform, it is the second

order temperature that exhibits spatial variations. These spatial variations cause temperature non uniformities, which can lead to inhomogeneities in the material properties of a sintered ceramic. As an aid to our analysis, we will also investigate the effects of cavity detuning and skin effect shielding on the shape of the bistable response curves and the implications these phenomena have for second order spatial temperature variation. We choose a two dimensional cavity as a compromise between the simpler single mode  $TE_{103}$  cavity considered by Kriegsmann and a more complicated fully three dimensional cavity. The two dimensional version supports many more modes than the single mode cavity and provides insight into the effects of these higher order modes that are present in more realistic situations.

The outline of the remainder of this dissertation is as follows: In chapter 2 we present a survey of analytical and numerical methods that have been used in the past to obtain electromagnetic field distributions within dielectric-loaded single and multi-mode cavities. This serves as a basis for comparison with the method used in this study for electromagnetic field determination. In chapter 3 we formulate the microwave heating problem for a low loss ceramic slab in a  $TE_{J0n}$  cavity where the integer  $J$  specifies the mode number with respect to cavity width and  $n$  the mode number with respect to cavity length. Next, an asymptotic approximation for the temperature and electric field distributions within the slab, as the Biot number goes to zero, is developed in chapter 4. In chapter 5 we find the leading order electric fields in the cavity and sample utilizing scattering matrix theory; we then solve the resulting linear system by singular value decomposition to include resonant cavity length determination. Finally, in chapter 6, we discuss cavity effects on the leading and second order slab temperatures including preliminary results on temperature uniformity within the slab.

## CHAPTER 2

### LITERATURE SURVEY OF METHODS TO DETERMINE CAVITY ELECTROMAGNETIC FIELDS

For perspective, we include a brief survey of methods that have been used to determine cavity electromagnetic fields and the advantages and disadvantages of each with respect to providing understanding of the interaction between the fields and the loaded cavity.

#### 2.1 Numerical Approaches

Many numerical investigations have been undertaken to describe this interaction, including the finite difference time domain method(FDTD), ( e.g. [10, 11, 12]), the method of lines(MOL), a variation on FDTD which leads to the solution of Maxwell's equations via a system of ODE's (e.g. [14, 15]), and the finite element method(e.g. [17, 18]), all of which require discretization of the entire applicator volume and its load. Although these methods are essential for field computations involving arbitrarily shaped cavities and loads and in cases where the electromagnetic properties of the load vary, they often suffer with respect to the computational time and computer memory required to implement them.

First, for example, when the FDTD method is used to solve hyperbolic systems such as Maxwell's equations, the spatial step size must be a small fraction of the wavelength and the time step even smaller in order to ensure that the Courant stability condition is satisfied and, hence, that the numerical scheme is convergent[14]. The method of lines technique described by Fu and Metaxas in [14] relaxes this stringent condition somewhat but still requires a small enough spatial step size for sufficient solution accuracy. Regardless of whether FDTD, MOL or FEM is used, in situations where the cavity dimensions are typically much larger than the wavelength,

the convergence and accuracy requirements for each of these methods demand sufficiently fine spatial grids so that large computer memory storage and long computation times are necessary.

Secondly, as detailed by Kriegsmann and Hile in [8], these methods are not efficient for low loss ceramics in high Q cavities. A low loss ceramic absorbs small amounts of electromagnetic energy and therefore requires a high Q cavity to allow the electromagnetic fields to build up sufficiently to heat the ceramic. To solve the time dependent Maxwell equations using the FDTD method, assuming a time harmonic incident wave, the time required for the fields to converge to a time harmonic steady state is greatly increased because transient fields will linger in a high Q cavity for many periods before radiating out of the structure. To solve the time harmonic Maxwell equations using the FE method, it is necessary to construct and numerically invert large matrices, which become ill conditioned at resonant states.

Lastly, these numerical schemes certainly can provide an accurate, detailed description of the field-material interaction within a given cavity, but they are not efficient means for obtaining qualitative understanding of the complicated interaction between the fields, the applicator and its load. This is because there are several geometrical and electrical parameters that describe the system and varying them to understand trends and functional relationships creates an intensive computational burden.

## 2.2 Analytical Approaches

Alternatively, analytical analyses for simple cavity and simple geometries have been offered, most notably the two or three dimensional rectangular cavity with cross sectional dielectric slab. For example, in [19], Fu does an analytical study of the propagation of microwaves through a dielectric filled two dimensional waveguide. Paolini [20] considers a three dimensional rectangular cavity with lossy dielectric

cross sectional slab fed by a single mode waveguide. By approximating the aperture field,  $\mathbf{E}_a$ , as the incident time harmonic TE<sub>10</sub> mode(ray approximation) and then introducing a fictitious surface magnetic current,  $\mathbf{M}_a = \mathbf{n} \times \mathbf{E}_a$  in the aperture, he is able to analytically derive approximations for the mode coupling coefficients, i.e. Fourier coefficients, for the Fourier series representations of the fields in the cavity. Consequently he is able to evaluate the field at any point in the cavity and thereby calculate the power deposition across the dielectric sheet.

Shou-Zheng and Han-kui [21] use a similar approach to Paolini's except that they consider a three dimensional rectangular cavity with a cross sectional stratified dielectric load and derive the Fourier series representations of the fields in the cavity by the moment method, i.e. letting  $|\mathbf{M}_a| = \sum_{n=1}^N v_n M_n$  where the  $M_n$  are chosen basis functions and the  $v_n$  are to be determined. They then approximate the integral expressions for the Fourier coefficients as a solution of a linear system for the  $v_n$ 's. Once the fields are known, they run computational experiments to optimize the power distribution in the stratified load by adjustment of the aperture location.

While these approaches give general insight into the nature of the electromagnetic fields in a simply loaded rectangular cavity, they are lacking in systematic parameter studies of trends and functional relationships with respect to the field-material interaction. Meredith[22] acknowledges the need for a more qualitative understanding of this interaction that will complement existing numerical descriptions. He synthesizes modes in a three dimensional rectangular cavity lightly loaded with cross sectional slab by considering the loaded cavity as three mutually orthogonal overmoded waveguides terminating in short circuit plates. He then uses established waveguide and transmission line theory to analyze parameters that determine desirable performance characteristics of the cavity, e.g. insensitivity to loading and low cross coupling between generator feedports in multi-magnetron applications. In general, compared to numerical methods, these analytical approaches

provide a better understanding of the mechanisms involved in propagating the field within a simply loaded cavity, but they become cumbersome or impossible to apply in more complex geometrical situations where numerical methods are the only alternative.

## 2.3 Recent Developments

In recent years, new methods have been developed to overcome the disadvantages inherent in previous numerical and analytical treatments of the loaded electromagnetic cavity problem.

### 2.3.1 Hybrid Method

In [8], Kriegsmann and Hile developed a hybrid asymptotic-numerical technique to model the electromagnetic-material interaction of a low loss ceramic in a high  $Q$  single mode rectangular microwave applicator. Their method involves decomposing the scattering problem into two independent pieces. In one piece, the interaction between the iris, the incident electromagnetic field and the electromagnetic field reflected by a cylindrical ceramic post and short is described asymptotically using scattering matrix theory, which assumes the post is positioned far enough from the iris that evanescent modes generated by the iris and post are negligible. In the other piece, the interaction between the electromagnetic field and the ceramic post in a single mode applicator with iris effectively removed is determined using the FDTD method in conjunction with an absorbing boundary condition for the outgoing scattered field. Then the solutions to these two pieces are analytically combined using a simple connection formula derived from scattering matrix theory to produce an accurate approximation to the original problem. Simulations were conducted using this hybrid method in two dimensions for a low loss cylindrical post and again for a low loss cross sectional slab in a high  $Q$  applicator and then compared to results

obtained for these same configurations using a straight forward application of the FDTD method. Both methods yielded identical results, but the hybrid method was significantly faster (roughly by a factor of six) in both cases.

### **2.3.2 “Gridless” Method**

As an alternative to the grid intensive techniques for determining the electromagnetic field, Feher et al. developed a “gridless” simulation code for solving the time harmonic Maxwell’s equations in large loaded cavities in terms of covariant optics (MiRa-code, Microwave Raytracer)[23, 24]. This code is particularly well suited to computations in the millimeter wave regime where grid methods are impractical even for small cavities. Advantages of this approach are avoidance of grid related convergence restrictions, reduction of computer memory requirement and reduction of computation time as compared with the FDTD and FEM methods; but, like those methods, the MiRa code is able to handle more complex cavity and sample geometries.

## CHAPTER 3

### INITIAL-BOUNDARY VALUE PROBLEM FORMULATION

As a basis for the more difficult analysis of the heating of a ceramic slab of uniform width completely filling the cross section of a three dimensional multi-mode rectangular cavity [left side of Figure (3.1)] in which TE and TM modes would be excited at the aperture, we first examine the simpler two dimensional situation in which the waveguide and cavity are both of uniform height  $H$  in the  $Y$  direction as depicted on the right of Figure (3.1) and having dimensions in the  $XZ$  plane as shown in Figure (3.2). Assuming a waveguide that supports only a  $TE_{10}$  mode, requiring (1) the waveguide and cavity to be of uniform height and (2) a slab of uniform width to fill the entire cross section, prevent the aperture and slab from exciting modes with variations in the  $Y$  direction.

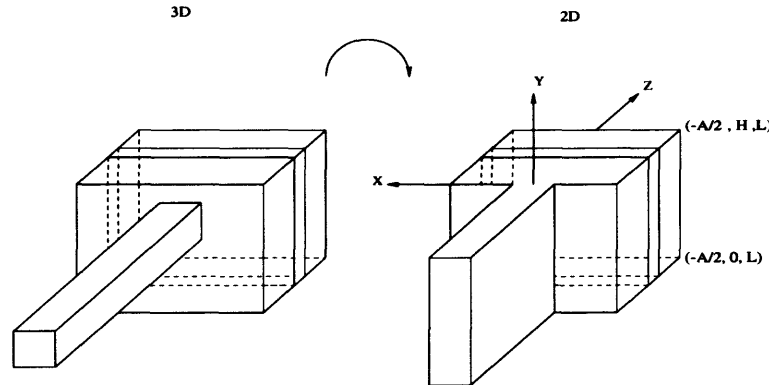


**Figure 3.1** Left: 3-D loaded cavity. Right: 2-D loaded cavity.

The following initial-boundary value problem formulation is identical to that described by Kriegsmann in [7] for a ceramic slab in a two dimensional  $TE_{103}$  applicator with adjustable iris and short. For clarity we summarize the formulation here. However, instead of using an adjustable iris, which retains the single mode nature of the cavity field regardless of the iris size, we fix the waveguide width,  $W$ , and allow the cavity width,  $A$ , and cavity length,  $L$ , to vary. The choice of  $A$  and

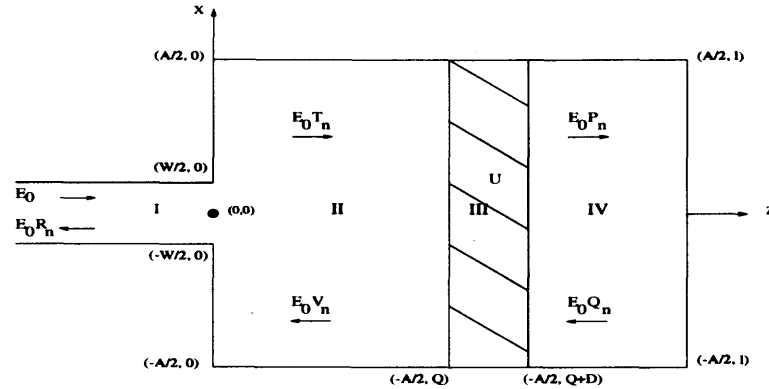


**Figure 3.2** Planar view of 2-D loaded cavity depicting electric field modal amplitudes outside slab and electric field  $U$  inside slab.

$L$  determine a  $TE_{J0n}$  cavity where  $J$  corresponds to cavity width and  $n$  to cavity length. This configuration allows us to examine a variety of multi-mode electric field patterns and their effects on the heating of a ceramic slab.

### 3.1 Electromagnetic Formulation

**Governing Equations.** The free space Maxwell's equations for the time harmonic electromagnetic fields in regions I,II and IV of Figure (3.2) are

$$\nabla \times \tilde{\mathbf{E}} = i\omega\mu_0\tilde{\mathbf{H}} \quad (3.1)$$

$$\nabla \times \tilde{\mathbf{H}} = -i\omega\epsilon_0\tilde{\mathbf{E}} \quad (3.2)$$

$$\nabla \cdot \tilde{\mathbf{E}} = 0 \quad (3.3)$$

$$\nabla \cdot \tilde{\mathbf{H}} = 0, \quad (3.4)$$

where the  $e^{-i\omega t}$  convention is used with  $\omega$  the source frequency (typically 2.45 GHz in industrial microwave heating applications),  $\epsilon_0$  the permittivity of free space and  $\mu_0$  the permeability of free space. With further manipulation, these equations conve-

niently simplify to the Helmholtz equation for both  $\tilde{\mathbf{E}}$  and  $\tilde{\mathbf{H}}$ ,  
i.e.,

$$\nabla^2\{\tilde{\mathbf{E}}, \tilde{\mathbf{H}}\} + K^2\{\tilde{\mathbf{E}}, \tilde{\mathbf{H}}\} = 0 \quad (3.5)$$

where  $K^2 = \omega^2\epsilon_0\mu_0$  is the square of the free space wave number.

The time harmonic Maxwell's equations in region III are the same except that equation (3.2) becomes

$$\nabla \times \tilde{\mathbf{H}} = -i\omega\epsilon_1\tilde{\mathbf{E}} + \sigma(T)\tilde{\mathbf{E}} \quad (3.6)$$

where  $\epsilon_1$  is the electrical permittivity of the ceramic,  $T$  is the temperature and  $\sigma$  is the effective electrical conductivity, incorporating losses primarily due to dipolar or reorientation polarization, which is the most significant loss mechanism in industrial microwave heating applications at frequencies above 1 GHz [9]. Typically,  $\epsilon_1$  depends on temperature also, but here we assume it to be constant since changes in  $\epsilon_1$  with temperature are negligible when compared to changes in  $\sigma$  with temperature[7]. Additionally, both  $\epsilon_1$  and  $\sigma$  are frequency dependent, but we avoid this complication by fixing the source frequency in our problem. Finally, we assume that the ceramic is not susceptible to magnetic losses, with a constant magnetic permeability equal to that of free space. In region III then, from (3.1),(3.3) and (3.6), we find that  $\tilde{\mathbf{E}}$  satisfies

$$\nabla^2\tilde{\mathbf{E}} + (N_1^2 + i\omega\mu_0\sigma)\tilde{\mathbf{E}} = 0 \quad (3.7)$$

where  $N_1^2 = \omega^2\epsilon_1\mu_0$  is the square of the wave number in the ceramic slab.

**Electric Fields.** Suppressing the harmonic time dependence, the electric field in region I of Figure (3.2) is given by

$$\tilde{\mathbf{E}} = E_0 \left\{ e^{iK_1 Z} \tilde{\psi}_1(X) + \sum_{n=1}^{\infty} R_n e^{-iK_n Z} \tilde{\psi}_n(X) \right\} \hat{\mathbf{y}}, \quad Z < 0, \quad (3.8)$$

where we have assumed that the waveguide is excited by a TE<sub>10</sub> mode and supports only that mode.  $K_n = \sqrt{K^2 - n^2\pi^2/W^2}$  are the propagation constants with  $K$  and  $W$  chosen such that  $K_1$  is real and  $K_n = i|K_n|$ ,  $n \geq 2$ ;  $E_0$  is the strength of the incident mode;  $R_n$  are the amplitudes of the reflected modes; and  $\tilde{\psi}_n(X) = \sin[n\pi(X/W + 1/2)]$ .

In region II, the electric field is

$$\tilde{\mathbf{E}} = E_0 \left\{ \sum_{n=1}^{\infty} (T_n e^{i\tilde{\beta}_n Z} + V_n e^{-i\tilde{\beta}_n Z}) \tilde{\phi}_n(X) \right\} \hat{\mathbf{y}}, \quad 0 < Z < Q, \quad (3.9)$$

where  $\tilde{\beta}_n = \sqrt{K^2 - n^2\pi^2/A^2}$  are the propagation constants with  $\tilde{\beta}_1, \dots, \tilde{\beta}_M$  real and  $\tilde{\beta}_n = i|\tilde{\beta}_n|$ ,  $n \geq M + 1$ ;  $T_n$  are the transmission coefficients;  $V_n$  are the reflection coefficients; and  $\tilde{\phi}_n(X) = \sin[n\pi(X/A + 1/2)]$ .

Similarly, in region IV the electric field is

$$\tilde{\mathbf{E}} = E_0 \left\{ \sum_{n=1}^{\infty} (P_n e^{i\tilde{\beta}_n Z} + Q_n e^{-i\tilde{\beta}_n Z}) \tilde{\phi}_n(X) \right\} \hat{\mathbf{y}}, \quad Q + D < Z < L, \quad (3.10)$$

where  $P_n$  and  $Q_n$  are the transmission and reflection coefficients respectively.

Now in region III, if we consider the slab to be thermally insulated on its  $Y = 0, H$  surfaces (see section (3.2)) and given that the exciting electric field is independent of  $Y$ , we may assume that the temperature is also independent of  $Y$ . Then the electric field in region III is given by  $\tilde{\mathbf{E}} = U(X, Z; t_h) \hat{\mathbf{y}}$ , where  $U$  satisfies

$$\left( \frac{\partial^2}{\partial X^2} + \frac{\partial^2}{\partial Z^2} \right) U + N_1^2 \left[ 1 + i \frac{\sigma(T(X, Z; t_h))}{\omega \epsilon_1} \right] U = 0, \quad Q < Z < Q + D. \quad (3.11)$$

Here  $t_h$  is a thermal time, typically on the order of seconds or minutes, which is much greater than a microwave period with a duration on the order of  $10^{-10}$  seconds.

We eventually determine the solution to (3.11) as the leading order electric field in a small convective Biot number asymptotic analysis of the initial boundary value problem consisting of equation (3.11) coupled to a non-homogeneous heat equation in conjunction with appropriate idealized thermal and electromagnetic boundary conditions. To find the electric fields in the cavity and waveguide, we use a scattering matrix formulation to accurately approximate the unknown amplitude coefficients of the propagating modes in regions I,II and IV. To find the leading order electric field in the slab, we solve a two point boundary value problem in  $Z$  that allows us to obtain the first  $M$  terms in a modal representation for this field, where  $M$  is the number of propagating modes in the empty portions of the cavity.

**Magnetic Fields.** Since the magnetic field will not contribute to the heating of the slab, it is sufficient to note that it can easily be found from equation (3.1) and the solution to equation (3.11) in the slab or the appropriate electric field expression in regions I,II or IV. In all regions, the magnetic field has the form

$$\tilde{\mathbf{H}} = \tilde{H}_X(X, Z)\hat{\mathbf{x}} + \tilde{H}_Z(X, Z)\hat{\mathbf{z}}.$$

**Boundary Conditions.** The pertinent electromagnetic boundary and continuity conditions are satisfied as follows:

- (BC 1) On the vertical sides of the waveguide and cavity, the electric fields satisfy boundary conditions which follow from Maxwell's equations and from the assumption that the walls are perfectly conducting, i.e.,  $\tilde{\mathbf{E}} \times \mathbf{n} = \mathbf{0}$  or, equivalently,  $\tilde{\mathbf{E}} \cdot \hat{\mathbf{y}} = 0$ .
- (BC 2) On the walls, bottom ( $Y = 0$ ) and top ( $Y = H$ ) of the waveguide and cavity, the electric fields satisfy  $\partial(\tilde{\mathbf{E}} \cdot \hat{\mathbf{y}})/\partial Y = 0$ , which follows from equation (3.3) and the absence of  $X$  and  $Z$  electric field components.

- (BC 3) The tangential components of the electric and magnetic fields must be continuous across the faces of the slab at  $Z = Q$  and  $Q + D$ , i.e.,

$$[\tilde{\mathbf{E}} \cdot \hat{\mathbf{y}}] = 0 \quad \text{and} \quad \left[ \frac{\partial}{\partial Z} \tilde{\mathbf{E}} \cdot \hat{\mathbf{y}} \right] = 0$$

where  $[ ]$  denotes the jump in the function across the interface.

### 3.2 Thermal Formulation

**Governing Equation and Assumptions.** In the slab the electric field interacts with the ceramic and increases its temperature by dipolar heating according to the equation

$$\rho C_p \frac{\partial}{\partial t_h} T = \kappa \nabla^2 T + \frac{1}{2} \sigma(T) |U|^2 \quad (3.12)$$

where  $U$  satisfies (3.11) and  $t_h$  is the aforementioned thermal time whose scaling is chosen in section (3.3) to obtain a non dimensional slow convective time appropriate for a small Biot number analysis of the coupled thermal-electric system;  $\kappa$  is the thermal conductivity of the ceramic;  $\rho$  is its density;  $C_p$  is the thermal capacity. These thermal parameters typically depend on temperature; here we assume these quantities to be constant since changes in their values with respect to temperature are negligible as compared to changes in the effective electrical conductivity with respect to temperature when a ceramic sample is heated from the ambient temperature to its sintering temperature[25].

Implicit in equation (3.12) is that  $t_h$  is much greater than an electromagnetic wave period. By averaging the heat equation over a wave period, we can effectively remove the wave period time scale, i.e.

$$\frac{1}{2} \sigma(T(t_h)) \frac{\omega}{2\pi} \int_0^{2\pi/\omega} |\tilde{\mathbf{E}}|^2 dt \quad (3.13)$$

with  $\tilde{\mathbf{E}} = \text{Re}[U(X, Z)e^{-i\omega t}]\hat{y}$ ,  $U = U_R + iU_I$  and  $\sigma$  constant with respect to the wave period time scale gives the form of the source term in (3.12)[6].

**Initial/Boundary Conditions and Assumptions.** In keeping with Kriegsmann's treatment in [7], we assume that the slab is initially at the ambient temperature,  $T_A$ , in the cavity, i.e.

$$T(X, Y, Z, 0) = T_A \quad (3.14)$$

and that the temperature satisfies the surface heat balances

$$\kappa \frac{\partial}{\partial Z} T + h_e(T - T_A) + se(T^4 - T_A^4) = 0, \quad Z = Q + D \quad (3.15)$$

$$-\kappa \frac{\partial}{\partial Z} T + h_e(T - T_A) + se(T^4 - T_A^4) = 0, \quad Z = Q \quad (3.16)$$

where  $h_e$  is the effective heat transfer coefficient, which is a measure of how the slab loses heat to its surroundings by convection.  $s$  is the Stefan-Boltzmann constant and  $e$  is the thermal emissivity of the ceramic surface. We assume that the remaining slab surfaces are thermally insulated, i.e.,

$$\frac{\partial}{\partial X} T = 0, \quad X = A/2, -A/2, \quad Q < Z < Q + D \quad (3.17)$$

$$\frac{\partial}{\partial Y} T = 0, \quad Y = 0, H, \quad Q < Z < Q + D. \quad (3.18)$$

These thermal idealizations are introduced for the sake of simplifying the mathematical analysis of the thermal and electromagnetic problems. Specifically, (3.18) is a necessary condition for assuming that the effective electrical conductivity,  $\sigma$ , does not vary in the  $Y$  direction so that a modal representation in  $X$  and  $Z$  for the leading order electric field in the slab can be derived. (See section (5.2)); (3.17) facilitates obtaining a convenient modal representation for the second order

temperature resulting from the small Biot number asymptotic analysis, thereby allowing us to examine the effect of the leading order electric field on spatial variations in temperature within the two dimensional slab.

Finally, we note that, in this model of surface heat transfer, the ability of the ceramic to heat its environment has not been considered. We assume that the empty portions of the cavity and cavity walls remain at the ambient temperature for all time [6]. A more detailed model would have to consider the contribution made by the walls to the heating of the slab in the form of reflected and radiated energy.

### 3.3 Non-dimensionalization

To further facilitate the mathematical analysis, we use the following scalings to non dimensionalize our problem:

$$\mathbf{E} = \frac{\tilde{\mathbf{E}}}{E_0}, \quad (x, y, z) = \frac{(X, Y, Z)}{W}, \quad (d, l, q, a, h) = \frac{(D, L, Q, A, H)}{W},$$

$$u = \frac{U}{E_0}, \quad v = -1 + \frac{T}{T_A}, \quad \tau = \frac{t_h}{t_c}$$

where we have scaled  $t_h$  with respect to the convective time scale  $t_c = \frac{\rho C_p D}{h_e}$ . From our non-dimensionalization, the following parameters naturally arise:

$$B = \frac{h_e D}{\kappa}, \quad p = \frac{\sigma_A D E_0^2}{2 h_e T_A}, \quad \beta = \frac{se T_A^3}{h_e}, \quad \nu = \frac{\sigma_A}{\omega \epsilon_1}, \quad f = \frac{\sigma}{\sigma_A}$$

$$k = KW, \quad n_1 = N_1 W, \quad k_n = K_n W, \quad \beta_n = \tilde{\beta}_n W$$

where  $\sigma_A = \sigma(T_A)$  is the effective electrical conductivity at the ambient temperature;  $B$ , the Biot number, is a measure of the relative effects of convection and conduction and is equivalent to the ratio  $t_d/t_c$ , where  $t_d = \rho C_p D^2/\kappa$  is the diffusive time scale in the ceramic;  $p$ , the non dimensional power, is the ratio of the incident power to the power lost at the  $z$  boundaries of the slab by convection at the ambient temperature;  $\beta$ , the radiative equivalent of the Biot number, is a measure of the relative effects of radiation and convection at the ambient temperature;  $\nu$ , the loss constant, is a measure of the loss in the slab at the ambient temperature and is equivalent to the

square of the ratio of the wavelength in the ceramic to the skin depth at the ambient temperature [6]. Finally  $f$ , the scaled temperature dependent electrical conductivity function, is typically an exponential of the form  $f = e^{cv}$  where  $c$  is a constant appropriate for certain ceramics, such as alumina, over the range of temperatures present in a sintering experiment [7].

In dimensionless form, equations (3.8)-(3.11) of section (3.1) for the electric fields are now

$$\mathbf{E} = \left[ e^{ik_1z} \psi_1(x) + \sum_{n=1}^{\infty} R_n e^{-ik_nz} \psi_n(x) \right] \hat{\mathbf{y}}, \quad z < 0, \quad (3.19)$$

$$\mathbf{E} = \left[ \sum_{n=1}^{\infty} (T_n e^{i\beta_n z} + V_n e^{-i\beta_n z}) \phi_n(x) \right] \hat{\mathbf{y}}, \quad 0 < z < q, \quad (3.20)$$

$$\mathbf{E} = \left[ \sum_{n=1}^{\infty} (P_n e^{i\beta_n z} + Q_n e^{-i\beta_n z}) \phi_n(x) \right] \hat{\mathbf{y}}, \quad q + d < z < l, \quad (3.21)$$

$$\left( \frac{\partial^2}{\partial x^2} + \frac{\partial^2}{\partial z^2} \right) u + n_1^2 [1 + i\nu f(v)] u = 0, \quad q < z < q + d, \quad (3.22)$$

where  $\psi_n(x) = \sqrt{2} \sin n\pi(x + 1/2)$  and  $\phi_n(x) = \sqrt{\frac{2}{a}} \sin n\pi(x/a + 1/2)$  have been normalized and  $k_n = \sqrt{k^2 - n^2\pi^2}$  and  $\beta_n = \sqrt{k^2 - n^2\pi^2/a^2}$  are dimensionless propagation constants with  $k$  restricted to  $(\pi, 2\pi)$  so that only the lowest mode propagates in the waveguide for  $z < 0$ .

Equations (3.12)-(3.18) for the temperature in the slab become

$$B \frac{\partial}{\partial \tau} v = d^2 \nabla^2 v + p B f(v) |u|^2, \quad (3.23)$$

$$v(x, y, z, 0) = 0, \quad (3.24)$$

$$-d \frac{\partial}{\partial z} v + B \{ v + \beta [(v + 1)^4 - 1] \} = 0, \quad z = q \quad (3.25)$$

$$d \frac{\partial}{\partial z} v + B \{v + \beta[(v + 1)^4 - 1]\} = 0, \quad z = q + d \quad (3.26)$$

$$\frac{\partial}{\partial x} v = 0, \quad x = \pm a/2, \quad q < z < q + d \quad (3.27)$$

$$\frac{\partial}{\partial y} v = 0, \quad y = 0, h, \quad q < z < q + d. \quad (3.28)$$

The highly non-linear character of the problem is apparent through (1) the thermal boundary conditions at the slab faces, (2) the source term of the heat equation and particularly through (3) the strong temperature dependence of the electrical conductivity  $f$ . Thus, the electric field propagates through the ceramic and affects the temperature distribution through its presence in (3.23). This, in turn, changes  $f$  in the material, which affects the propagation of the electric field through its presence in (3.22).

In the absence of any simplifications, the only recourse is to solve these coupled equations numerically in an iterative fashion until a steady state temperature is obtained or until thermal runaway occurs [8]. However, this approach is time consuming for the case of a low loss ceramic in a high  $Q$  cavity as discussed in section (2.1), and in the case where the sample is nearly insulated (i.e., the Biot number is small so that the diffusive time scale is much faster than the convective time scale) as discussed in chapter (1). Alternatively, we can introduce simplifications to aid in our analysis of this highly non-linear problem. We exploit a small Biot number and the simplified rectangular geometry of our problem to conduct a more systematic analytical investigation of the effects of the cavity and electric field on the heating of the slab.

## CHAPTER 4

### THERMAL CONSIDERATIONS

This analysis is in accordance with that given in [7]. We seek an asymptotic approximation to  $u$  and  $v$  within the slab in the limit as  $B \rightarrow 0$  with  $\beta$  held fixed. The asymptotic expansions for  $u$  and  $v$  in this limit are

$$u(x, z, \tau; B) = \sum_{n=0}^{\infty} B^n u_n(x, z, \tau)$$

$$v(x, z, \tau; B) = \sum_{n=0}^{\infty} B^n v_n(x, z, \tau).$$

Inserting these expansions into equations (3.22) through (3.28), expanding the non-linear terms in Taylor series and equating to zero the coefficients of the powers of  $B$  yields an infinite set of partial differential equations, which sequentially determine the  $u_n$  and  $v_n$ .

The leading order problem for  $v_0$  is

$$\nabla^2 v_0 = 0 \tag{4.1}$$

$$\frac{\partial}{\partial x} v_0 = 0, \quad x = \pm a/2, \quad q < z < q + d \tag{4.2}$$

$$\frac{\partial}{\partial y} v_0 = 0, \quad y = 0, h, \quad q < z < q + d \tag{4.3}$$

$$\frac{\partial}{\partial z} v_0 = 0, \quad z = q, q + d \tag{4.4}$$

$$v_0(x, z, 0) = 0, \tag{4.5}$$

which has a solution that is independent of  $x$  and  $z$ , i.e.  $v_0(\tau)$ . This makes intuitive sense since we expect a completely insulated slab subject to a volumetric heat source to become spatially uniform on the slow time scale  $\tau$ .

The leading order equation for  $u_0$  is

$$\left( \frac{\partial^2}{\partial x^2} + \frac{\partial^2}{\partial z^2} \right) u_0 + n_1^2 [1 + i\nu f(v_0)] u_0 = 0, \quad q < z < q + d, \quad (4.6)$$

subject to the boundary condition  $u_0 = 0$  at  $x = \pm a/2$  and the continuity of  $u_0$  and  $\frac{\partial}{\partial z} u_0$  at  $z = q$  and  $z = q + d$  with the tangential components of the cavity electric and magnetic fields respectively. We find  $u_0$  in the next chapter by separation of variables, which is appropriate since  $u_0$  depends only parametrically on  $\tau$  through  $v_0$ . The equation that determines  $v_0$  is found from the solvability condition that guarantees the existence of the second order temperature  $v_1$ . It is

$$\frac{d}{d\tau} v_0 = 2L(v_0) + pf(v_0) \|u_0(v_0)\|^2 \quad (4.7)$$

$$\|u_0\|^2 = \frac{1}{ad} \int_{-a/2}^{a/2} \int_q^{q+d} |u_0|^2 dz dx \quad (4.8)$$

where  $L(v_0) = -v_0 - \beta((v_0 + 1)^4 - 1)$ . This non-linear ordinary differential equation and the corresponding initial condition (4.5) constitute an initial value problem whose steady state solutions are discussed in section (6.1).

Finally, the problem for  $v_1$  is

$$\nabla^2 v_1(x, z; \tau) = \frac{1}{d^2} \left[ \frac{d}{d\tau} v_0 - pf(v_0) |u_0(x, z; v_0)|^2 \right], \quad (x, y, z) \in \mathbf{S} \quad (4.9)$$

$$\frac{\partial}{\partial z} v_1 = \frac{-L(v_0)}{d}, \quad z = q, \quad -a/2 < x < a/2, \quad 0 < y < h \quad (4.10)$$

$$\frac{\partial}{\partial z} v_1 = \frac{L(v_0)}{d}, \quad z = q + d, \quad -a/2 < x < a/2, \quad 0 < y < h \quad (4.11)$$

$$\frac{\partial}{\partial x} v_1 = 0, \quad x = \pm a/2, \quad q < z < q + d, \quad 0 < y < h \quad (4.12)$$

$$\frac{\partial}{\partial y} v_1 = 0, \quad y = 0, h, \quad q < z < q + d, \quad -a/2 < x < a/2 \quad (4.13)$$

$$v_1(x, z; 0) = 0 \quad (4.14)$$

where  $\mathbf{S}$  denotes the interior of the three dimensional slab. We now have non-linear heat flux through the slab faces at  $z = q$  and  $z = q + d$ . The form of the

source term and the boundary conditions indicate that  $v_1$  has no  $y$  dependence. It is the spatial dependence in  $x$  and  $z$  that gives rise to non uniformities in this temperature field. We expect  $v_1$  to be bounded in  $x$  and  $z$  so that an asymptotically valid second order approximation for  $v$  can be obtained, i.e.,  $v \sim v_0 + Bv_1$  with  $Bv_1 \ll v_0$ . The solution for  $v_1$  is derived in appendix C. We note here that this bounded solution includes an additive term (denoted  $c_2$  in the appendix) that only depends on  $\tau$ . A complicated exponentially decaying solution for  $c_2$  can be determined from the solvability condition that guarantees the existence of  $v_2$ , but since we are primarily interested in the spatial variations to  $O(B)$ , this additive term is unimportant. Further analysis and interpretation of  $v_1$  for various cavity widths is conducted in section (6.2). Before proceeding further, we find the electric fields in the waveguide and cavity and the solution to equation (4.6) in the slab. This is required to determine  $v_0$  and  $v_1$ .

## CHAPTER 5

### ELECTROMAGNETIC CONSIDERATIONS

#### 5.1 Empty Two Dimensional Cavity

Before finding the time harmonic electric fields in the slab loaded two dimensional cavity, we first use scattering matrix theory to determine the propagating time harmonic electric field within the two dimensional lossless cavity and waveguide without the slab. This method forms the basis of the method used to find the propagating fields in the loaded cavity case with the restriction that the slab be positioned far enough from the aperture that evanescent modes generated by the aperture can be neglected. In addition, we seek cavity lengths that maximize the electric field in the slab. These resonant fields are instrumental in minimizing power levels required for sintering.

##### 5.1.1 Boundary Value Problem For Electric Field

We want to know the electric field,  $u_e$ , in the waveguide and cavity neglecting evanescent modes due to the aperture. We must solve the scalar Helmholtz equation

$$\nabla^2 u_e + k^2 u_e = 0 \quad (5.1)$$

in the region  $(-\infty < z \ll 0, -1/2 < x < 1/2) \cup (0 \ll z < l, -a/2 < x < a/2)$  subject to boundary conditions (BC 1) and (BC 2) of section (3.1) and where  $u_e$  takes the asymptotic forms

$$u_e \approx [e^{ik_1 z} + \tilde{R}_1 e^{-ik_1 z}] \psi_1(x), \quad z \ll 0 \quad (5.2)$$

with  $z \ll 0$  defined to be all  $z$  such that  $e^{|k_n|z} \ll 1$  for  $n \geq 2$ , and

$$u_e \approx \sum_{n=1}^M [B_n e^{i\beta_n z} + A_n e^{-i\beta_n z}] \phi_n(x), \quad 0 \ll z < l \quad (5.3)$$

with  $0 \ll z$  defined to be all  $z$  such that  $e^{-|\beta_n|z} \ll 1$  for  $n \geq M+1$ . This asymptotic condition may be determined by applying (BC 1) of (3.1) at  $z = l$  to the full infinite series representation for  $u$  in  $0 < z < l$  to obtain  $A_n = -e^{2i\beta_n l} B_n$  and then using the fact that  $\beta_n = i|\beta_n|$  for  $n \geq M+1$ . The value of the positive integer  $M$  is determined by the choice of  $k$  in the interval  $(\pi, 2\pi)$  and the width of the cavity,  $a$ ; that is, if  $\beta_M^2 \geq 0 > \beta_{M+1}^2$ , then for all  $a$  such that  $M\pi/k \leq a < (M+1)\pi/k$  there are  $M$  propagating cavity modes. In the case when  $\beta_M = 0$ , the  $M^{\text{th}}$  mode makes a non-evanescent contribution to the total field and must be included as a propagating mode. Although the propagating modal amplitudes  $\tilde{R}_1, A_n, B_n, n = 1 \dots M$ , can not be found exactly, a method for accurately approximating them, similar to the method considered in [8] and [7] for a single mode cavity with iris, is described below.

### 5.1.2 Scattering Matrix Formulation

In Figure (5.1) we assume that the imaginary plane  $z = z_I$  is located far enough from the aperture so that the electric field there is given by (5.3). Consider first the region  $z < z_I$  containing the aperture, which is irradiated by  $M+1$  propagating modes with amplitudes  $A_0, \dots, A_M$ . The mode from the left has amplitude  $A_0 = 1$  and is due to the source, i.e., the first term in (5.2). The other  $M$  modes with amplitudes  $\mathbf{A} = (A_1, \dots, A_M)$  are reflected from the short at  $z = l$ , i.e., the second set of terms in (5.3). The aperture appears to reflect a mode of amplitude  $R_1$  to the left, i.e., the second term in (5.2), and  $M$  modes with amplitudes  $\mathbf{B} = (B_1, \dots, B_M)$  to the right, i.e., the first set of terms in (5.3).

These amplitudes are related by the  $M+1$  linear equations

$$\tilde{R}_1 = r_1 A_0 + \sum_{n=1}^M \tau_{1n} A_n \quad (5.4)$$

$$B_j = t_j A_0 + \sum_{n=1}^M \gamma_{jn} A_n, \quad j = 1, \dots, M, \quad (5.5)$$

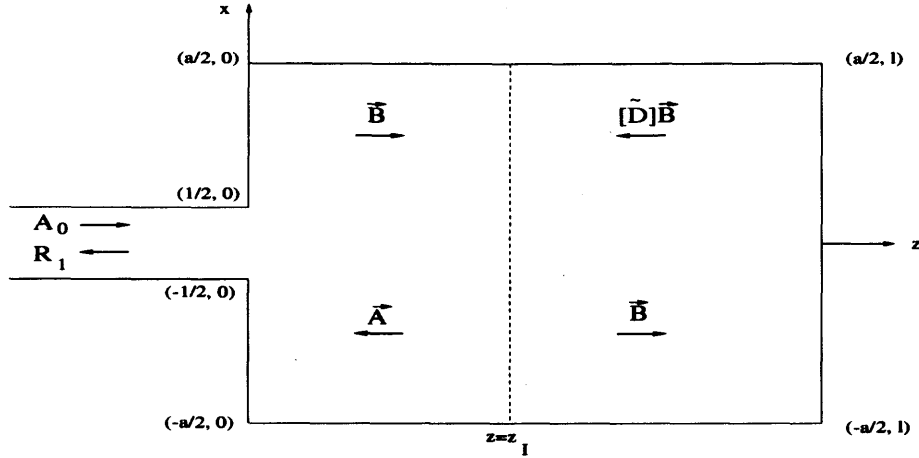


**Figure 5.1** Empty 2-D cavity depicting propagating modal amplitudes.

where the matrix determined by this linear system is called the scattering matrix for the aperture.  $r_1$  is the reflected propagating mode coefficient and  $\mathbf{t} = (t_1, \dots, t_M)$  are the transmitted propagating mode coefficients due to a mode of strength 1 and propagation constant  $k_1$  incident from the left upon the aperture located at  $z = 0$  in an infinite perfectly conducting waveguide of width 1 for  $z < 0$  and width  $a$  for  $z > 0$ . The  $\tau_{1n}$  and  $\gamma_{jn}$  are the propagating transmission and reflection coefficients respectively due to the  $j^{\text{th}}$  mode of strength 1 and propagation constant  $\beta_j$  incident upon the aperture from the right in the same infinite waveguide. These coefficients for the left and right problems in the infinite guide depend on the values of the tangential electric and magnetic fields in the aperture, which unfortunately, can not be found in closed form; however, in appendix A, we derive accurate approximations to the first  $N$  coefficients by using Galerkin's method to solve an integral equation for the aperture field in both the left and right problems. In doing so, it is necessary that  $N \geq M$  where  $N$  is the number of terms used in the Galerkin approximation for the aperture field.

Next, consider the region  $z > z_I$  in Figure (5.1). Each of the terms in the first set of terms of (5.3) can be interpreted as a mode of strength  $B_n$  incident upon the short at  $z = l$ . The second set of terms in (5.3) are the modes reflected by the short. Substituting  $A_n = -e^{2i\beta_n l} B_n$  into equations (5.5), we obtain the linear system

$$[I + \Gamma(a, k) \tilde{D}(a, k, l)]\mathbf{B} = \mathbf{t}(a, k), \quad (5.6)$$

where

$$\tilde{D} = \begin{bmatrix} e^{2i\beta_1(a,k)l} & 0 & \cdots & 0 \\ 0 & \ddots & \ddots & \vdots \\ \vdots & \ddots & \ddots & 0 \\ 0 & \cdots & 0 & e^{2i\beta_M(a,k)l} \end{bmatrix}, \quad \Gamma = \begin{bmatrix} \gamma_{11}(a, k) & \cdots & \gamma_{1M}(a, k) \\ \vdots & & \vdots \\ \vdots & & \vdots \\ \gamma_{M1}(a, k) & \cdots & \gamma_{MM}(a, k) \end{bmatrix}$$

and  $I$  is the identity matrix. The structure of  $\Gamma$  and  $\mathbf{t}$  and the dependence of their elements on cavity width  $a$  and wavenumber  $k$  is explicitly shown in appendix A. In particular, we show that mode symmetry with respect to the axis of the waveguide and cavity requires that the even numbered elements of  $\mathbf{t}$  are zero and the odd(even) numbered elements of the  $j^{\text{th}}$  column of  $\Gamma$  are zero for  $j$  even(odd).

Thus, upon solving system (5.6), we have determined the approximate amplitudes for the left and right propagating modes in the cavity. Substitution of the  $A_n$ 's into equation (5.4) gives  $\tilde{R}_1$ , the amplitude of the reflected propagating mode in the waveguide, where  $|\tilde{R}_1|^2 = 1$  for  $z \ll 0$  by conservation of power for a lossless waveguide and cavity. The electric fields for  $z \ll 0$  and  $z \gg 0$  are then given by expressions (5.2) and (5.3) respectively, with the even numbered  $A_n$  and  $B_n$  suppressed in keeping with the mode symmetry. It must be emphasized that the solution to (5.6) is an approximation whose accuracy ultimately depends on the number of Galerkin basis functions used in the representation of the aperture field considered in appendix A.

### 5.1.3 Solution of Linear System for Propagating Mode Amplitudes and Resonant Length Determination

We now consider solutions to equation (5.6) for various cavity widths. In particular we consider cavity widths for the cases  $M = 1$ ,  $M = 2$  and  $M = 3$  and seek resonant cavity lengths in the case of one dominant mode; that is, resonant lengths corresponding to only one out of  $M$  propagating mode amplitudes being much larger than the other  $M - 1$  amplitudes. In subsequent calculations we fix  $k = 3\pi/2$ .

Before proceeding further, we must note the pathological case of  $\beta_M = 0$ , which causes the matrix  $I + \Gamma\tilde{D}$  to be singular for any cavity length. This is a non-physical artifice that results from the neglect of evanescent modes and may be remedied by including one or more evanescent modes in the determination of (5.6). We avoid this case in subsequent computations.

**5.1.3.1  $M = 1$ .** We first consider  $a = 1$ . This is the simplest case in which we merely have a truncated semi-infinite waveguide. The solution to (5.6) is  $B_1 = 1$  since  $\gamma_{11} = 0$  and  $t_1 = 1$ . For  $1 < a < 2\pi/k$ , the cavity width is slightly larger than the waveguide width. Now  $0 << |t_1| < 1$  and  $0 < |\gamma_{11}| \ll 1$  as per equations (A.14) and (A.22) of appendix (A), so that (5.6) gives

$$B_1 = \frac{t_1}{1 + \gamma_{11}e^{2i\beta_1 l}}. \quad (5.7)$$

We do not expect  $|B_1|$  to be arbitrarily large and, accordingly, the denominator of (5.7) can never equal zero since  $0 < |\gamma_{11}| \ll 1$ . However, it is possible to determine resonant lengths,  $l_r$ , which maximize  $|B_1|$  or, equivalently, minimize the denominator of  $|B_1|$ . Using the fact that the tangent function is  $\pi$ -periodic, we find two possibilities for a resonant length,

$$l_r^{max} = \frac{(n - 1/2)\pi}{\beta_1} - \frac{1}{2\beta_1} \tan^{-1} \left( \frac{\text{Im } \gamma_{11}}{\text{Re } \gamma_{11}} \right) \quad (5.8)$$

$$l_r^{min} = \frac{n\pi}{\beta_1} - \frac{1}{2\beta_1} \tan^{-1} \left( \frac{\text{Im } \gamma_{11}}{\text{Re } \gamma_{11}} \right), \quad n = 1, 2, 3, \dots \quad (5.9)$$

where  $l_r^{max}$  maximizes  $|B_1|$ , namely,

$$|B_1|^{max} = \frac{|t_1|}{(1 - |\gamma_{11}|)^2}, \quad (5.10)$$

$l_r^{min}$  minimizes  $|B_1|$ , namely,

$$|B_1|^{min} = \frac{|t_1|}{(1 + |\gamma_{11}|)^2} \quad (5.11)$$

and  $n\pi/\beta_1$  is the eigenlength for a closed cavity with width  $a$  and length determined by  $n$ . Thus, the choice of  $n$  in (5.8) and (5.9) determines the desired open resonant cavity lengths. For example, taking  $a = 1.2$  and setting  $n = 3$  determines a  $\text{TE}_{103}$  cavity with  $l_r^{max} = 2.0863$ ,  $|B_1|^{max} = .9990$  or  $l_r^{min} = 2.4872$ ,  $|B_1|^{min} = .8973$  and standing wave patterns as shown in Figures (5.2) and (5.3). It is important to note that the depiction of the electric field near the aperture is not realistic since evanescent modes have not been included in the field calculations. If an adequate number of these evanescent modes were included, the strength of the field near the aperture would be decreased accordingly. Nevertheless, we have illustrated how the choice of cavity length and width determines the desired field pattern.

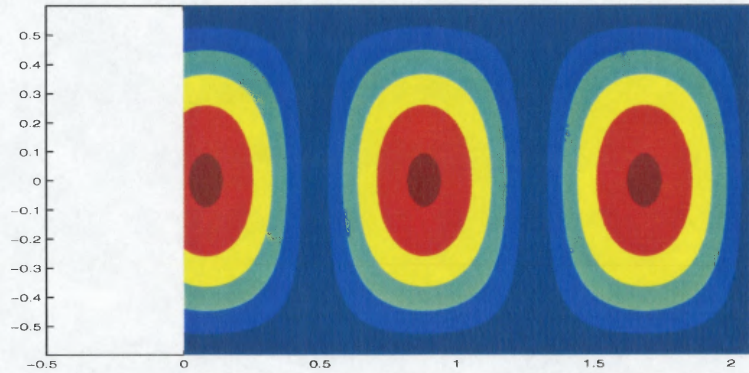


**Figure 5.2** Electric field pattern in  $\text{TE}_{103}$  cavity with  $l = l_r^{max} = 2.0863$ .

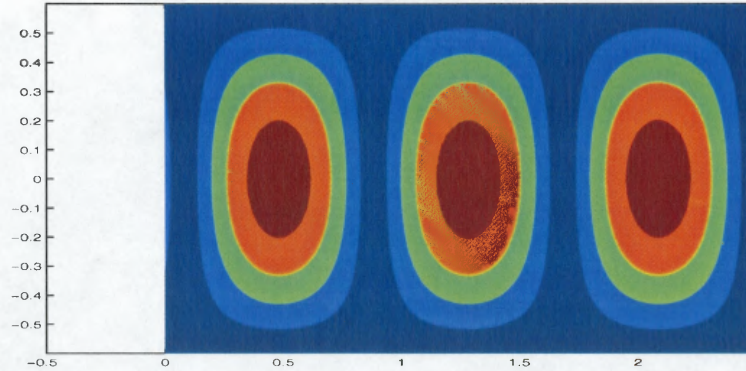


**Figure 5.3** Electric field pattern in  $TE_{103}$  cavity with  $l = l_r^{min} = 2.4872$ .

**5.1.3.2**  $M = 2$ . For this case, equation (5.6) has

$$\Gamma = \begin{bmatrix} \gamma_{11} & 0 \\ 0 & \gamma_{22} \end{bmatrix} \quad \text{and} \quad \mathbf{t} = \begin{pmatrix} t_1 \\ 0 \end{pmatrix}.$$

It follows that  $B_2 = 0$  and  $B_1$  is the same as expression (5.7), except that the numerical values of  $\gamma_{11}$  and  $t_1$  are different. Consequently, we obtain the same formulas for  $l_r^{max}$ ,  $l_r^{min}$  and the same field patterns as in the  $M = 1$  case.

**5.1.3.3**  $M \geq 3$ . For these values of  $M$ , we encounter two complications that were not present for  $M = 1$  and  $M = 2$ . First, the amplitude of the dominant mode may become very large at resonant cavity lengths. In this case, the matrix  $I + \Gamma \tilde{D}$  is near singular implying that the solution to the linear system is inherently sensitive to small perturbations in the cavity length. Therefore, we use a singular value decomposition of  $I + \Gamma \tilde{D}$  to maintain vector length scales and achieve the best possible numerically stable solution to (5.6) at resonant lengths[26]. Secondly, it is not possible to derive an explicit expression for the resonant lengths; instead, they are implicit solutions to a transcendental equation whose form depends on which mode we wish to excite in the cavity and whose complexity increases as the value of  $M$  increases. In principle, we may solve any of the resulting transcendental equations numerically to obtain

resonant lengths for a given cavity width. In practice, we avoid this computational burden by conducting a graphical search for our desired resonant lengths.

To illustrate, we take  $M = 3$  and choose as a reference length,  $l_{cc}$ , the Helmholtz eigen-length for a closed square cavity; that is,  $l_{cc} = a = \frac{\pi}{k}\sqrt{n^2 + J^2}$  where  $n$  and  $J$  are positive integers,  $n$  corresponding to the  $z$  direction and  $J$  corresponding to the  $x$  direction. For  $M = 3$ , we have  $\frac{3\pi}{k} < a < \frac{4\pi}{k}$ , which implies that either  $n^2 + J^2 = 10$  or  $n^2 + J^2 = 13$ . Both of these possibilities are double degeneracies for squares of side length  $l_{cc} = 2.1082$  and  $l_{cc} = 2.4037$  respectively. We choose the case of  $n^2 + J^2 = 10$ , which will determine electric field patterns in the open cavity corresponding to  $n = 3, J = 1$  and  $n = 1, J = 3$  for specific resonant lengths. These are  $TE_{103}$  and  $TE_{301}$  cavities respectively. In the case of  $n^2 + J^2 = 13$ , a field pattern corresponding to  $n = 2, J = 3$  is supported in the open cavity, but one corresponding to  $n = 3, J = 2$  is not since even numbered modes are suppressed in the  $x$  direction.

To determine the two resonant lengths in the case of  $n^2 + J^2 = 10$ , we plot  $|B_1|$  and  $|B_3|$  as functions of  $l$  where  $B_1$  and  $B_3$  are the non zero components of  $\mathbf{B}$ . In Figure (5.4) it is evident that at  $l_r^{max} = 2.0982$ ,  $|B_3|$  is maximized and dominates  $|B_1|$ , while in figure (5.6) at  $l_r^{min} = 2.0944$ ,  $|B_3|$  is minimized and is subdominant to  $|B_1|$ . Plots of the magnitude of the electric field in the cavity corresponding to these two cases are shown in Figures (5.5) and (5.7). While both modal patterns are supported in the closed square Helmholtz cavity of side length  $l_{cc} = 2.1082$ , this example shows that the presence of an opening in the cavity causes this resonant length to shift and split into two slightly different resonant lengths, each of which supports only the modal pattern and amplitude indicated. The reason for the vast disparity in field amplitude between the two cases is due to a three order of magnitude difference in the smallest singular values of the matrix  $I + \Gamma\tilde{D}$  at  $l_r^{max}$  and  $l_r^{min}$  respectively.

We have demonstrated that determining a specific field pattern and amplitude can be quite sensitive to the choice of resonant length. For wider and longer cavities, discriminating between resonant lengths can become even more problematic due to the greater number of possible resonant field configurations and the higher density of corresponding resonant lengths within a given range of cavity lengths.

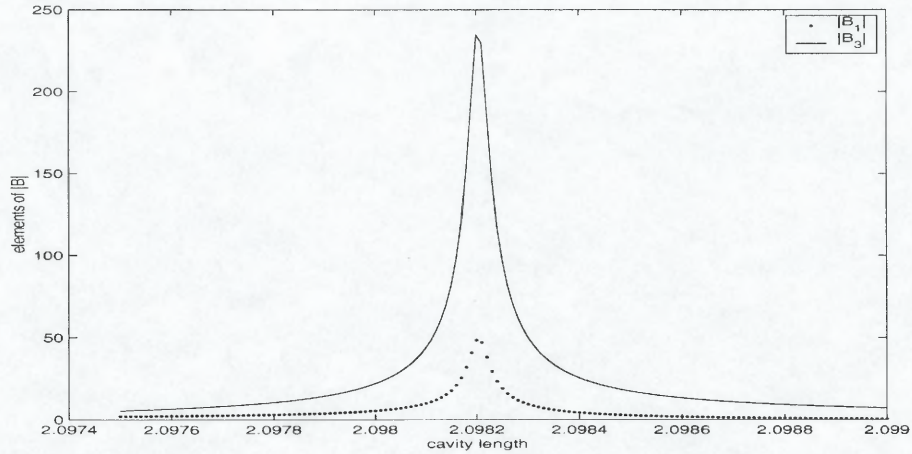


**Figure 5.4**  $M = 3$ : Mode amplitudes vs. cavity length near resonant maximum length,  $l_r^{max} = 2.0982$ .

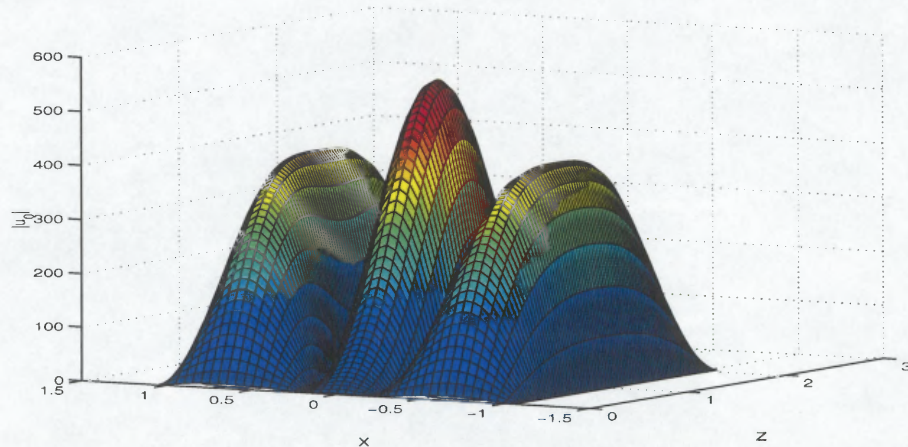


**Figure 5.5** Dominant  $TE_{301}$  mode for  $l_r^{max} = 2.0982$ .

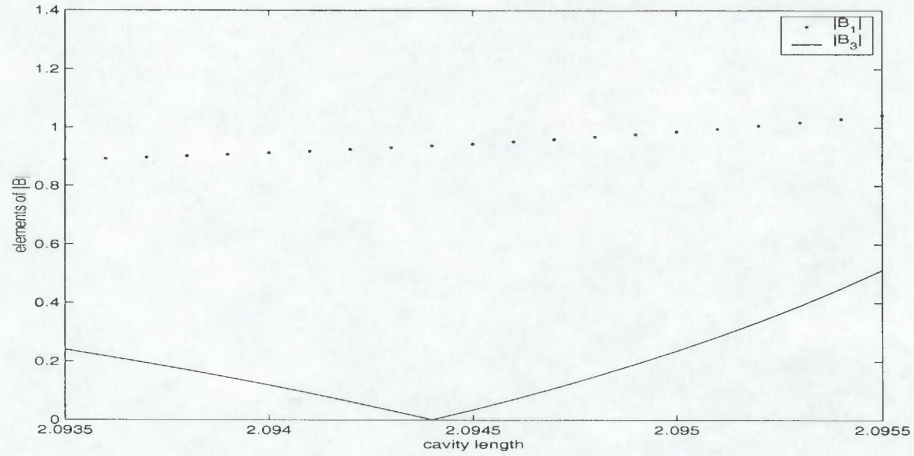


**Figure 5.6**  $M = 3$ : Mode amplitudes vs. cavity length near resonant minimum length,  $l_r^{min} = 2.0944$ .

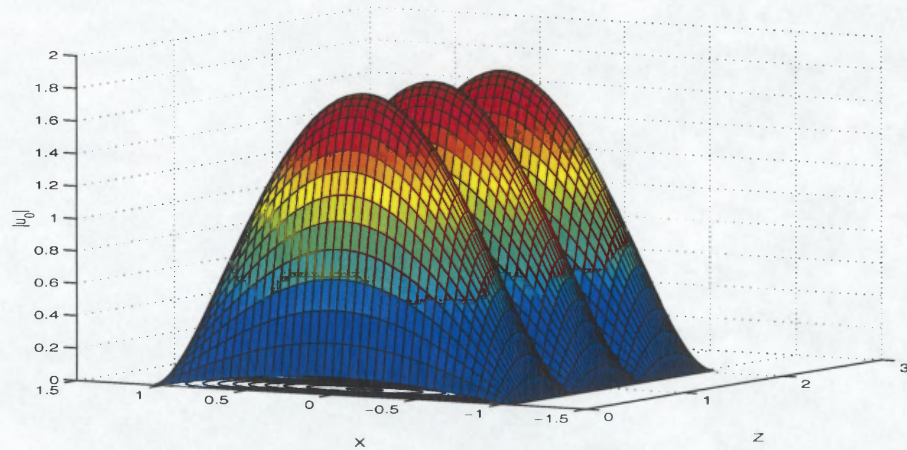


**Figure 5.7** Dominant  $TE_{103}$  mode for  $l_r^{min} = 2.0944$ .

## 5.2 Slab Loaded Two Dimensional Cavity

We consider again our original ceramic slab loaded two dimensional cavity and proceed to find the propagating electric field,  $u_c$ , in the waveguide and empty portions of the cavity by combining the scattering matrix for the aperture used in section (5.1.2) with the scattering matrix for the slab to be determined shortly. The simple

rectangular geometry of the slab and cavity allows the elements of this scattering matrix to be found analytically. We then find the first  $M$  terms in the modal representation for the leading order electric field in the slab, assuming that the slab is far enough from the aperture to neglect evanescent modes. Resonant lengths in the case of a cavity containing a lossless slab are found using same the same analytical and graphical methods as were used in the empty cavity case.

### 5.2.1 Boundary Value Problem For Electric Field

In region I of Figure (5.8) the  $y$  component of the electric field satisfies

$$u_c(x, z) \approx e^{ik_1 z} \psi_1(x) + R_1 e^{-ik_1 z} \psi_1(x), \quad z \ll 0 \quad (5.12)$$

where  $R_1$  is unknown. In region II

$$u_c(x, z) \approx \sum_{n=1}^M (T_n e^{i\beta_n z} + V_n e^{-i\beta_n z}) \phi_n(x), \quad 0 \ll z < q \quad (5.13)$$

and in region IV

$$u_c(x, z) \approx \sum_{n=1}^M (P_n e^{i\beta_n z} + Q_n e^{-i\beta_n z}) \phi_n(x), \quad q + d < z < l \quad (5.14)$$

where  $V_n = \rho_n T_n$ ,  $P_n = \alpha_n T_n$  and  $Q_n = \mu_n \alpha_n T_n$  are unknown.  $z \ll 0$  and  $z \gg 0$  are defined to be all  $z$  such that evanescent modes generated by the aperture can be neglected. The condition that ensures the slab is located far enough from the aperture so that evanescent modes can be neglected is deduced from the solution for the leading order electric field in the slab at  $z = q$  [See section (5.2.4)]. It is  $e^{-2|\beta_n|q} \ll 1$  for  $n \geq M + 1$ . Note that the solutions in regions I, II and IV automatically satisfy boundary conditions (BC 1) and (BC 2) of section (3.1).

If we assume that the effective electrical conductivity of the ceramic does not vary in the  $y$  direction, then the  $y$  component of the leading order electric field in the slab satisfies

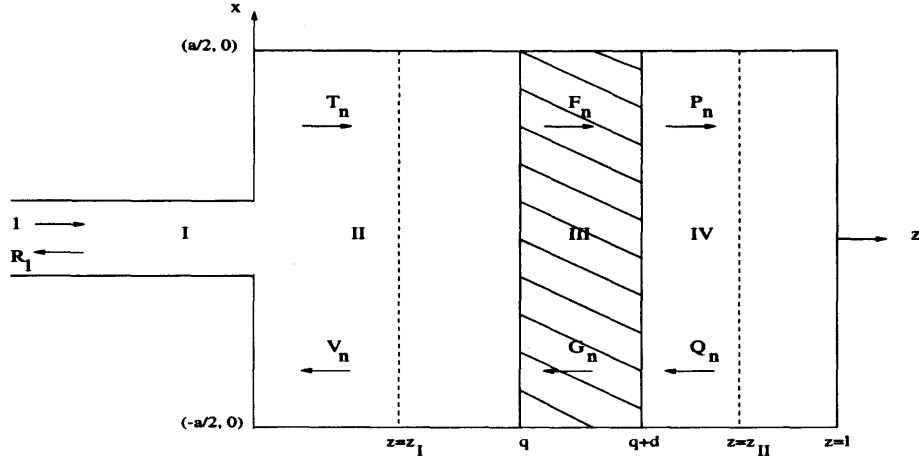


**Figure 5.8** Two dimensional configuration depicting propagating modal amplitudes in the cavity and modal amplitudes in the slab.

$$\nabla^2 u_0(x, z; \tau) + n_1^2 [1 + i\nu f(v_0(\tau))] u_0(x, z; \tau) = 0, \quad (5.15)$$

subject to the continuity of the tangential electric and magnetic fields at the slab faces. The solution has the modal representation

$$u_0(x, z; \tau) = \sum_{n=1}^{\infty} \left( F_n e^{i[\theta_n(\tau)](z-q)} + G_n e^{-i[\theta_n(\tau)](z-q)} \right) \phi_n(x); \quad (5.16)$$

where  $\theta_n = \sqrt{\chi_n^2 + in_1^2 \nu f(v_0(\tau))}$  with  $\chi_n^2 = n_1^2 - (n\pi/a)^2$  are the dimensionless propagation constants in the slab. The imaginary part of  $\theta_n$  is called the loss factor and governs the rate of exponential decay of each slab mode. Since  $0 < \arg(\theta_n) < \pi/2$  for all  $n$ , we choose the positive branch of  $\theta_n$  in subsequent calculations. As with the solutions in regions I, II and IV,  $u_0$  automatically satisfies (BC 1) and (BC 2) of section (3.1) on the portions of the cavity adjacent to the slab. The first  $M$   $F_n$  and  $G_n$  will be found in terms of the  $T_n$  as a result of assuming the appropriate ansatz for  $u_0$  and then solving a linear two point boundary value problem in  $z$  within the

slab. We defer solution of this boundary value problem until after the  $T_n$  have been determined in the next section.

### 5.2.2 Scattering Matrix Formulation for Cavity Electric Field

We want to find the propagating electric field in the empty regions of Figure (5.8). We will combine scattering matrices for the aperture and slab to obtain an  $M \times M$  linear system whose form is similar to that obtained in the empty cavity case and whose solution gives the propagating  $T_n$ ,  $n = 1, \dots, M$ . Consider  $z = z_I$  in Figure (5.8) where the propagating electric field is given by (5.13). For  $z < z_I$  we have already found the scattering matrix for the aperture in terms of the reflection and transmission coefficients for the infinite stepped guide. [See section (5.1.2) and appendix A]. In terms of these coefficients and those shown in regions I and II of Figure (5.8), we have the  $M + 1$  linear equations

$$R_1 = r_1 + \sum_{n=1}^M \tau_{1n} V_n \quad (5.17)$$

$$T_j = t_j + \sum_{n=1}^M \gamma_{jn} V_n, \quad j = 1, \dots, M, \quad (5.18)$$

Consider  $z = z_{II}$  in Figure (5.8) where the propagating electric field is given by (5.14). For  $z > z_{II}$ , we apply the Dirichlet condition at  $z = l$  to get  $\mu_n = -e^{2i\beta_n l}$ .

Proceeding in the same manner as for the aperture of section (5.1.2), we now consider the region  $z_I < z < z_{II}$  containing the slab, which is irradiated by  $2M$  propagating modes with amplitudes  $T_1, \dots, T_M$  from the left and  $Q_1, \dots, Q_M$  from the right. The  $T_n$  are generated by the aperture; the  $Q_n$  are reflected from the short at  $z = l$ . The slab appears to reflect  $M$  modes with amplitudes  $V_1, \dots, V_M$  to the left and  $M$  modes with amplitudes  $P_1, \dots, P_M$  to the right. These amplitudes are related by the  $2M$  linear equations

$$V_j = \sum_{n=1}^M \hat{a}_{jn} T_n + \hat{d}_{jn} Q_n, \quad j = 1, \dots, M \quad (5.19)$$

$$P_j = \sum_{n=1}^M \hat{b}_{jn} T_n + \hat{c}_{jn} Q_n, \quad j = 1, \dots, M, \quad (5.20)$$

with

$$\hat{a}_{jn} = e^{i(\beta_j + \beta_n)q} \frac{2i(\theta_n^2 - \beta_n^2) \sin(\theta_n d) \delta_{jn}}{\Delta_n} \quad (5.21)$$

$$\hat{b}_{jn} = e^{i[\beta_j q - \beta_n(q+d)]} \frac{4\beta_n \theta_n \delta_{jn}}{\Delta_n} \quad (5.22)$$

$$\hat{c}_{jn} = e^{-i(\beta_j + \beta_n)(q+d)} \frac{2i(\theta_n^2 - \beta_n^2) \sin(\theta_n d) \delta_{jn}}{\Delta_n} \quad (5.23)$$

$$\hat{d}_{jn} = \hat{b}_{jn} \quad (5.24)$$

$$\Delta_n = (\beta_n + \theta_n)^2 e^{-i\theta_n d} - (\beta_n - \theta_n)^2 e^{+i\theta_n d}. \quad (5.25)$$

where  $\delta_{jn}$  is the Kronecker symbol. The matrix determined by this linear system is the scattering matrix for the slab. The  $\hat{a}_{jn}$  are the reflected propagating mode coefficients for  $z < q$  and  $\hat{b}_{jn}$  are the transmitted propagating mode coefficients for  $z > q+d$  due to the  $j^{\text{th}}$  mode of strength 1 and propagation constant  $\beta_j$  incident from the left upon the slab located in an infinite perfectly conducting waveguide of width  $a$ . Similarly, the  $\hat{c}_{jn}$  and  $\hat{d}_{jn}$  are the propagating reflection and transmission coefficients respectively due to the  $j^{\text{th}}$  mode of strength 1 and propagation constant  $\beta_j$  incident upon the slab from the right in the same infinite waveguide. In appendix (B) we derive (5.21)-(5.25) using the continuity of the tangential electric and magnetic fields at the  $z = q$  and  $z = q + d$  slab faces.

We must find  $R_1$  in (5.17) and  $T_j$   $j = 1, \dots, M$  in (5.18). Substituting  $Q_n = \mu_n P_n$  into equations (5.20) and (5.19) gives

$$\mathbf{P} = \left[ (I - \hat{C}\mu)^{-1} \hat{B} \right] \mathbf{T} \quad (5.26)$$

$$\mathbf{V} = \left[ \hat{A} + \hat{D}\mu (I - \hat{C}\mu)^{-1} \hat{B} \right] \mathbf{T}, \quad (5.27)$$

where  $\hat{A} = \text{diag}(\hat{a}_{jj})$ ,  $\hat{B} = \text{diag}(\hat{b}_{jj})$ ,  $\hat{C} = \text{diag}(\hat{c}_{jj})$ ,  $\hat{D} = \text{diag}(\hat{d}_{jj})$ , and  $\mu = \text{diag}(\mu_j)$   $j = 1, \dots, M$  with “diag” indicating a diagonal matrix. We note that the  $M \times M$  matrices multiplying  $\mathbf{T}$  in equations (5.26) and (5.27) are also diagonal so that we now know  $\alpha_j$ , the transmission coefficients in region IV and  $\rho_j$ , the reflection coefficients in region II. Using (5.27) in (5.17) gives the scalar equation

$$R_1 = r_1 + \boldsymbol{\tau}_1 \cdot \mathbf{V} \quad (5.28)$$

where  $\boldsymbol{\tau}_1 = (\tau_{11}, \dots, \tau_{1M})$ ,  $\mathbf{V} = (V_1, \dots, V_m)$  and  $|R_1|^2 = 1$  for  $z \ll 0$  by conservation of power for a lossless waveguide, cavity and slab. Finally, inserting (5.27) into (5.18) gives the  $M \times M$  matrix equation

$$[I + \Gamma \mathcal{D}] \mathbf{T} = \mathbf{t} \quad (5.29)$$

with

$$\mathcal{D} = -\hat{A} - \hat{D}\mu (I - \hat{C}\mu)^{-1} \hat{B} \quad (5.30)$$

and where  $\mathbf{t}$  is the vector of transmission coefficients and  $\Gamma$  is the matrix of reflection coefficients from the left and right problems respectively of appendix A. As was the case for the simple phase matrix  $\tilde{D}$  in the linear system for the empty cavity,  $\mathcal{D}$  is also a diagonal matrix, whose elements are much more complicated than those of  $\tilde{D}$  since they incorporate the electrical and thermal properties of the slab as determined by (5.21)-(5.25). Thus, using (5.28), the propagating electric field in region I is given by (5.12). Using the solution to (5.29) in (5.27) and (5.26), the propagating electric field in region II is given by (5.13) and in region IV by (5.14). As in the empty cavity case, mode symmetry about the wave guide and cavity axis requires  $T_n = 0$  for  $n$  even.

### 5.2.3 Solution of Linear System for Propagating Mode Amplitudes and Resonant Length Determination

In the case of a lossless slab, the  $J^{th}$  element of the  $M \times M$  matrix  $\mathcal{D}$  is greatly simplified if the slab width is an integral multiple of a half slab wavelength, that is,  $d = \frac{p\pi}{\chi_J(a)}$ , where  $\chi_J(a)$  is the cavity width dependent resonant propagation constant in a lossless slab and  $J$  is the resonant mode index in the  $x$  direction. For these specific slab widths, the  $J^{th}$  element of  $\mathcal{D}$  reduces to a simple phase constant of the same form as those determined for  $\tilde{D}$  in the empty cavity case; that is,  $\mathcal{D}_{JJ} = e^{2i\beta_J(l-d_p)}$  as if no slab were present in a cavity of length  $l - d_p$ . Unfortunately, the other elements of  $\mathcal{D}$  do not simplify in this manner; however, if  $M = 1$  or  $2$  we obtain explicit formulas for  $T_1$ ,  $l_r^{max}$  and  $l_r^{min}$  that are identical to (5.7), (5.8) and (5.9) respectively, except that  $l$  in (5.7) is replaced by  $l - d_p$  and  $d_p$  is added to the formulas for  $l_r^{max}$  and  $l_r^{min}$  in (5.8) and (5.9). For  $M \geq 3$ , we encounter the same difficulties in determining resonant lengths for a loaded lossless cavity as we did for an empty cavity. We again must resort to a graphical search for perturbed resonant lengths in the vicinity of  $l_{cc} + d$  where  $d$  can be any slab width.

### 5.2.4 Solution for Leading Order Electric Field in Slab

We now may completely determine a solution to (5.15). To obtain the solution in the form of (5.16), we first let

$$u_0 = \sum_{n=1}^{\infty} T_n e^{i\beta_n q} \Lambda_n(z) \phi_n(x) \quad (5.31)$$

where the  $\Lambda_n$  are to be determined. Inserting this ansatz into (5.15) and equating to zero the coefficients of the  $\phi_n$  gives

$$\frac{d^2}{dz^2} \Lambda_n + \theta_n^2 \Lambda_n = 0, \quad q < z < q + d. \quad (5.32)$$

In (5.31) the  $e^{i\beta_n q}$  are factored out for algebraic convenience in determining the boundary conditions as follows: At  $z = q$ , continuity of the tangential electric fields  $u_0$  and  $u_c$  in region *II* given by (5.13) gives

$$\Lambda_n(q) - 1 - \rho_n e^{-2i\beta_n q} = 0, \quad (5.33)$$

while continuity of the tangential magnetic fields gives

$$\frac{d}{dz}\Lambda_n(q) - i\beta_n (1 - \rho_n e^{-2i\beta_n q}) = 0. \quad (5.34)$$

Combining these conditions to eliminate the  $\rho_n$ , we get

$$\frac{d}{dz}\Lambda_n(q) + i\beta_n \Lambda_n(q) = 2i\beta_n. \quad (5.35)$$

Similarly, continuity of the tangential electric fields at  $z = q + d$  gives

$$\Lambda_n(q + d) - \alpha_n [e^{i\beta_n d} - \mu_n e^{-i\beta_n(2q+d)}] = 0 \quad (5.36)$$

where we have used  $u_0$  and  $u_c$  in region *IV* given by (5.14); continuity of the tangential magnetic fields gives

$$\frac{d}{dz}\Lambda_n(q + d) - i\beta_n \alpha_n [e^{i\beta_n d} - \mu_n e^{-i\beta_n(2q+d)}] = 0. \quad (5.37)$$

Dividing (5.37) by (5.36) to eliminate the  $\alpha_n$ , we get

$$\frac{d}{dz}\Lambda_n(q + d) + \beta_n \cot[\beta_n(l - q - d)]\Lambda_n(q + d) = 0. \quad (5.38)$$

The solution of the boundary value problem determined by (5.32), (5.35) and (5.38) is readily found to be

$$\Lambda_n(z) = f_n e^{i\theta_n(z-q)} + g_n e^{-i\theta_n(z-q)} \quad (5.39)$$

where

$$f_n = \frac{2\beta_n Z_n}{\beta_n(Z_n + W_n) + \theta_n(Z_n - W_n)} \quad (5.40)$$

$$g_n = \frac{2\beta_n W_n}{\beta_n(Z_n + W_n) + \theta_n(Z_n - W_n)} \quad (5.41)$$

$$Z_n = e^{-i\theta_n d} \{\theta_n + i\beta_n \cot[\beta_n(l - q - d)]\} \quad (5.42)$$

$$W_n = e^{i\theta_n d} \{\theta_n - i\beta_n \cot[\beta_n(l - q - d)]\}. \quad (5.43)$$

Now with  $\Lambda_n(z)$  known in (5.31), we can express  $u_0$  in the form given by (5.16) with  $F_n = T_n f_n e^{i\beta_n q}$  and  $G_n = T_n g_n e^{i\beta_n q}$ ,

that is,

$$u_0(x, z; \tau) \approx \sum_{n=1}^M T_n e^{i\beta_n q} \left( f_n e^{i[\theta_n(\tau)](z-q)} + g_n e^{-i[\theta_n(\tau)](z-q)} \right) \phi_n(x) \quad (5.44)$$

where  $f_n$  and  $g_n$  are given by (5.40)-(5.43) and the  $T_n$  are determined as the solution to the linear system (5.29)-(5.30).

Finally, we note that equations (5.33) and (5.36) determine expressions for  $\rho_n$ , the reflection coefficients in region II, and  $\alpha_n$ , the transmission coefficients in region IV. These give identical results to those obtained for  $\rho_n$  and  $\alpha_n$  by scattering matrix methods. Also, (5.33) and (5.36) determine the condition that governs how far from the aperture the slab should be placed so that evanescent modes can be neglected in subsequent calculations.

## 5.3 Future Work

### 5.3.1 Large Cavity Widths ( $a \gg 1$ )

The uncertainty inherent in the numerical inversion of  $I + \Gamma \tilde{D}$  or  $I + \Gamma \mathcal{D}$  at resonant lengths for very large cavity widths,  $a$ , requires an alternate solution method to validate our graphical results. Instead of using the Galerkin approximation for the

electric field in the aperture, we can use a ray approximation for this field (i.e.,  $u(x, 0) \approx \psi_1(x)$  where  $\psi_1(x)$  is the incident mode for the left problem of appendix A or  $u(x, 0) \approx \phi_j(x)$   $j \in (1 \dots M)$  where  $\phi_j(x)$  is the incident mode for the right problem of appendix A) as an alternate means of determining the elements of the vector  $\mathbf{t}$  (left problem) and the matrix  $\Gamma$  (right problem). Then, without inverting the linear system, we can obtain an asymptotic approximation for the solution vector  $\mathbf{B}$  (empty cavity) or  $\mathbf{T}$  (loaded cavity) , valid at a resonant length when only one mode dominates. We expect that this approximation will only be valid when  $J \ll a$ , that is, when the dominant mode index is much less than  $a$ . Improvements in the accuracy of these asymptotically determined lengths and field magnitudes can be made by including diffraction contributions from the edges of the aperture. We can use this same asymptotic approach in the case of multiply resonant modes to determine these dominant mode amplitudes and the associated resonant length.

### 5.3.2 Inclusion of Evanescent Modes

Including an appropriate number of evanescent modes in the computation of the field in the cavity will give a more realistic picture of the field structure near the aperture. This will allow us to place the ceramic slab close to the aperture. We can then investigate the effect this has on the heating of the slab.

## CHAPTER 6

### SLAB TEMPERATURE AND ELECTRIC FIELD ANALYSIS

#### 6.1 Analysis of Steady State Leading Order Temperature and its Effect on the Electric Field

For the convenience of the reader, we restate the initial value problem for  $v_0$  given in chapter (4). It is

$$\frac{d}{d\tau}v_0 = 2L(v_0) + pf(v_0)\|u_0(v_0)\|^2 \quad (6.1)$$

$$\|u_0\|^2 = \frac{1}{ad} \int_{-a/2}^{a/2} \int_q^{q+d} |u_0|^2 dz dx \quad (6.2)$$

$$u_0(x, z; v_0) \approx \sum_{n=1}^M T_n e^{i\beta_n q} \left\{ f_n e^{i\theta_n(z-q)} + g_n e^{-i\theta_n(z-q)} \right\} \phi_n(x) \quad (6.3)$$

$$v_0(0) = 0 \quad (6.4)$$

where  $L(v_0) = -v_0 - \beta((v_0 + 1)^4 - 1)$  and the modal representation of  $u_0$  is the same as given by (5.44) with  $T_n$ ,  $f_n$ ,  $g_n$  and  $\theta_n$  also depending on  $v_0$ . This equation admits a steady state solution given by  $v_0 = v_s(p)$ , where  $v_s(p)$  is the implicit solution of

$$p = \frac{-2L(v_s)}{f(v_s)\|u_0(v_s)\|^2}. \quad (6.5)$$

Equation (6.5) equates the dimensionless power  $p$  to the ratio of the power lost at the surface and the power generated by the microwaves within the slab. The complicated non-linear dependence of  $u_0$  upon  $v_s$  is embodied in expression (6.3) via the  $T_n$  as determined by solution of the linear system (5.29)-(5.30), the  $f_n$  and  $g_n$  as given by expressions (5.40)-(5.43) and  $\theta_n = \sqrt{\chi_n^2 + in_1^2 \nu f(v_s)}$  with  $\chi_n^2 = n_1^2 - (n\pi/a)^2$ .

Using an exponential conductivity function of the form  $f(v_s) = e^{cv_s}$  for an appropriate choice of  $c$  as discussed in section (3.3) and fixing the thermal and electrical parameters of the problem, we investigate the  $S$  shaped steady state response curves generated by equation (6.5) for resonant  $TE_{J_0n}$  cavities of varying

widths containing a slab of thickness  $d$ , where  $d$  is taken to be one wavelength in a lossless slab, i.e.  $d = d_2 = \frac{2\pi}{\chi_J}$  with  $J$  odd indicating the number of half wavelengths between  $a/2$  and  $-a/2$ . The use of an idealized lossless slab closely approximates a low loss slab at ambient temperature.

For  $M = 1$  and 2, the  $z$  coordinate of the left slab face,  $q$ , is chosen so that the centerline of the slab is placed on the centerline of the loaded resonant cavity. This is possible since the resonant length is determined by an explicit formula that does not depend on  $q$ , i.e.,

$$l_r^{max} = l_{cc} + d - \frac{\pi}{2\beta_1} - \frac{1}{2\beta_1} \tan^{-1} \left( \frac{\text{Im } \gamma_{11}}{\text{Re } \gamma_{11}} \right) \quad (6.6)$$

where  $l_{cc} = \frac{n\pi}{\beta_1}$  is the closed cavity eigenlength for a square resonator first introduced in section (5.1.3).

For  $M \geq 3$ , the determination of the loaded resonant length does depend on  $q$  so we can not know the centerline of the cavity until after the slab has been placed in it. Therefore, in order to locate the centerline of the slab as closely as possible to the centerline of the loaded resonant cavity, we place the slab centerline at the midpoint of the distance  $l_{cc} + d$  from the aperture, where  $l_{cc} = a = \frac{n\pi}{\beta_J}$ . The resonant lengths we seek are then small perturbations from  $l_{cc} + d$  and the slab centerline will be nearly on the centerline of the cavity. Finally, we must also ensure that the slab face at  $z = q$  is far enough from the aperture that evanescent modes may be neglected without affecting our results. The following additional parameters are fixed in all examples:  $\beta = .01$ ,  $\nu = .0001$ ,  $c = .78$ ,  $k = 3\pi/2$ ,  $n_1 = 3k$ .

Before proceeding further, we include a brief explanation of the stability of the three branches of a steady state response curve. [Refer figures (6.1) and (6.2)]. From a straightforward analysis of equation (6.1), it is possible to deduce that the middle branch of an S curve is unstable whereas the lower and upper branches are stable. In other words, given a specific incident mode strength,  $E_0$  (i.e. a specific  $p$  since

$p = \sigma_A D E_0^2 / 2h_e T_A$ ) impinging on the slab at ambient temperature,  $v_0$  will evolve to a steady  $v_s$  on either the upper or lower branch. If the power level is increased an infinitesimal amount past the point where the lower branch transitions to the unstable middle branch, then the ceramic will experience a dramatic jump in temperature to a point on the upper branch, which may be a high enough temperature to melt the sample. This is the thermal runaway phenomenon discussed in [6] and [7].

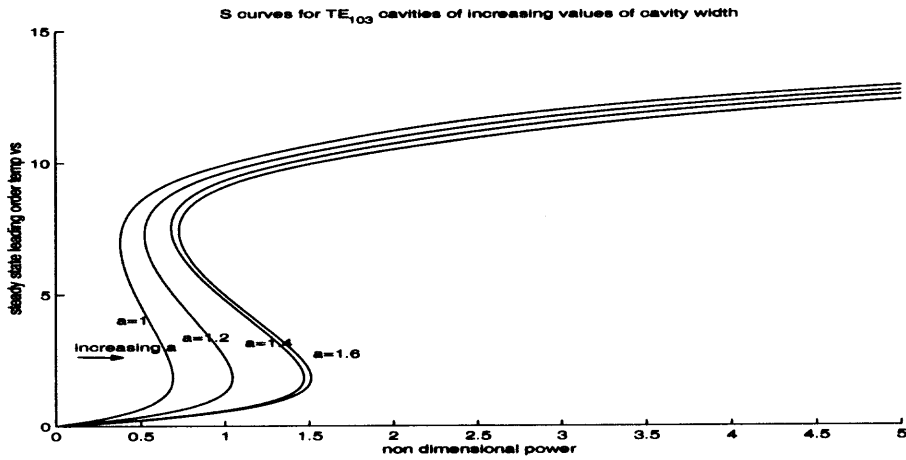


Figure 6.1 S curves for TE<sub>103</sub> cavities of increasing width when  $M = 1, 2$ .

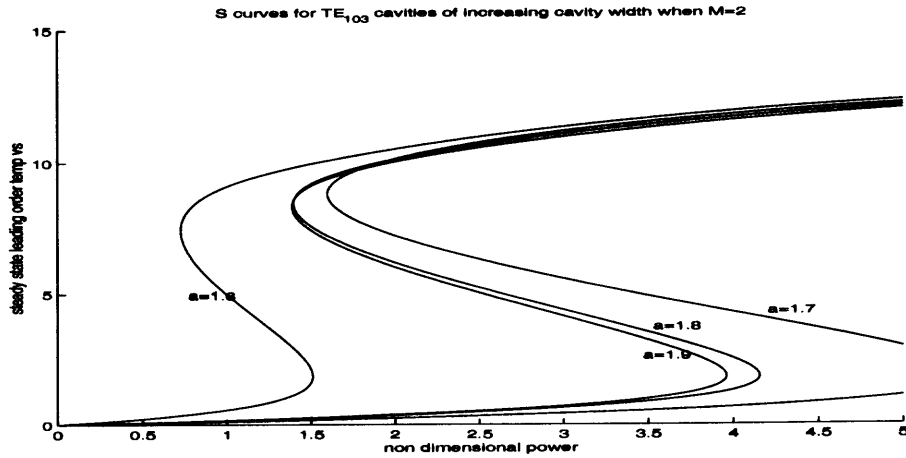


Figure 6.2 S curves for TE<sub>103</sub> cavities of increasing cavity width when  $M = 2$ .

### 6.1.1 Cases of $M = 1$ and $M = 2$

In Figure (6.1) are plotted steady state response curves for  $TE_{103}$  cavities of widths  $a = 1.2, 1.4$  and  $1.6$  with resonant lengths determined by equation (6.6) with  $n = 3$ . The  $a = 1$  curve, corresponding to a truncated waveguide, is included as a benchmark. In this case,  $M = 1$  and  $T_1 = 1$  in the expression for  $u_0$  given by (6.3); thus, it follows from (6.5) that the response curve has the same form as for the infinite slab considered in [6], which implies that the presence of the waveguide does not qualitatively alter the heating physics to leading order temperature. For  $1 < a < 2$ ,  $M = 1$  or  $M = 2$ , but  $|T_1| \neq 1$  so that the effect of the cavity is now incorporated in equation (6.5).

The existence of the upper branches of the curves in figures (6.1) and (6.2) is due to skin effect shielding. A dimensional analysis of the equation for the electric field in the slab shows that, for a specified  $v_s$ , the skin depth,  $L_s$ , is determined from the formula  $L_s = D / (d\sqrt{n_1^2\nu f(v_s)})$ , where  $D$  is the dimensional slab width and  $d$  depends on  $a$  via  $\chi_J$ . For  $v_s = 12$ , a physically attainable temperature on the upper branch of each of the curves,  $L_s \sim .15D$ , implying that the electric field is significantly attenuated within the slab [See Figure (6.3)], thereby allowing other steady state solutions to exist, i.e. the upper branches. On the lower branches, temperatures are low enough that skin effect shielding is negligible; that is, the skin depth is much larger than the slab width so that the electric field is essentially undamped in the slab.

In Figure (6.1), the progression of the curves to the right for increasing values of  $a$  indicates that the power required to produce a given steady state temperature within the slab increases as the cavity width increases to  $a = 1.6$ . This can be explained by the fact that the maximum magnitude of the resonant electric field within the slab at the ambient temperature actually decreases monotonically as  $a$  increases from 1 to 1.6. We expect, as  $a$  increases past 1.6, that the initial resonant

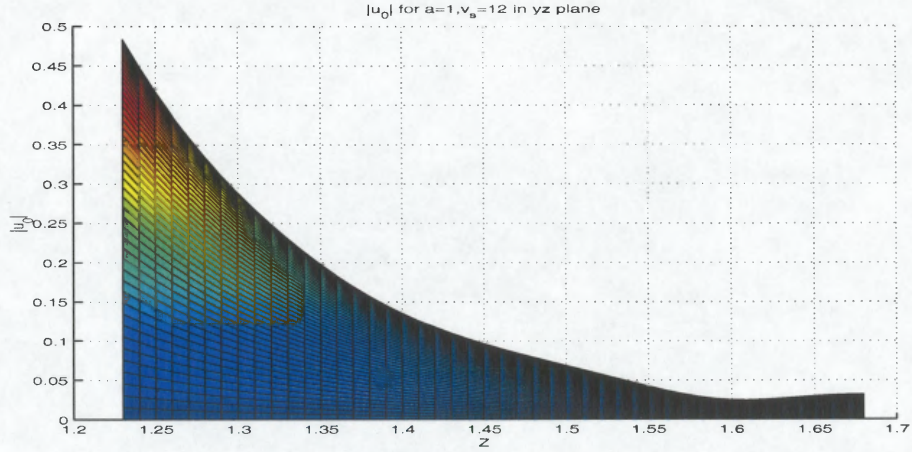


**Figure 6.3** Cross sectional illustration of skin effect on electric field within a slab of width  $a = 1$  heated to a steady state temperature  $v_s = 12$  on the upper branch of the S curve shown in Figure (6.1).

field in the slab eventually becomes large enough, as the applicator becomes more cavity-like, to cause the curves to reverse direction to the left. This is demonstrated in Figure (6.2) for  $a = 1.6, 1.7, 1.8$  and  $1.9$  where the power required to produce a given steady state temperature now decreases as the cavity width increases past  $a = 1.7$ . This direction reversal suggests that, for a given  $v_s$ , there is a specific cavity width that maximizes the amount of incident power required to reach that  $v_s$ ; this is a width that should be avoided in applications. From these results it is evident that a cavity with width slightly greater than its feeding waveguide is of no practical utility.

### 6.1.2 Case of $M \geq 3$

**6.1.2.1 Configuration.** In Figures (6.4) and (6.5) are plotted steady state response curves for resonant  $TE_{J01}$  cavities with  $J = M = 3, 5, 7, 9$  respectively.  $a$  is chosen such that  $a = l_{cc} = \frac{\pi}{\beta_M}$  and resonant lengths,  $l_r^{max}$ , are chosen as perturbations from  $l_{cc} + d$ . In Figure (6.4), the  $a = 1$  curve is again included as

a benchmark. Figure (6.5) is a plot of the curves of Figure (6.4) near the origin, excluding the  $a = 1$  curve.

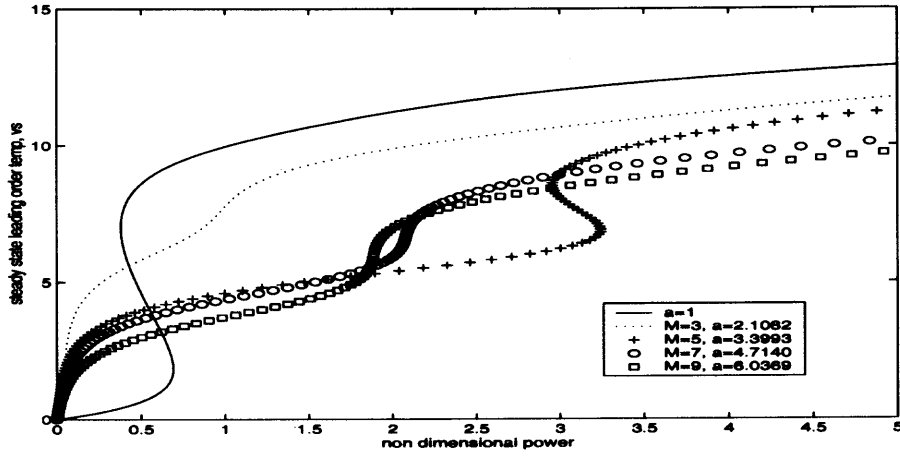


**Figure 6.4**  $S$  curves for  $TE_{J01}$  cavities with  $J = M$ .

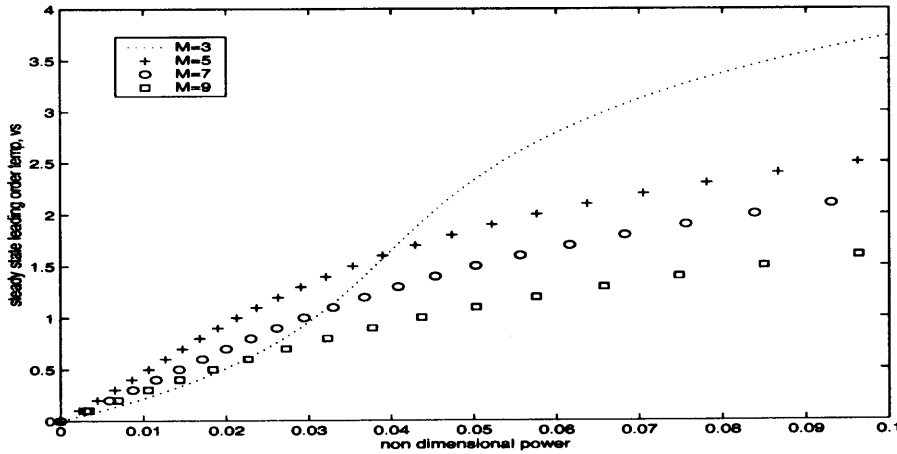


**Figure 6.5**  $S$  curves of Figure (6.4) near origin.

A representative contour plot of the magnitude of the electric field in a loaded lossless  $TE_{901}$  cavity is shown in Figure (6.6). For each  $M$ , the  $TE_{M01}$  mode is chosen to dominate in order to maintain consistency of field pattern when comparing  $S$  curves for cavities with widths corresponding to each value of  $M$ . The result is that placement of the slab centerline near the  $z$  centerline of the cavity is akin to

placing the slab centerline at or near the local maxima of the initial resonant field strength. We remind the reader that the depiction of the field near the aperture in Figure (6.6) is not realistic since evanescent modes have not been included in the computations. However, the slab has been placed far enough from the aperture (i.e., the condition  $e^{-|\beta_{M+1}|q} \ll 1$  has been satisfied) that these neglected evanescent modes are not significant with respect to computations within the slab (e.g. for  $M = 3$ ,  $e^{-|\beta_4|q} \sim .02$  and for  $M = 9$ ,  $e^{-|\beta_{10}|q} \sim .001$ )

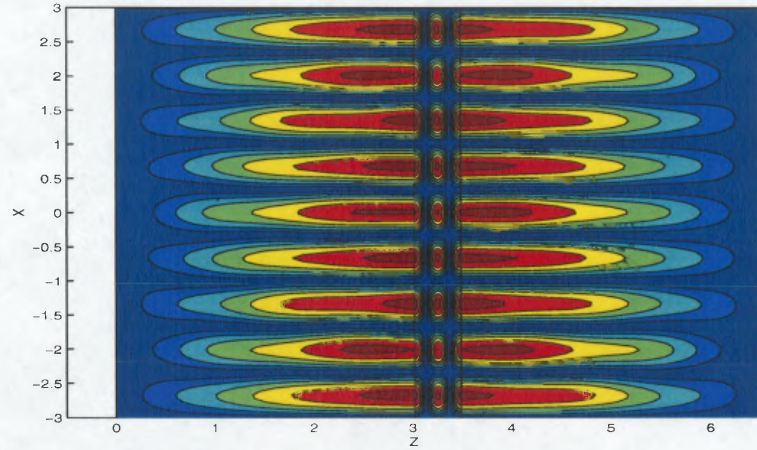


**Figure 6.6** Contour plot of magnitude of leading order electric field in loaded lossless  $TE_{901}$  cavity. Slab edges at  $z = q = 3.0185$  and  $z = q + d = 3.4895$ .  $l = l_r^{max} = 6.520$  and  $a = 6.0369$ .

**6.1.2.2 Discussion.** We first consider the curves of Figure (6.4) for  $0 < p < \sim .5$  where steady state temperatures for the cases of  $M \geq 3$  are much greater than those for the case of  $a = 1$ . This is due to the relatively large initial resonant fields attained in the slabs with  $M \geq 3$  as compared to the initial resonant field in the slab for the case of the truncated waveguide ( $a = 1$ ). Specifically, for  $M = 3, 5, 7$  and  $9$  the maximum values of the magnitudes of the initial resonant fields in the slab are  $\max |u_0(0)| \sim 15, 28, 25$  and  $32$  respectively, while the maximum value in the  $a = 1$  case is only  $\sim 2.6$ . So as  $M$  increases (i.e.,  $a$  increases), the applicator

becomes more cavity-like causing the initial resonant fields to become larger, albeit not in a monotonic manner. This deviation from monotonicity in the increase of the maximum values of  $|u_0(0)|$  with increasing cavity width may be due to the fact that the slab centerline is perturbed from the cavity centerline. If it were possible to place the slab centerline exactly in the center of the resonant cavity, then  $\max |u_0|$  would be maximized and a monotonically increasing sequence of these maxima could be obtained.

For a small expenditure of incident power, it is these large resonant fields that rapidly heat the slab, at least initially. As the slab heats, its temperature increases, which makes the electrical conductivity larger. The increase in the conductivity affects the  $f_n$  and  $g_n$  inside the slab, and the  $T_n$  inside the cavity but outside the slab in a complicated non-linear fashion as discussed in conjunction with the initial value problem for  $v_0$  listed at the beginning of section (6.1). These quantities, in turn, determine  $u_0$  in the slab in accordance with expression (6.3) with  $v_0$  eventually reaching a steady state  $v_s$ . Essentially, for lower branch values of  $v_s$ , the  $TE_{M01}$  mode of the electric field dominates, i.e.,  $|T_M| \gg |T_i|$ ,  $i \neq M$ . For upper branch values this is not the case; one or more different modes may dominate and drastically alter the field configuration in the loaded cavity. This is demonstrated shortly.

Another noticeable feature of the curves in Figure (6.4) for  $0 < p < . \sim 5$  is the decrease in the height of the curves as  $M$  increases. In other words, for a given  $v_s$ , the amount of incident power required to achieve that steady state temperature increases as  $M$  increases. This trend is clearly demonstrated in Figure (6.5) for  $v_s$  values in the range  $\sim 1.75 < v_s < \sim 3.75$  and  $p$  values in the range  $.04 \sim < p \leq .1$ . Taking  $v_s = 2$ , for example, the  $TE_{M01}$  mode remains dominant and, in fact, the field maxima retain the same relative heights with respect to one another, but the maximum values of the field amplitudes in the slab for  $M = 3, 5, 7$  and  $9$  have now decreased to  $|u_0(2)| = 11.6, 9.3, 7.7$  and  $5.6$  respectively. (Compare to  $|u_0(0)|$  values.) The

monotonic decrease in electric field amplitude as  $M$  increases is consistent with the observation that a larger  $p$  (i.e.  $E_0$ ) is required as  $M$  increases in order to achieve  $v_s = 2$ . Since skin depths for  $v_s = 2$  are  $\sim 7D$ , that is, seven times larger than the dimensional slab width, we can not attribute these reduced field strengths to skin effect shielding, but rather, to detuning of the cavity as the slab heats, so that less power actually gets to the load. Furthermore, as the value of  $M$  increases, the maximum field strengths for  $v_s = 2$  are reduced by 23% , 66%, 69%, and 82% from their ambient temperature values for  $M = 3, 5, 7$  and 9 respectively, which suggests that the cavity becomes more sensitive to detuning as  $M$  increases. This detuning phenomenon is also discussed in [7] for the case of a  $TE_{103}$  cavity with adjustable iris.

Now focusing on the region in Figure (6.5) where  $0 < v_s < \sim 1.75$  and  $p < \sim .04$ , it is evident, for  $p > \sim .02$ , that the  $M = 3$  curve increases more rapidly than the other curves, while for  $0 < p < \sim .02$ , it has approximately the same rate of increase but lies below the other curves. We may interpret this behavior as follows: For  $0 < p < \sim .02$ , the initial resonant field strength for the  $M = 3$  case,  $|u_0(0)| = 15$ , is significantly less than those for the  $M = 5, 7$  and 9 cases,  $|u_0(0)| = 28, 25, 32$  respectively; therefore, a lower steady state temperature is achieved for  $M = 3$ , i.e. this curve lies below the others. Nevertheless, for these small values of  $p$ , the effect of detuning for all four  $M$  values is about the same, hence, the similar slopes of the curves. But as the incident power increases past  $p = .02$ , the quenching of the initial resonant field by cavity detuning for  $M = 5, 7$  and 9 becomes more pronounced than quenching of the smaller initial resonant field for  $M = 3$ , the result of which is that the  $M = 3$  curve increases at a greater rate.

In Figure (6.5), taking  $v_s = .5$  for example, the maximum values of the field strengths in the slab for  $M = 3, 5, 7$  and 9 are now  $|u_0(.5)| = 13.8, 17, 14.7$  and 13 respectively, which are not monotonically decreasing as was the case for field

strengths with  $v_s = 2$ . The fact that the maximum  $|u_0|$  for  $v_s = .5$  occurs for  $M = 5$  may account for why the  $M = 5$  curve is the farthest left when  $v_s = .5$ ; that is, the cavity that maintains the largest field strength in the slab requires the smallest  $p$  value to reach  $v_s = .5$ . Evidently, for this value of  $v_s$ , the detuning effect has not yet become significant enough to push the  $M = 5, 7,$  and  $9$  curves to the right of the  $M = 3$  curve. Furthermore, as in the case of  $v_s = 2$ , there are reductions in the field strengths from the ambient temperature values with percentage decreases becoming larger as  $M$  increases, i.e. 8%, 39%, 41% and 59% for  $M = 3, 5, 7$  and  $9$  respectively. These reductions in field strength for a given  $v_s$  suggest that, as  $M$  increases, detuning becomes an increasingly significant inhibitor to the heating process even for very small values of  $p$  (and  $v_s$ ).

Finally, we consider the upper branches of the curves in figure (6.4). Taking  $v_s = 10$ , for example, skin depths for the curves with  $M \geq 3$  are  $\sim .3D$ , implying that skin effect shielding is the primary reason for the existence of the upper branches; however, the secondary effect of cavity detuning can also be discerned for upper branch temperatures. We can see this detuning effect for the particular case of a  $TE_{301}$  cavity when  $v_s = 10$  by comparing Figures (6.7) and (6.8) to Figures (6.9) and (6.10) respectively. Figure (6.10), a depiction of the magnitude of the electric field for  $v_s = 2$  in the loaded  $TE_{301}$  cavity with fixed dimensions  $l_r^{max} = 2.5225$  and  $a = 2.1082$ , is a three dimensional version of Figure (6.9). Figures (6.7) and (6.8) depict the magnitude of the electric field in the same loaded cavity when  $v_s = 10$ . The exact location of the slab is more easily discerned in the contour plots of figures (6.7) and (6.9).

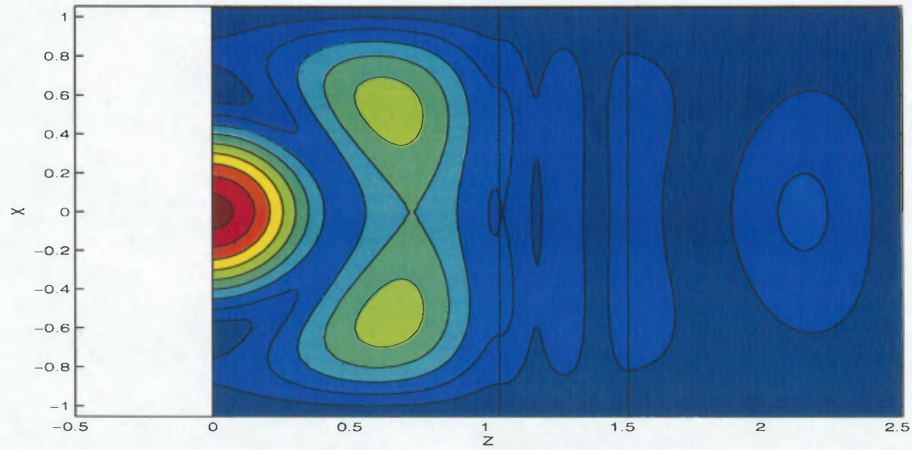


**Figure 6.7** Contour plot of magnitude of leading order electric field in loaded  $TE_{301}$  cavity with  $v_s = 10$ . Slab edges at  $z = q = 1.0541$  and  $z = q + d = 1.5226$ .  $l = l_r^{max} = 2.5225$  and  $a = 2.1082$ .

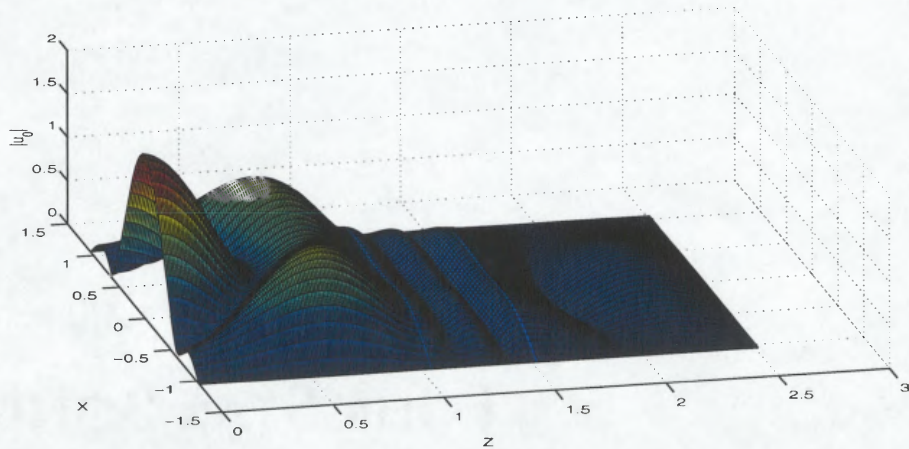


**Figure 6.8** Three dimensional version of Figure (6.7).

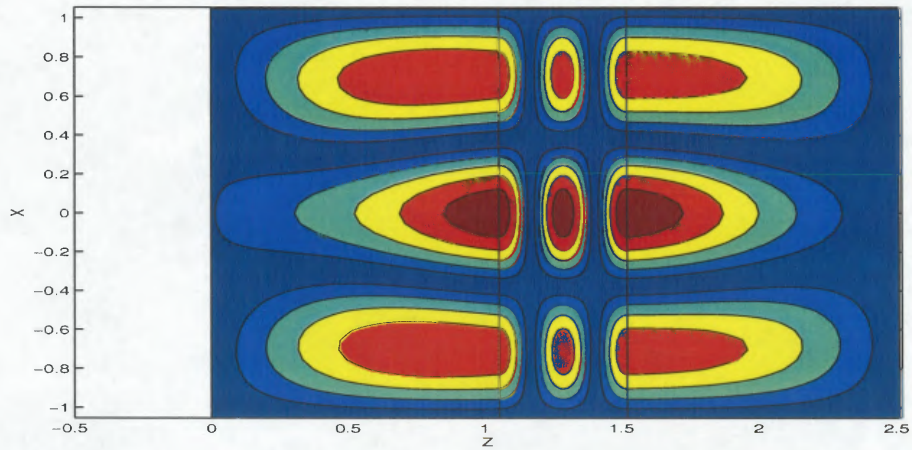


**Figure 6.9** Contour plot of magnitude of leading order electric field in loaded  $TE_{301}$  cavity with  $v_s = 2$ . Slab edges at  $z = q = 1.0541$  and  $z = q + d = 1.5226$ .  $l = l_r^{max} = 2.5225$  and  $a = 2.1082$ .

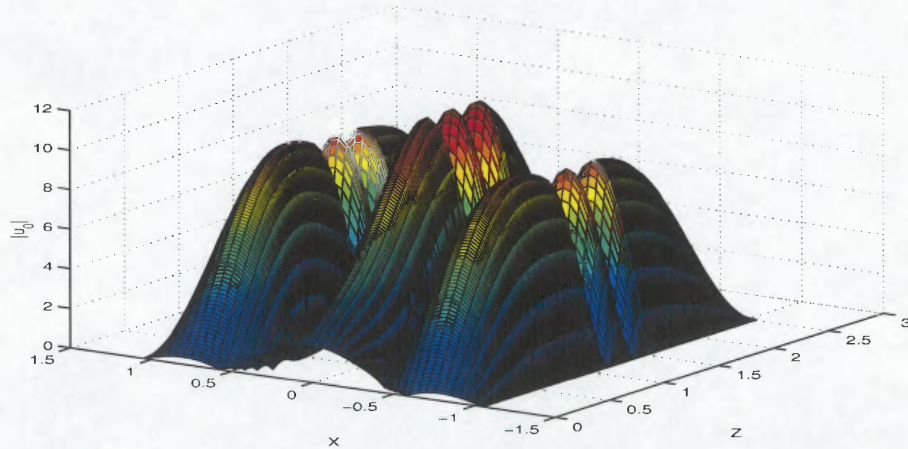


**Figure 6.10** Three dimensional version of Figure (6.9).

In figure (6.8), the influence of skin effect shielding on the electric field in the cavity is readily observed in the reduced field strength within the slab and cavity as well as in the “bunching” of the field to the side of the slab nearest the source. The effect of slab heating on cavity detuning, however, is observed in the change from a  $TE_{301}$  field pattern for temperatures on the lower branch of the  $M = 3$

curve of Figure (6.4) to a field pattern beginning to resemble that of a  $TE_{103}$  cavity, particularly within the slab, as demonstrated in figures (6.8) and (6.7). The reason for this metamorphosis is seen in the fact that  $|T_1| \sim |T_3|$  when  $v_s = 10$ , where  $T_1$  and  $T_3$  are the amplitude coefficients in the modal representation for  $u_0$  given by expression (6.3). That is, at this elevated temperature, the modal field strengths are of the same order of magnitude, giving the more amorphous field pattern of Figures (6.8) and (6.7), whereas for temperatures on the lower branch of the  $M = 3$  curve,  $|T_3| \gg |T_1|$ , giving the distinct  $TE_{301}$  pattern of Figures (6.9) and (6.10). The comparable contributions of the  $TE_{301}$  and  $TE_{103}$  modes can be seen more clearly in Figure (6.11), a plot of the field strength in the slab, which reveals local maxima of equal amplitude symmetric about the horizontal midline of the slab. These two modes have effectively combined to give a  $TE_{201}$  field pattern. On the other hand, it is skin effect shielding that has drastically reduced the field amplitude from  $\max |u_0(2)| = 11.6$  to  $\max |u_0(10)| = .45$  and determined that these maxima should reside near the left edge of the slab at  $Z_{\text{slab}} = 1.08$ ,  $X_{\text{slab}} = \pm .50$ .

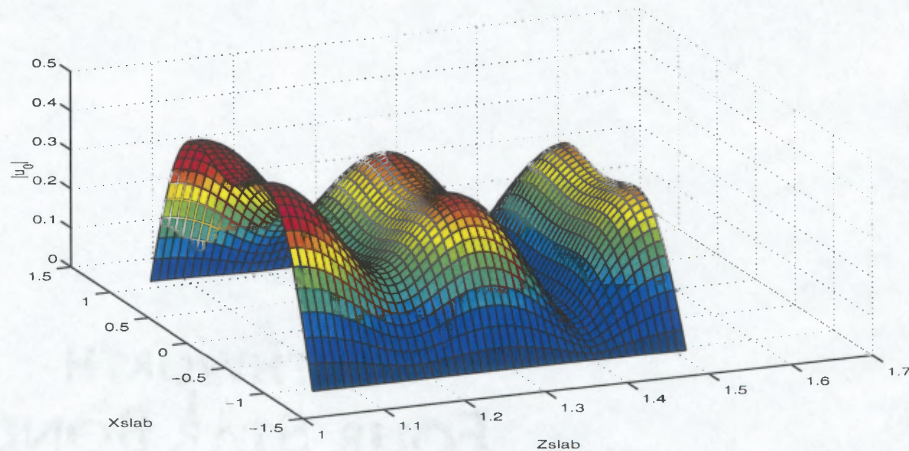


**Figure 6.11** Magnitude of leading order electric field in lossy slab of Figures (6.7) and (6.8) with  $v_s = 10$ .

For temperatures on the upper branches of the  $M = 5, 7$  and  $9$  curves of Figure (6.4), similar metamorphoses of field pattern occur as a result of cavity detuning, but the complicated non linear structure of the field prevents an a priori determination of the dominant field mode(s) for a given  $v_s$ . The maximum  $|u_0|$  at  $v_s = 10$  for  $M = 5, 7$ , and  $9$  are  $\sim .44, .34$ , and  $.34$  respectively, which demonstrates that skin effect shielding has essentially diminished the field strengths for these cases to the same order of magnitude. This is a reasonable result given that the skin depth for each case is in the vicinity of  $.3D$ .

### 6.1.3 Future Work

In subsequent work, we intend to analyze steady state temperature and its effect on the leading order electric field in the slab for larger values of  $M$ . The size of  $M$  will be limited by the computational resources required to solve an  $M \times M$  linear system for the field in the loaded cavity. We expect the upper branches of the corresponding  $S$  curves to be lowered in a manner similar to those for  $S$  curves considered by Kriegsmann in [7] for small iris openings in a  $TE_{103}$  cavity. In these cases, the existence of the upper branches was attributed to cavity detuning instead of skin effect shielding.

## 6.2 Analysis of Effect of Leading Order Temperature and Electric Field Distribution on Second Order Temperature Distribution

In the following analysis, we examine the generation of hot spots in the slab by considering the relationship between the magnitude of the leading order electric field ( $|u_0|$ ) and second order temperature( $v_1$ ) distributions for  $S$  curve lower and upper branch values of  $v_s$  in cavities with widths corresponding to those considered in section (6.1). We also provide preliminary evidence to support the experimental observation that the temperature of a heated object becomes more uniform as the mode number of the electric field within the object increases. More specifically,

for lower branch values of  $v_s$ , we show in a  $\text{TE}_{J01}$  cavity with  $J = M$ , that as  $M$  increases, the relative difference between the maximum and minimum second order temperatures within the slab becomes smaller, suggesting a trend toward uniformity.

We recall from chapter 4 that  $v_1$  satisfies the following two dimensional initial-boundary value problem:

$$\nabla^2 v_1(x, z; \tau) = \frac{1}{d^2} \left[ \frac{d}{d\tau} v_0 - pf(v_0) |u_0(x, z; v_0)|^2 \right], \quad (x, y, z) \in \mathbf{S} \quad (6.7)$$

$$\frac{\partial}{\partial z} v_1 = \frac{L(v_0)}{-d}, \quad z = q, \quad -a/2 < x < a/2, \quad 0 < y < h \quad (6.8)$$

$$\frac{\partial}{\partial z} v_1 = \frac{L(v_0)}{d}, \quad z = q + d, \quad -a/2 < x < a/2, \quad 0 < y < h \quad (6.9)$$

$$\frac{\partial}{\partial x} v_1 = 0, \quad x = \pm a/2, \quad q < z < q + d, \quad 0 < y < h \quad (6.10)$$

$$\frac{\partial}{\partial y} v_1 = 0, \quad y = 0, h, \quad q < z < q + d, \quad -a/2 < x < a/2 \quad (6.11)$$

$$v_1(x, z; 0) = 0 \quad (6.12)$$

where  $\mathbf{S}$  denotes the interior of the slab,  $L(v_0) = -v_0 - \beta((v_0 + 1)^4 - 1)$  and all other quantities are as originally defined in chapters (3) and (4). In appendix C, after assuming a steady state leading order temperature, we find a bounded, spatially dependent modal solution for  $v_1$  given by

$$v_1 = \left( \sum_{k=0}^{2M} A_k(z; v_s) \Upsilon_k(x) \right) - \frac{L(v_s)}{d} \left( 1 + \frac{2q}{d} \right) z + \frac{L(v_s)}{d^2} z^2 \quad (6.13)$$

where  $\Upsilon_k(x) = \cos[\lambda_k(x + \frac{a}{2})]$ ,  $\lambda_k = \frac{k\pi}{a}$  and each of the  $A_k$  are solutions to one or more of the equations (C.13)-(C.16), the choice of equation depending on the values of  $k$ , i.e.,  $k = 0, 2n, n + m$ , or  $|n - m|$ . The net result is that the  $A_k$  with  $k$  odd are zero so that the modal structure of  $v_1$ , like that of  $u_0$ , has even symmetry with respect to the horizontal midline of the slab. It must be emphasized that the following results obtained for  $v_1$  are only valid in materials where  $Bv_1 \ll v_s$  with  $B = h_e D / \kappa$ , the Biot number, as defined in chapter (3). This condition ensures that  $v \sim v_s + Bv_1$  is

a valid second order asymptotic approximation to the non dimensional temperature in the slab.

### 6.2.1 Case of $a = 1$

For this case, it is demonstrated that the presence of the waveguide clearly affects the second order temperature distribution in the slab, whereas its presence does not affect the leading order temperature. (Recall that this was demonstrated by the fact that the  $a = 1$   $S$  curve was identical to that for a slab of finite thickness in the  $z$  direction and infinite extent in the  $x$  direction.) The second order temperature and electric field distributions in the slab for this case are representative of those obtained for the  $TE_{103}$  cavities considered in section (6.1.1) for  $M = 1$  and  $M = 2$ .

We first consider a leading order temperature,  $v_s = .5$ , on the lower branch of the  $a = 1$  curve of Figure (6.1) . Figure (6.12) shows a contour plot of the magnitude of the electric field in the slab with three maxima of equal amplitude lying along the  $X_{slab} = 0$  line of symmetry. There is no perceptible difference from the field pattern for a lossless slab. Figures (6.13) and (6.14) show the corresponding symmetric contour and three dimensional plots of  $v_1$  with its maximum value,  $\max v_1 = 5.7$ , at the same location as the center maximum of the electric field. Although there are field peaks at the left and right edges of the slab, their contribution to heating is diminished by the radiative and convective heat loss governed by boundary conditions (6.8) and (6.9). The effect of this heat flux is manifested in the inverted parabolic shape of the  $v_1$  plot along the  $X_{slab} = \pm .5$  insulated edges of the slab as shown in Figure (6.14). This shape is consistent with the quadratic behavior in  $z$  demonstrated by the solution for  $v_1$  given by expression (6.13).

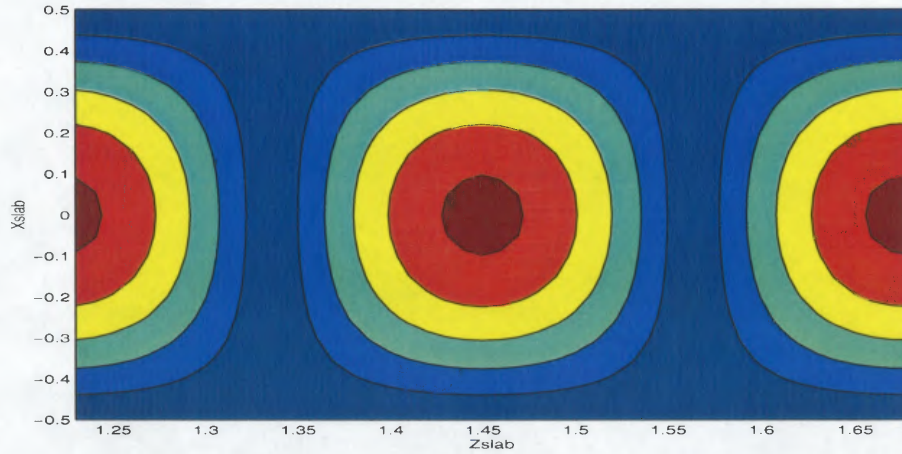


**Figure 6.12** Electric field strength within a slab of width  $a = 1$  heated to a steady state temperature  $v_s = .5$  on the lower branch of the  $S$  curve shown in Figures (6.1) and (6.4).

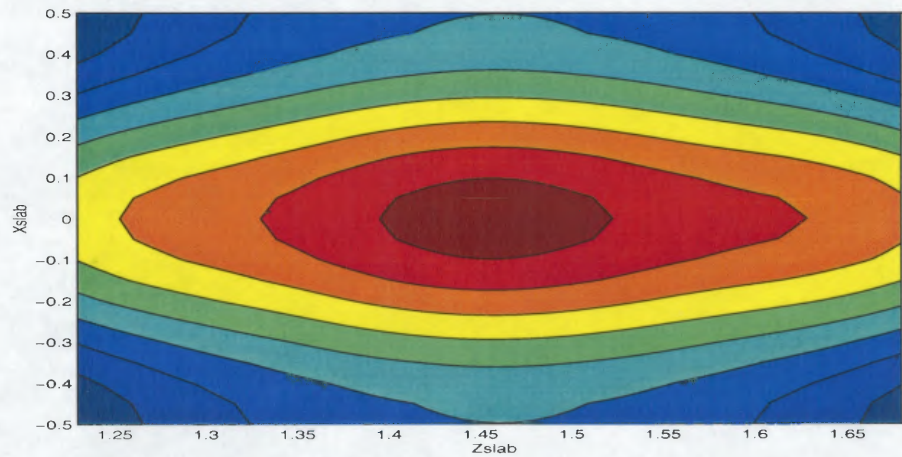


**Figure 6.13** Second order temperature,  $v_1$ , corresponding to Figure (6.12).

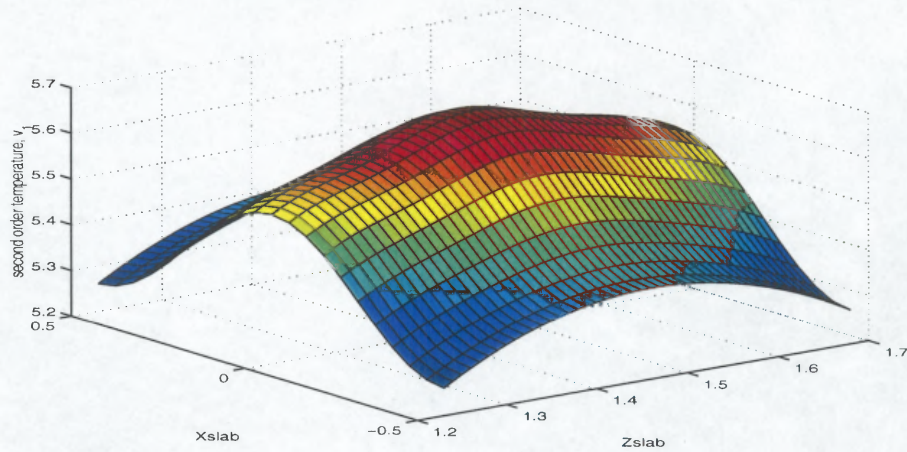


**Figure 6.14** Three dimensional version of Figure (6.13).

For  $v_s = 12$ , a physically attainable temperature on the upper branch of the  $a = 1$   $S$  curve, the maximum value of the electric field strength has decreased from  $\max |u_0| = 2.62$  at the three maxima indicated in figure (6.12) when  $v_s = .5$  to  $\max |u_0| = .48$  at the left edge of the slab ( $Z_{\text{slab}} = 1.23, X_{\text{slab}} = 0$ ) as shown in the contour plot of Figure (6.15). This Figure corresponds to Figure (6.3) of section (6.1), which is a cross sectional illustration of the skin effect within the same slab for  $v_s = 12$ . The influence of skin effect shielding has not only significantly decreased the field strength in the slab, but has shifted the maximum to the center of the edge nearest the source. Not surprisingly, the maximum of the second order temperature,  $\max v_1 = 3124$ , has shifted from the center of the slab to near the left edge ( $Z_{\text{slab}} = 1.26, X_{\text{slab}} = 0$ ) as demonstrated in the contour plot of figure (6.16). This does not exactly coincide with the location of the maximum of the electric field strength due to the effect of heat flux at the left slab face. Of course, the non dimensional temperature in the slab is not this high, but rather, is expressed to second order accuracy by  $v_s + Bv_1$ , as long as  $Bv_1 \ll v_s$ . Even so, depending on the material, this temperature may still be high enough to melt the ceramic so that the pattern for  $v_1$  just discussed is not applicable.

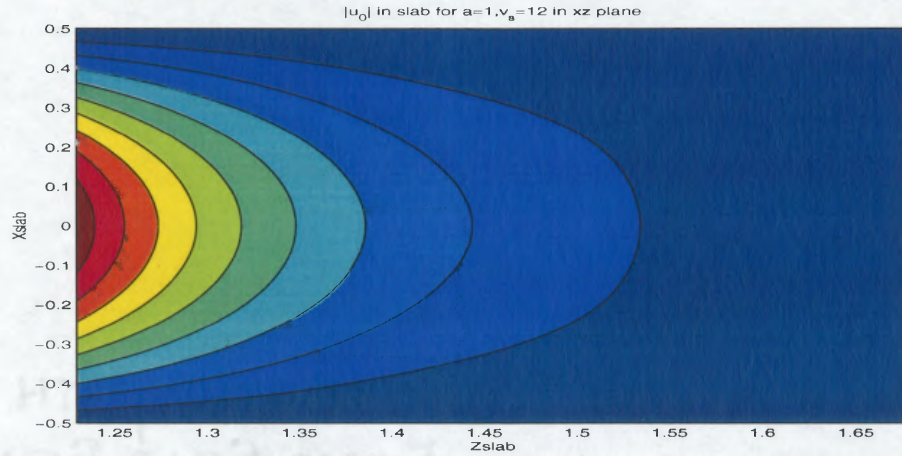


**Figure 6.15** Electric field strength within a slab of width  $a = 1$  heated to a steady state temperature  $v_s = 12$  on the upper branch of the  $S$  curve shown in Figures (6.1) and (6.4).

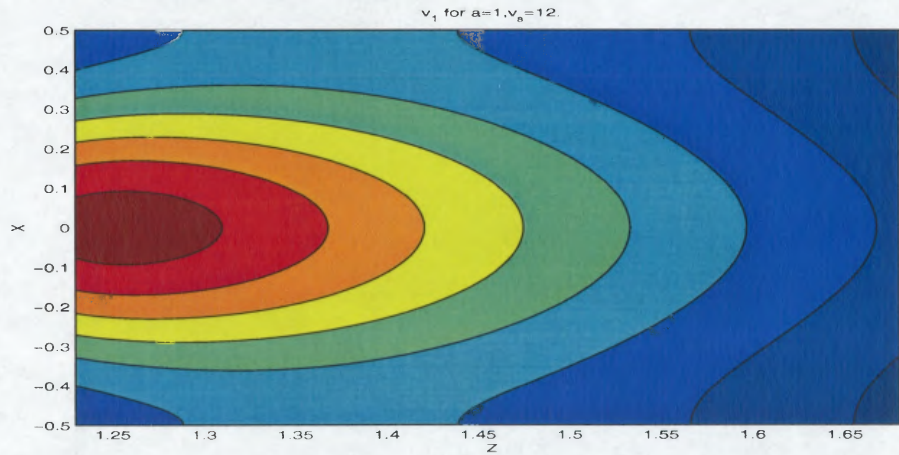


**Figure 6.16** Second order temperature corresponding to Figure (6.15).

### 6.2.2 Cases of $M \geq 3$

In contrast to the  $a = 1$  case for both upper and lower branch values of  $v_s$ , where the absolute maxima of the electric field strength and second order temperature were essentially co-located, we find that these maxima are not co-located within slabs contained in  $\text{TE}_{M01}$  cavities with  $M \geq 3$ . This relationship not only holds true for upper branch values of  $v_s$  where multiple modes can dominate the behavior of the electric field, but also for lower branch  $v_s$  values where the  $\text{TE}_{M01}$  mode remains dominant. For upper branch  $v_s$  values, the unpredictable behavior of the electric field again stymies any hope of predicting the location of the maximum of  $v_1$ .

An asymptotic analysis of the solution for  $v_1$  given by (6.13) helps to shed light on the low loss behavior of the second order temperature. Here, “low loss” refers to lower branch values of  $v_s$  where  $\text{Im } \theta_n \sim n_1^2 \nu f(v_s) / (2 \chi_n) \ll 1$ . Assuming that the  $A_k$  remain small enough, the terms in (6.13) containing  $L(v_s)$  and the last term of  $v_1(z)$  in the solution for  $A_0(z)$  containing  $L(v_s)$  [see appendix (C)] determine the magnitude of  $v_1$ . This is due to the fourth power dependence of  $L$  on  $v_s$ . As mentioned in conjunction with the solution for  $A_0(z)$  in the appendix, the large terms of  $A_0$  that depend upon  $\text{Im } \theta_n$  nearly cancel each other when  $\text{Im } \theta_n \ll 1$  and, therefore, do not make a significant contribution to  $v_1$ . An examination of the non-zero  $A_k, k \neq 0$  reveals that these amplitudes are composed of the sum of terms whose dominant behavior is governed by the solutions for the  $A_{2n}(z)$  with  $n \in (1, \dots, M)$  odd, which behave like  $|T_n|^2(|f_n|^2 + |g_n|^2) / \lambda_{2n}^2$  with  $\lambda_{2n}^2 = 4n^2\pi^2/a^2$ . In particular, we expect  $A_{2M}(z)$  to dominate the modal behavior of  $v_1$  since  $T_M$  is the dominant electric field mode amplitude and  $|T_M|^2(|f_M|^2 + |g_M|^2)$  is  $O(1)$  or greater depending on the value of  $M$ . While terms containing  $L(v_s)$  certainly remain dominant for upper branch values of  $v_s$ , a convenient asymptotic analysis of the  $A_k$  is not possible since it is not known a priori which, if any,  $|T_n|$  dominate. In this case,  $\text{Im } \theta_n \sim O(1)$

and we simply note that terms in the solutions for the  $A_k$  containing the factor  $e^{2(\text{Im } \theta_n)(z-q)}$  govern the modal behavior of  $v_1$ .

**6.2.2.1 Case of  $M = 3$ , lower branch.** We consider the  $\text{TE}_{301}$  resonant cavity of section (6.1) with dimensions  $a = 2.1082$ ,  $l_r^{\text{max}} = 2.5225$  containing a lossless slab of width one wavelength with its  $z$  centerline located near the cavity centerline. For  $v_s = 2$ , a lower branch leading order temperature, we have  $|T_3| = 5.3 \gg |T_1| = .93$ , so that the electric field in the slab retains its dominant mode structure as shown in Figure (6.17) with the three local maxima located along the  $X_{\text{slab}} = 0$  midline now visibly greater than the maxima at the  $X_{\text{slab}} = \pm a/2$  edges as shown in Figure (6.18). However, there is no corresponding dominant mode structure for  $v_1$ ; its absolute maxima are not located along the  $X_{\text{slab}} = 0$  midline. Figures (6.19)-(6.21) clearly show symmetric maxima of  $v_1$  centered in the  $Z_{\text{slab}}$  direction near the  $X_{\text{slab}} = \pm a/2$  edges.

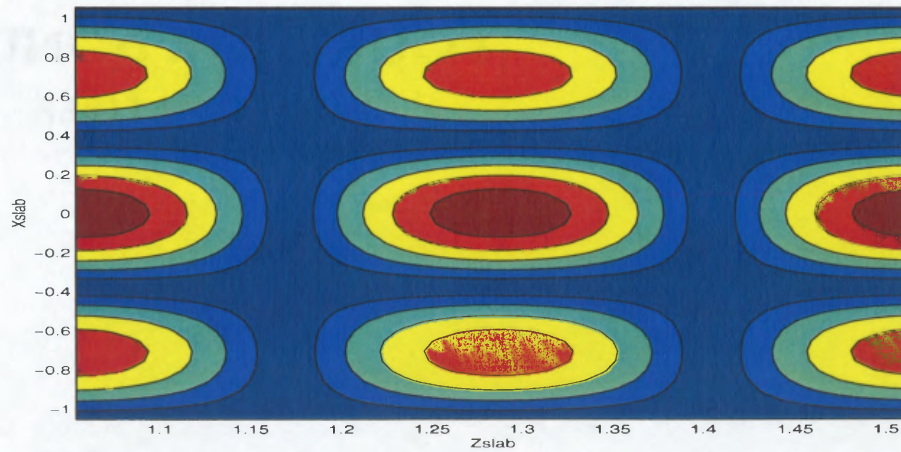


**Figure 6.17** Magnitude of leading order electric field in slab for  $M = 3$ ,  $a = l_{cc} = 2.1082$ ,  $v_s = 2$ .

A possible physical explanation for this disparity in the location of  $|u_0|$  and  $v_1$  maxima is as follows: The heat generated by the field maximum at the center of the slab has diffused toward the four slab boundaries. At the  $Z_{\text{slab}}$  boundaries,

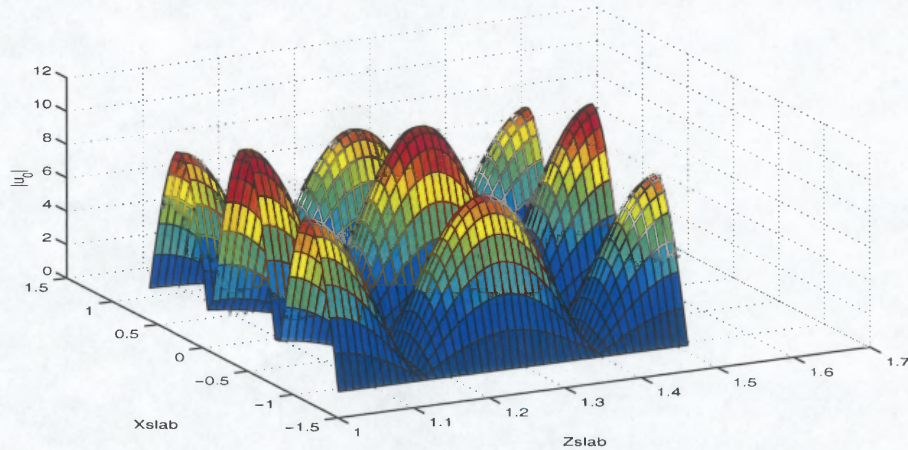


**Figure 6.18** Three dimensional version of Figure (6.17).

the heat is further dissipated by convective and radiative loss, while near the Xslab boundaries there are other local field maxima which generate hot spots sustained by their proximity to these insulated edges. Evidently, for the incident power level  $p = .045$ , corresponding to  $v_s = 2$ , the rates of heat diffusion from the slab center and heat loss at the Zslab boundaries combined with the absence of heat loss at the Xslab sides is greater than the rate at which power is absorbed along the Xslab=0 midline such that a lower temperature trough has evolved by the time leading order thermal equilibrium on the long convective time scale has been established at  $v_s = 2$ .

This physical behavior can be mathematically justified by an examination of the non-zero modes of  $v_1$ , with amplitude coefficients  $A_0, A_2, A_4, A_6$ . In particular, along the line  $z = q$ , the values of the coefficients are  $A_0 = 0, A_2 = .58, A_4 = -.17, A_6 = -.34$  (similar values hold along the midline of the slab) so that the superposition of the corresponding cosine functions in  $x$  gives the symmetric profile depicted in figure (6.21). The fact that the  $A_k, k = 2, 4, 6$  are all of comparable magnitude confirms the lack of a distinct mode structure for  $v_1$  corresponding to the dominant  $TE_{301}$  electric field mode. The existence of this correspondence would

require  $|A_6| \gg |A_2|$  and  $|A_4|$ . The diminished magnitude of  $A_6$  is probably due to the fact that  $|T_3|$  is only  $O(1)$ . Thus, for  $M = 3$ , the magnitude of  $v_1$  is governed by the terms in (6.13) containing  $L(v_s = 2) = -2.8$ , while the modal structure of  $v_1$  is determined by the sum of trigonometric terms of comparable amplitude.

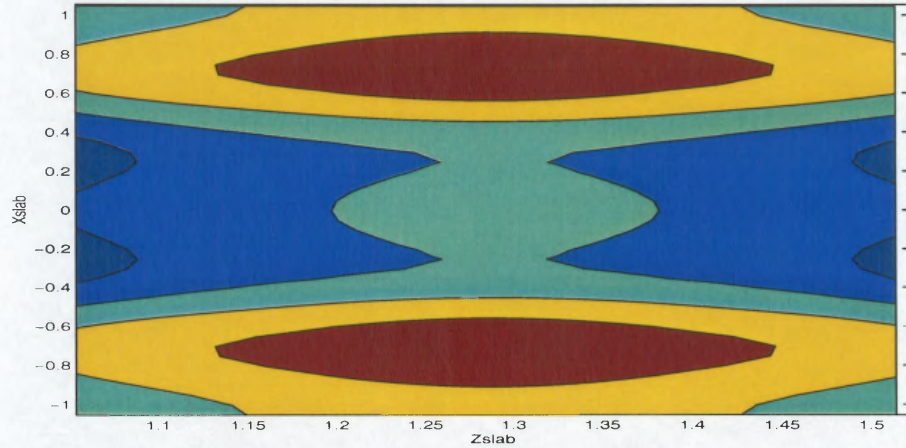


**Figure 6.19** Second order temperature in slab for  $M = 3$ ,  $a = l_{cc} = 2.1082$ ,  $v_s = 2$ . Maxima are located at  $Z_{slab} = 1.29$ ,  $X_{slab} = \pm 0.65$ .

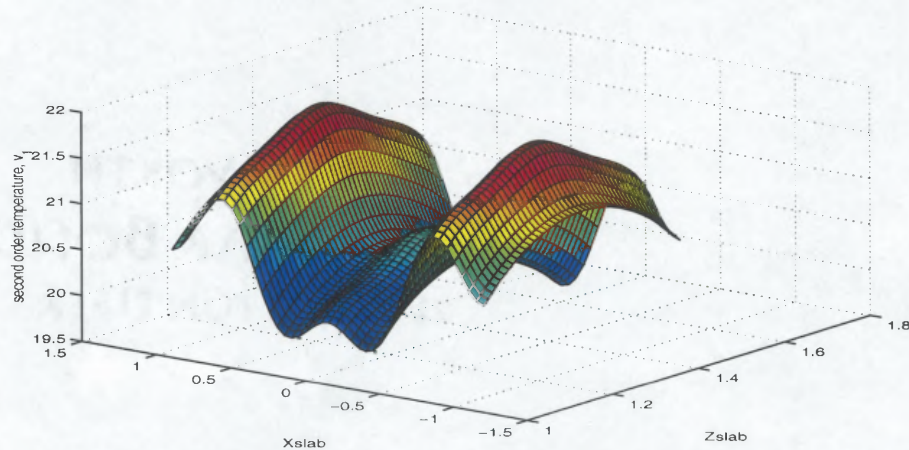


**Figure 6.20** Three dimensional version of (6.19).

**6.2.2.2 Case of  $M = 3$ , upper branch.** For  $v_s = 10$ , on the upper branch of the  $M = 3$   $S$  curve, skin effect shielding and cavity detuning have altered the electric

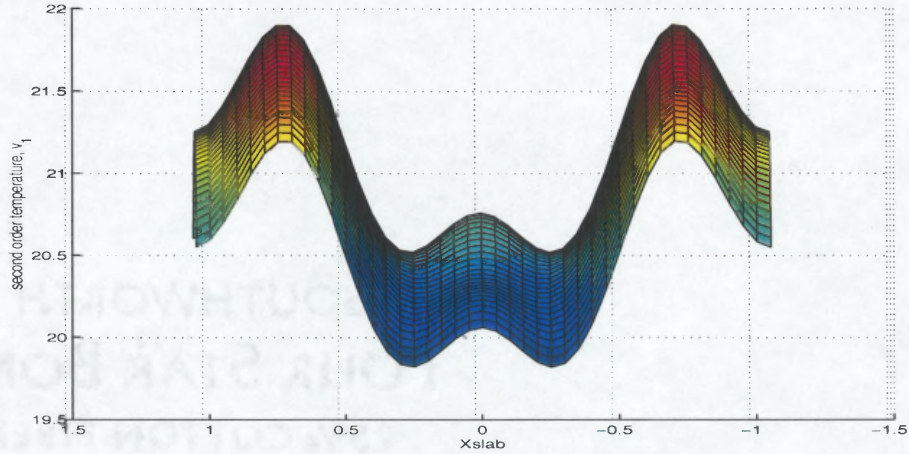


**Figure 6.21** Cross section of (6.20) in  $v_1$ -Xslab plane.

field in the slab as discussed near the end of section (6.1.2.2). A three dimensional plot of the field strength in the slab for  $v_s = 10$  was shown in Figure (6.11). For the reader's convenience, we include a two dimensional version in figure (6.22), which shows the symmetric maxima occurring near the left edge of the slab. The contour and three dimensional plots of  $v_1$  are shown in Figures (6.23) and (6.24) respectively. Although  $v_1$  has dramatically increased to a maximum of  $v_1 = 1237$  from a maximum of  $v_1 = 22$  when  $v_s = 2$ , its distribution in the slab is similar to that for  $v_s = 2$ , except that skin effect shielding has shifted the  $v_1$  maxima to the left. This behavior occurs despite the drastic reduction in electric field strength ( $|T_3| \sim |T_1| = O(10^{-1})$ ) and metamorphosis of the field pattern. Along the line  $z = q$ , the values of the modal temperature coefficients are  $A_0 = 0$ ,  $A_2 = 38$ ,  $A_4 = 35$ ,  $A_6 = -1.2$  (along the midline of the slab they are  $-16.5$ ,  $38$ ,  $28$ , and  $-.82$  respectively). Although the terms in expression (6.13) for  $v_1$  containing  $L(v_s = 10) = -156$  still dominate, we can not determine the asymptotic behavior of the  $A_k$  in terms of the dominant electric field mode as discussed in the low loss case. Nevertheless, we invoke the same

physical reasoning as was used in the  $v_s = 2$  case to explain why the  $v_1$  distribution looks as it does here.

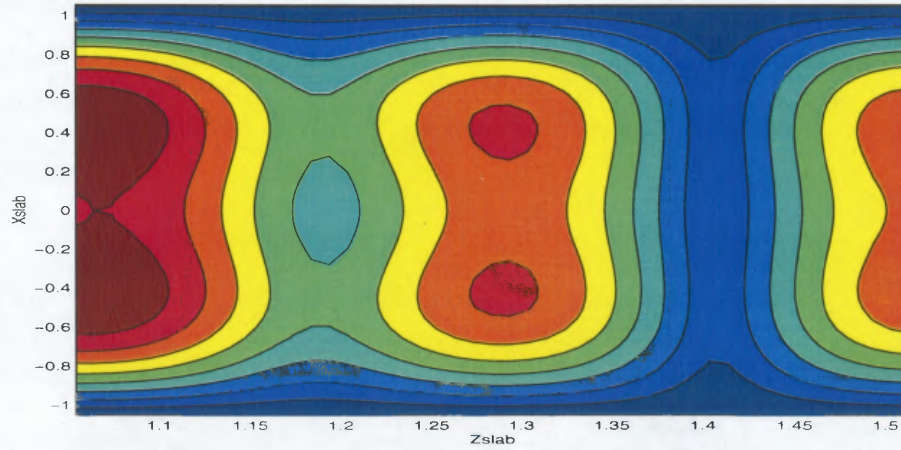


**Figure 6.22** Magnitude of leading order electric field in slab for  $M = 3, a = l_{cc} = 2.1082, v_s = 10$ . Maxima are located at  $Z_{slab} = 1.08, X_{slab} = \pm 0.5$ .

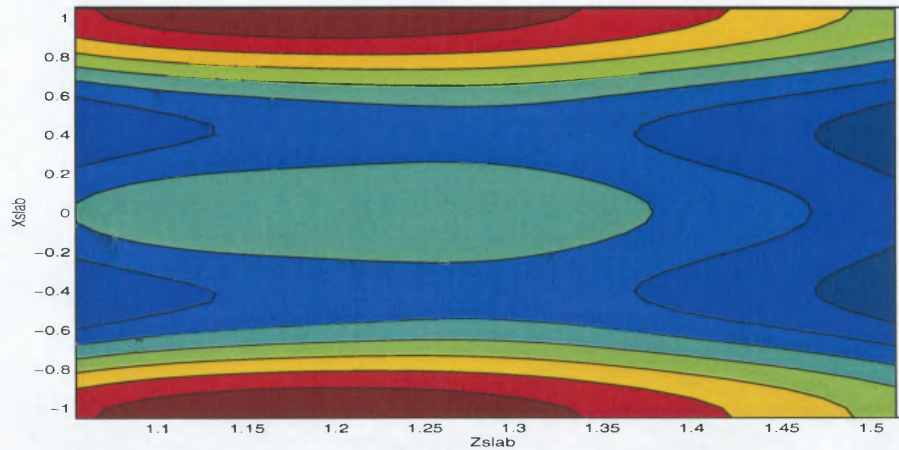


**Figure 6.23** Second order temperature in slab for  $M = 3, a = l_{cc} = 2.1082, v_s = 10$ . Maxima are located at  $Z_{slab} = 1.19, X_{slab} = \pm 1.0$ .

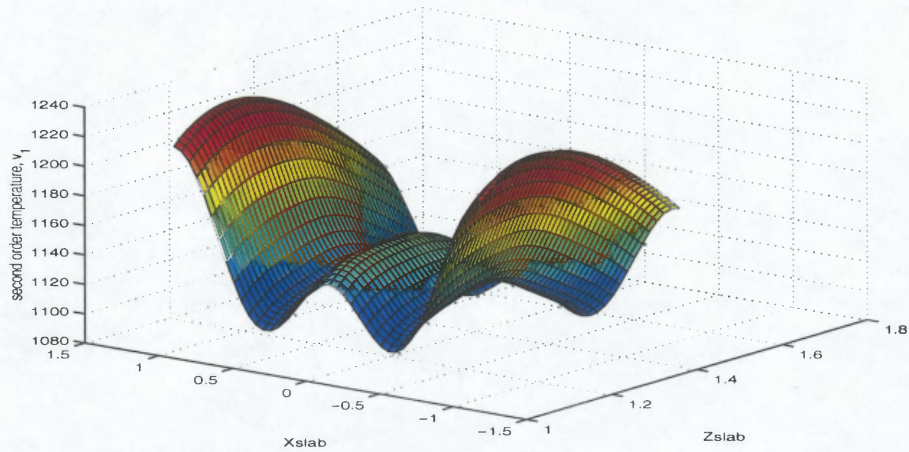


**Figure 6.24** Three dimensional version of Figure (6.23).

**6.2.2.3 Cases of  $M = 5, 7,$  and  $9,$  lower branch.** For  $v_s = 2,$  as  $M$  increases, we detect a change in configuration for  $v_1.$  When  $M = 5,$  it is apparent from Figure (6.27) that  $v_1$  has attained a distinct  $5 \times 1$  modal structure corresponding to the dominant mode structure of  $|u_0|.$  In fact, Figures (6.25) and (6.26), which are cross sections of  $v_1$  and  $|u_0|$  respectively in the  $v_1$ -Xslab plane, show that their peaks and valleys coincide. This distinct structure in  $v_1$  is corroborated by the fact that  $A_{10}$  is the largest modal amplitude, which is consistent with the asymptotic results discussed above. Despite the structural similarity between  $v_1$  and  $|u_0|,$  the location of the absolute maxima of  $v_1$  near the insulated edges of the slab ( $Z_{\text{slab}} = 1.95,$   $X_{\text{slab}} = \pm 1.4$ ) differs from the locations of the absolute maxima of  $|u_0|$  ( $Z_{\text{slab}} = 1.70, 1.93, 2.16,$   $X_{\text{slab}} = \pm 0.65$ ), although the relative difference between all  $|u_0|$  maxima is quite small as evidenced by Figure (6.26).

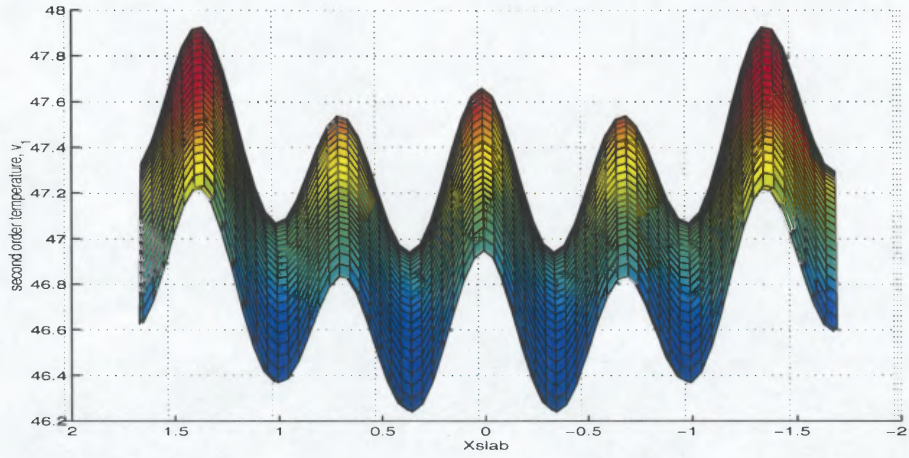


Figure 6.25 Cross section of Figure (6.27) in  $v_1$ -Xslab plane.

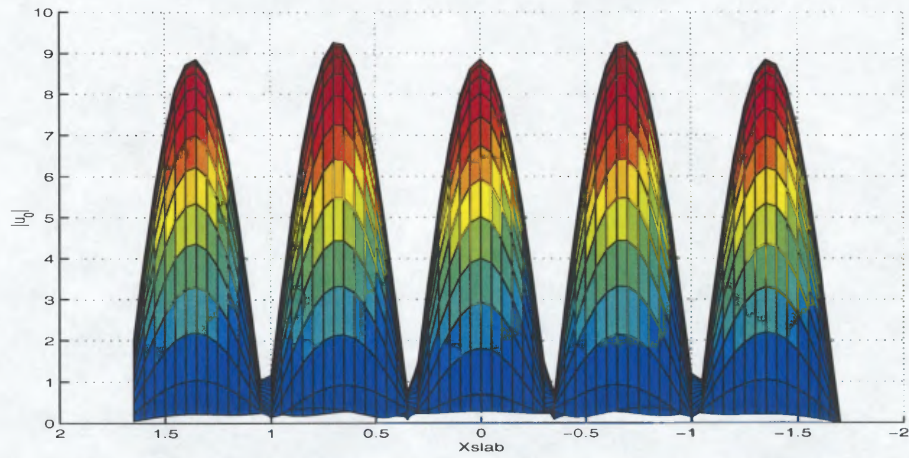
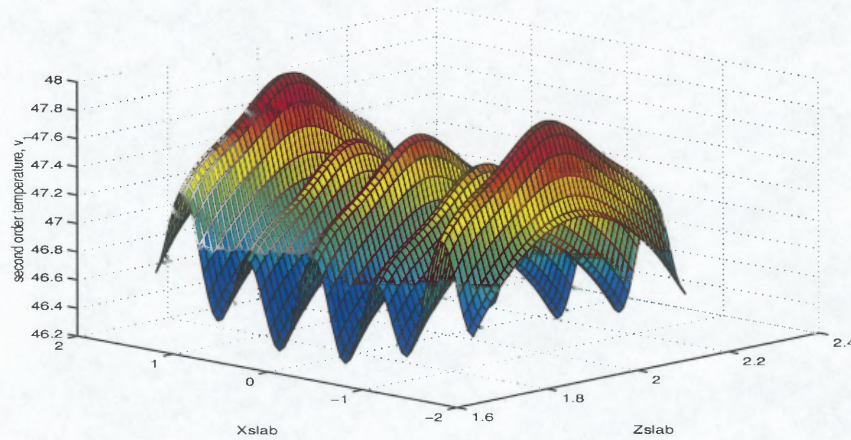


Figure 6.26 Cross section of leading order electric field magnitude in  $|u_0|$ -Xslab plane for  $M = 5$ .



**Figure 6.27** Second order temperature in slab for  $M = 5$ ,  $a = l_{cc} = 3.3993$ ,  $v_s = 2$ .

This disparity in the locations of field and temperature absolute maxima is similar to the one obtained in the  $M = 3$  case in that the absolute maxima of  $v_1$  were also located near the insulated edges while the absolute maxima of the electric field strength were located on the horizontal midline of the slab. In contrast to the  $M = 3$  case, which displayed only a weak  $3 \times 1$  mode structure in  $v_1$ , the three smaller interior maxima of  $v_1$  for  $M = 5$  are more prominent relative to the two absolute maxima of  $v_1$ . These two absolute maxima are about .8% higher than the other three local maxima, while for  $M = 3$  the absolute maxima of  $v_1$  were about 5% higher than the single interior maximum. The presence of three local  $v_1$  maxima in the interior of the slab coincident with three  $|u_0|$  maxima and the decrease in the relative difference between the  $v_1$  local maxima heights and the heights of the two  $v_1$  absolute maxima when compared to the  $M = 3$  case suggest that the rate of heat generation in the interior of the slab now provides a more significant counterbalance to the rate of heat loss at the  $z$  slab faces and to the heat retention at the insulated sides. In other words, the temperature trough that was present in the  $M = 3$  case has significantly diminished.

In the case of  $M = 7$ , the dominant mode amplitudes are  $A_2 = .29$  and  $A_{14} = .31$  at the left edge of the slab. The value of the magnitude of  $A_2$  is not consistent with the asymptotics, but is certainly plausible, since the asymptotic analysis serves only as a guide to expected results. In Figure (6.28) we can see the mode structure in  $v_1$  with  $\max v_1$  now located at the center of the slab. As in the  $M = 5$  case, all  $v_1$  peaks and valleys coincide with those of  $|u_0|$  in the  $v_1$ -Xslab plane, although their absolute maxima are not coincident. The modal structure of  $v_1$  is consistent with the dominant  $A_2$  and  $A_{14}$  modes; that is, the  $A_2$  mode coupled with the heat flux at the Zslab boundaries determines that  $\max v_1$  lies in the center of the slab, while the  $A_{14}$  mode determines the oscillatory nature of  $v_1$ . Evidently, enough electric field maxima are now present in the interior of the slab so that  $\max v_1$  shifts from nearer the insulated edges of the slab to its center. Moreover, this behavior persists for the case of  $M = 9$  in which  $A_2$  and  $A_{18}$  are the dominant amplitudes. We expect this trend to continue for  $M > 9$ ; further investigation is required to confirm this.

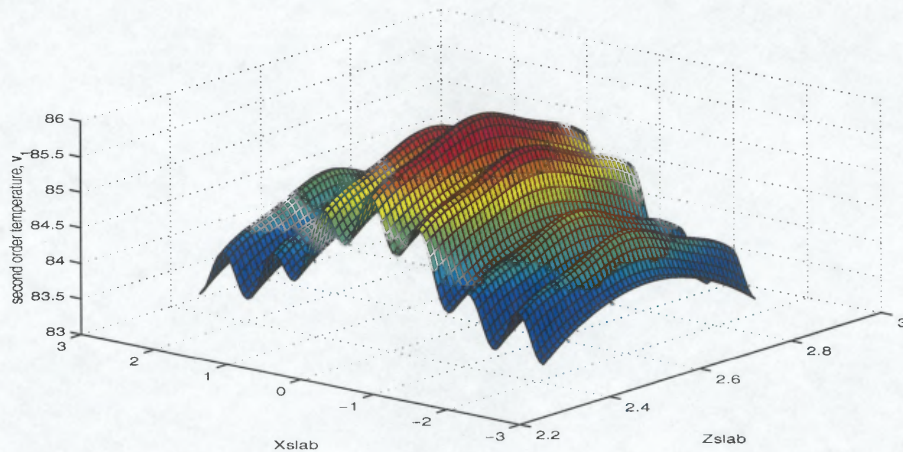


**Figure 6.28** Second order temperature in slab for  $M = 7$ ,  $a = l_{cc} = 4.7140$ ,  $v_s = 2$ .

In conclusion, despite the fact that the absolute maxima of  $v_1$  and  $|u_0|$  are not coincident for  $M \geq 3$  (at least in the cases discussed here), we were able to ascertain

that the absolute maximum of  $v_1$  shifted from double maxima near the insulated slab edges in the case of  $M = 3$  and  $M = 5$  to a single maximum in the center of the slab for  $M = 7$ ,  $M = 9$  and presumably for  $M > 9$ . This was due to the increase in the rate of heat generation in the interior of the slab. With respect to  $TE_{M01}$  cavities containing slabs heated to upper branch values of  $v_s$ , preliminary results suggest that the determination of a trend similar to that obtained for lower branch values of  $v_s$  is not possible due to the unpredictable nature of the electric field. We expect the location of hot spots to be coincident with electric field local maxima, but knowing the distribution of these field maxima is not predictable. Further investigation using increasing values of  $M$  is required in order to determine the existence of any trends.

**6.2.2.4 Uniformity of Slab Temperature.** Using the uniformity measure  $Uf = [(\max v_1 - \min v_1)/\max v_1] \times 100$  and taking  $v_s = 2$  in our  $TE_{M01}$  cavity for  $M = 3, 5, 7, 9$ , preliminary data show that  $Uf$  decreases monotonically as  $M$  increases as follows:  $M = 3$ ,  $Uf = 9.5\%$ ;  $M = 5$ ,  $Uf = 3.5\%$ ;  $M = 7$ ,  $Uf = 3\%$ ;  $M = 9$ ,  $Uf = 1.7\%$ . This evidence supports the experimental observation that the temperature of a heated object becomes more uniform as the number of electric field modes propagating within the object increases. For temperatures on the upper branch, e.g.  $v_s = 10$ , no such trend toward uniformity is observed as the following data suggests:  $M = 3$ ,  $Uf = 12\%$ ;  $M = 5$ ,  $Uf = 38\%$ ;  $M = 7$ ,  $Uf = 27\%$ ;  $M = 9$ ,  $Uf = 8\%$ . Further investigation is required for increasing  $M$  values to determine if  $Uf$  eventually decreases.

## APPENDIX A

### DERIVATION OF REFLECTION AND TRANSMISSION COEFFICIENTS FOR INFINITE STEPPED WAVEGUIDE

#### A.1 Summary of Method

Approximations for the coefficients can be found by using the continuity of the tangential electric and magnetic fields, i.e.  $u$  and  $\partial u/\partial z$ , across the infinite waveguide junction to derive an integral equation in terms of the unknown junction field  $u(x, 0)$ . Then, using an  $N$ -term sum of appropriately chosen basis functions to approximate  $u(x, 0)$  (with  $N \geq M$ , where  $M$  is the number of propagating modes for  $z > 0$ ), the integral equation can be solved for the unknown coefficients of the basis functions; this leads directly to the determination of the approximate values of the first  $N$  reflection and transmission coefficients for the left and right problems respectively.

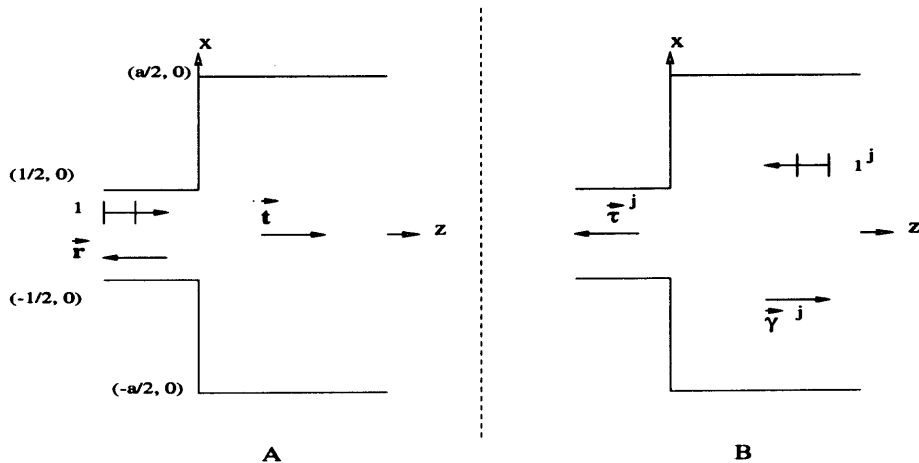


**Figure A.1** Infinite stepped waveguide junction. A: Incident wave from left. B:  $j^{\text{th}}$  incident wave from right.

#### A.2 Left Problem

Consider the left side of Figure (A.1). An incident plane wave of strength 1 impinges on the waveguide junction, which scatters a portion of the energy back down the waveguide of width 1 and transmits the remainder into the waveguide of width  $a$ .

In terms of non-dimensional variables and parameters, the solution to the Helmholtz equation with perfectly conducting boundary conditions is

$$u_L(x, z) = e^{ik_1 z} \psi_1(x) + \sum_{n=1}^{\infty} r_n e^{-ik_n z} \psi_n(x), \quad z < 0 \quad (\text{A.1})$$

$$= \sum_{n=1}^{\infty} t_n e^{i\beta_n z} \phi_n(x), \quad z > 0 \quad (\text{A.2})$$

where the  $r_n$  and  $t_n$  are unknown;  $\psi_n(x) = \sqrt{2} \sin[n\pi(x + 1/2)]$  with  $k_n = \sqrt{k^2 - n^2\pi^2}$  and  $\phi_n(x) = \sqrt{\frac{2}{a}} \sin[n\pi(x/a + 1/2)]$  with  $\beta_n = \sqrt{k^2 - n^2\pi^2/a^2}$ .  $k = W\omega/c \in (\pi, 2\pi)$  implies that  $k_1$  is real and corresponds to a single propagating mode in the waveguide for  $z < 0$  while  $k_n = i|k_n|$  for  $n \geq 2$  and correspond to evanescent modes in the waveguide for  $z < 0$ . Similarly,  $\beta_1, \dots, \beta_M$  are real and correspond to propagating modes in the waveguide for  $z > 0$ , while  $\beta_n = i|\beta_n|$  for  $n \geq M + 1$  and correspond to the evanescent modes in that portion of the waveguide.

From these solutions and continuity of the tangential electric and magnetic fields at the junction we get the relations

$$\psi_1(x) + \sum_{n=1}^{\infty} r_n \psi_n(x) = \sum_{n=1}^{\infty} t_n \phi_n(x) \quad (\text{A.3})$$

$$k_1 \psi_1(x) - \sum_{n=1}^{\infty} k_n r_n \psi_n(x) = \sum_{n=1}^{\infty} \beta_n t_n \phi_n(x), \quad (\text{A.4})$$

while orthonormality of the  $x$  eigenfunctions on their respective intervals and the fact that  $u = 0$  on the waveguide walls at  $z = 0^+$  allow the  $r_n$ 's and  $t_n$ 's to be represented in terms of the unknown electric field in the junction, i.e.,

$$r_n + \delta_{n1} = \int_{-1/2}^{1/2} u_L(x, 0^-) \psi_n(x) dx \quad (\text{A.5})$$

$$t_n = \int_{-1/2}^{1/2} u_L(x, 0^+) \phi_n(x) dx \quad (\text{A.6})$$

where  $\delta_{n1}$  is the Kronecker symbol.

Inserting (A.5) and (A.6) into (A.3) and interchanging the order of summation and integration gives the identity  $u_L(x, 0^-) = u_L(x, 0^+)$ ; inserting them into (A.4), we obtain the following integral equation in terms of the electric field in the junction,

$$\sum_{n=1}^{\infty} \left[ k_n \psi_n(x) \int_{-1/2}^{1/2} u_L(x', 0) \psi_n(x') dx' + \beta_n \phi_n(x) \int_{-1/2}^{1/2} u_L(x', 0) \phi_n(x') dx' \right] = 2k_1 \psi_1(x). \quad (\text{A.7})$$

Inspection of this equation reveals that interchange of summation and integration leads to an infinite sum that does not exist; therefore, we use Galerkin's method to obtain an approximate solution for  $u_L(x, 0)$  in terms of an orthonormal basis of eigenfunctions. Letting

$$u_L(x', 0) \approx \sum_{m=1}^N \eta_m \psi_m(x'), \quad N \geq M \quad (\text{A.8})$$

where the  $\eta_m$  are to be determined and substituting into (A.7), we obtain

$$\sum_{n=1}^{\infty} \left[ k_n \psi_n(x) \eta_n + \beta_n \phi_n(x) \left( \sum_{m=1}^N \eta_m K_{nm} \right) \right] \approx 2k_1 \psi_1(x) \quad (\text{A.9})$$

where, from (A.8),

$$\eta_n = \int_{-1/2}^{1/2} u_L(x', 0) \psi_n(x') dx' \quad (\text{A.10})$$

$$\sum_{m=1}^N \eta_m K_{nm} = \int_{-1/2}^{1/2} u_L(x', 0) \phi_n(x') dx' \quad (\text{A.11})$$

$$\text{with } K_{nm} = \int_{-1/2}^{1/2} \phi_n(x') \psi_m(x') dx'. \quad (\text{A.12})$$

To determine  $\boldsymbol{\eta} = (\eta_1, \dots, \eta_N)$ , we use (A.9) and the orthonormality of the  $\psi$  eigenfunctions on  $(-1/2, 1/2)$  to obtain the linear system

$$[D_{\mathbf{k}} + G] \boldsymbol{\eta} = 2k_1 \mathbf{e}_1 \quad (\text{A.13})$$

where  $\mathbf{e}_1 = (1, 0, \dots, 0)$  is of length  $N$ ;

$$D_{\mathbf{k}} = \begin{bmatrix} k_1 & 0 & \cdots & 0 \\ 0 & \ddots & \ddots & \vdots \\ \vdots & \ddots & \ddots & 0 \\ 0 & \cdots & 0 & k_N \end{bmatrix}, \quad G = \begin{bmatrix} G_{11} & \cdots & G_{1N} \\ \vdots & & \vdots \\ \vdots & & \vdots \\ G_{N1} & \cdots & G_{NN} \end{bmatrix}$$

with the elements of the symmetric complex mode coupling matrix  $G$  given by

$$G_{pm} = \sum_{n=1}^{\infty} \beta_n K_{nm} K_{np}, \quad p = 1, \dots, N, \quad m = 1, \dots, N, \quad N \geq M$$

and  $K_{nm}$  is defined in (A.12). For computational purposes, we truncate each infinite series element of  $G$  such that the number of terms used is at least as large as  $M$ , the number of propagating modes for  $z > 0$ . This is necessary in order to ensure sufficient accuracy of the propagating mode reflection coefficient,  $r_1$ , for  $z < 0$  and the propagating mode transmission coefficients,  $\mathbf{t} = (t_1, \dots, t_m)$ , for  $z > 0$ , derived below.

Finally, using the  $N$  Galerkin coefficients determined by equation (A.13) and inserting (A.8) into expressions (A.5) and (A.6), we find that the first  $N$  reflection and transmission coefficients in (A.1) and (A.2) respectively are

$$r_n(a, k) = \eta_n(a, k) - \delta_{n1} \quad \text{and} \quad t_n(a, k) = \sum_{m=1}^N \eta_m(a, k) K_{nm}(a), \quad n = 1, \dots, N, \quad (\text{A.14})$$

where the dependence on the cavity width,  $a$ , and wavenumber,  $k$ , are noted. We observe that the  $t_n$  with even numbered subscripts are zero for the following reason: The single mode incident from the left on the aperture is an even function with respect to  $x = 0$  and, therefore, generates transmitted modes in the larger portion of the guide that are also even functions with respect to this axis. The  $t_n$  associated with these modes have odd subscripts, while the  $t_n$  associated with the modes that are odd functions with respect to  $x = 0$  have even subscripts; hence, the even numbered  $t_n$  are zero in order to suppress the modes in the larger portion of the guide which are

odd functions in  $x$ . In particular, we use  $r_1$  and  $t_1, \dots, t_M$  in our scattering matrix formulation given by (5.4) and (5.5).

### A.3 Right Problem

Consider the right side of Figure (A.1) where the  $j^{\text{th}}$  incident plane wave of strength 1 impinges on the waveguide junction. Each  $j$  corresponds to each of the  $M$  propagating modes in the wider waveguide section so that the electric field is given by

$$u_R(x, z) = e^{-i\beta_j z} \phi_j(x) + \sum_{n=1}^{\infty} \gamma_{nj} e^{i\beta_n z} \phi_n(x), \quad z > 0 \quad (\text{A.15})$$

$$= \sum_{n=1}^{\infty} \tau_{nj} e^{-ik_n z} \psi_n(x), \quad z < 0. \quad (\text{A.16})$$

Using the procedure of the previous section, we obtain an integral equation for the aperture field,

$$\sum_{n=1}^{\infty} \left[ k_n \psi_n(x) \int_{-1/2}^{1/2} u_R(x', 0) \psi_n(x') dx' + \beta_n \phi_n(x) \int_{-1/2}^{1/2} u_R(x', 0) \phi_n(x') dx' \right] = 2\beta_j \phi_j(x), \quad (\text{A.17})$$

which can be converted to the  $N \times N$  linear system

$$[D_{\mathbf{k}} + G]\mathbf{s} = 2\beta_j \mathbf{e}_{\mathbf{p}}, \quad j = 1, \dots, M, \quad p = 1, \dots, N \quad N \geq M \quad (\text{A.18})$$

using the approximation  $u_R(x', 0) \approx \sum_{m=1}^N s_m \psi_m(x')$  and where  $D_{\mathbf{k}}$  and  $G$  are the same as given in (A.13) with  $K_{jp}$  given by (A.12).

Inserting the approximation for  $u_R$  in terms of  $s_m$  into

$$\gamma_{nj} + \delta_{nj} = \int_{-1/2}^{1/2} u_R(x', 0^+) \phi_n(x') dx' \quad (\text{A.19})$$

and

$$\tau_{nj} = \int_{-1/2}^{1/2} u_R(x', 0^-) \psi_n(x') dx', \quad (\text{A.20})$$

we find that

$$\tau_{nj}(a, k) = s_n(a, k) \quad (\text{A.21})$$

and

$$\gamma_{nj}(a, k) = \sum_{m=1}^N s_m(a, k) K_{nm}(a) - \delta_{nj}, \quad n = 1, \dots, N, \quad j = 1, \dots, M, \quad N \geq M, \quad (\text{A.22})$$

which give the first  $N$  terms of the series in (A.16) and (A.15) respectively. For each  $j$ , we observe that the  $\Gamma_{nj}$  and  $\tau_{nj}$ , which are generated by the  $j^{\text{th}}$  single mode incident on the aperture, have alternating zero and non-zero elements depending on whether  $j$  is even or odd, i.e. for  $j$  odd(even), the  $\Gamma_{nj}$  and  $\tau_{nj}$  with odd(even)  $n$  are non zero and the  $\Gamma_{nj}$  and  $\tau_{nj}$  with even(odd)  $n$  are zero. In particular, we use  $\tau_{1j}$  and  $\gamma_{nj}$  with  $n, j = 1, \dots, M$  in our scattering matrix formulation given by (5.4) and (5.5).

#### A.4 Conservation of Power

In [27], Amitay and Galindo showed that the reflection and transmission coefficients generated by an  $N$ -term Galerkin approximation of the electric field in a stepped waveguide junction satisfy the same power conservation law as the original continuous problem. Kriegsmann proved the same result for an  $N$  term Galerkin approximation of the electric field in the aperture of an iris situated in a waveguide of uniform width, regardless of the choice of basis functions or the size of  $N$ (as long as  $N \geq M$ )[28]. Furthermore, in both the continuous and discrete cases, he derived identical

conservation laws from the integral equation for the electric field in the aperture of the iris.

We can use either this method or the modal representation of the electric field in the junction together with the partial differential equation formulation of our scattering problem to determine the power conservation laws for the left and right problems described above. Considering only the propagating modes, we set  $N = M$  and find for the left problem

$$\frac{1}{k_1} \sum_{n=1}^M (\beta_n |t_n|^2) + |r_1|^2 = 1,$$

while for the right problem

$$\frac{1}{\beta_j} \left( \sum_{n=1}^M (\beta_n |\gamma_{nj}|^2) + k_1 |\tau_{1j}|^2 \right) = 1, \quad j = 1, \dots, M.$$

We use these equations to check the accuracy of our numerically computed reflection and transmission coefficients. However, as demonstrated in [27], we note that these relations are only necessary conditions and therefore, do not guarantee the accuracy of the coefficients. Nevertheless, we use them to check the validity of our results.

## APPENDIX B

### DERIVATION OF REFLECTION AND TRANSMISSION COEFFICIENTS FOR DIELECTRIC CERAMIC SLAB IN INFINITE WAVEGUIDE

#### B.1 Summary of Method

In the left and right cases, we use the continuity of the tangential electric and magnetic fields at the slab faces to derive a two point boundary value problem in the  $z$  variable of the electric field in the slab. From their solutions we find expressions for the reflection and transmission coefficients in the waveguide, i.e., the elements of the scattering matrix for the slab.

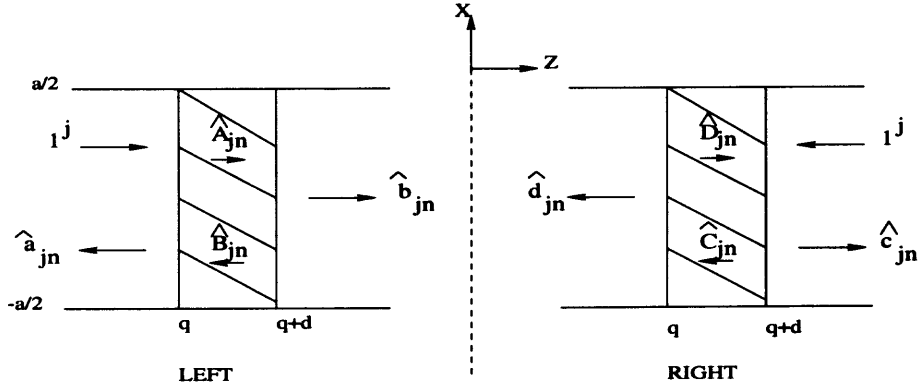


**Figure B.1** Ceramic slab in infinite waveguide of uniform width. A: incident wave from left. B: incident wave from right.

#### B.2 Derivation of Coefficients

Consider Figure (B.1) consisting of dielectric ceramic slabs situated in infinite perfectly conducting waveguides of width  $a$ . On the left(right) of the figure, the  $j^{th}$  incident plane wave of strength 1 impinges normally on the slab face at  $z = q(z = q + d)$ , which reflects a portion of the energy to the left(right) and transmits the remainder through the slab. Similarly, at  $z = q+d(z = q)$ , some energy is internally reflected and some is transmitted into the waveguide. The fractions

of incident electric energy transmitted and reflected depend on the temperature dependent effective electrical conductivity of the dielectric slab, which governs the power absorbed.

In terms of non dimensional variables and parameters and scattering matrix elements, the scalar electric field has the modal representation for the left problem

$$\hat{u}_L(x, z) = e^{i\beta_j z} \phi_j(x) + \sum_{n=1}^{\infty} \hat{a}_{jn} e^{-i\beta_n z} \phi_n(x), \quad j = 1, \dots, M, \quad z < q \quad (\text{B.1})$$

$$= \sum_{n=1}^{\infty} \hat{b}_{jn} e^{i\beta_n z} \phi_n(x), \quad j = 1, \dots, M, \quad z > q + d, \quad (\text{B.2})$$

and for the right problem

$$\hat{u}_R(x, z) = e^{-i\beta_j z} \phi_j(x) + \sum_{n=1}^{\infty} \hat{c}_{jn} e^{i\beta_n z} \phi_n(x), \quad j = 1, \dots, M, \quad z > q + d \quad (\text{B.3})$$

$$= \sum_{n=1}^{\infty} \hat{d}_{jn} e^{-i\beta_n z} \phi_n(x), \quad j = 1, \dots, M, \quad z < q. \quad (\text{B.4})$$

Note that these ansatzes are consistent with those used in section (5.2.1). In the slab the scalar electric field  $\tilde{u}_0(x, z; \tau)$  satisfies

$$\nabla^2 \tilde{u}_0 + n_1^2 [1 + i\nu f(v_0(\tau))] \tilde{u}_0 = 0. \quad (\text{B.5})$$

Letting

$$\tilde{u}_0(x, z; \tau) = \sum_{n=1}^{\infty} \tilde{\Omega}_{jn}(z; \tau) \phi_n(x) \quad (\text{B.6})$$

and substituting into (B.5) for each  $j = 1, \dots, M$  gives

$$\frac{d^2}{dz^2} \tilde{\Omega}_{jn} + \Theta_n^2 \tilde{\Omega}_{jn} = 0, \quad q < z < q + d \quad (\text{B.7})$$

with  $\Theta_n^2 = \chi_n^2 + in_1^2 \nu f(v_0(\tau))$  and  $\chi_n^2 = n_1^2 - n^2 \pi^2 / a^2$ .

Since the right problem is the mirror image of the left, we expect that  $\hat{b}_{jn} = (ph_1)\hat{d}_{jn}$  and  $\hat{a}_{jn} = (ph_2)\hat{c}_{jn}$  where  $ph_1$  and  $ph_2$  are phase constants. By choosing the appropriate ansatz in each region of the left(right) problem and in the slab, we can force  $ph_1 = ph_2 = 1$  so that it is necessary to solve only one problem. Therefore, we modify the ansatzes in (B.1)-(B.4) to

$$\begin{aligned}\tilde{u}_L(x, z) &= e^{i\beta_j(z-q)}\phi_j(x) + \sum_{n=1}^{\infty} \tilde{a}_{jn}e^{-i\beta_n(z-q)}\phi_n(x), \quad j = 1, \dots, M, \quad z < q \quad (\text{B.8}) \\ &= \sum_{n=1}^{\infty} \tilde{b}_{jn}e^{i\beta_n[z-(q+d)]}\phi_n(x), \quad j = 1, \dots, M, \quad z > q + d \quad (\text{B.9})\end{aligned}$$

and

$$\begin{aligned}\tilde{u}_R(x, z) &= e^{-i\beta_j[z-(q+d)]}\phi_j(x) + \sum_{n=1}^{\infty} \tilde{c}_{jn}e^{i\beta_n[z-(q+d)]}\phi_n(x), \quad j = 1, \dots, M, \quad z > q + d \quad (\text{B.10}) \\ &= \sum_{n=1}^{\infty} \tilde{d}_{jn}e^{-i\beta_n(z-q)}\phi_n(x), \quad j = 1, \dots, M, \quad z < q \quad (\text{B.11})\end{aligned}$$

Focusing our attention on the left problem, we use (B.8), (B.6) and the continuity of the tangential electric and magnetic fields at  $z = q$  to eliminate the  $\tilde{a}_{jn}$  and get the boundary condition

$$\frac{d}{dz}\tilde{\Omega}_{jn}(q) + i\beta_n\tilde{\Omega}_{jn}(q) = 2i\beta_n\delta_{jn} \quad (\text{B.12})$$

where  $\delta_{jn}$  is the Kronecker symbol. Similarly at  $z = q + d$  we use (B.10), (B.6) and the continuity conditions to eliminate the  $\tilde{b}_{jn}$  and get

$$\frac{d}{dz}\tilde{\Omega}_{jn}(q + d) - i\beta_n\tilde{\Omega}_{jn}(q + d) = 0. \quad (\text{B.13})$$

The solution to the two point boundary value problem given by (B.7), (B.12) and (B.13) is

$$\tilde{\Omega}_{jn}(z) = \tilde{A}_{jn}e^{i\theta_n(z-q)} + \tilde{B}_{jn}e^{-i\theta_n(z-q)} \quad (\text{B.14})$$

$$\text{with } \tilde{A}_{jn} = \frac{2\beta_n e^{-i\theta_n d}(\theta_n + \beta_n)\delta_{jn}}{\Delta_n}, \quad (\text{B.15})$$

$$\tilde{B}_{jn} = \frac{2\beta_n e^{i\theta_n d}(\theta_n - \beta_n)\delta_{jn}}{\Delta_n}, \quad (\text{B.16})$$

$$\text{and } \Delta_n = (\beta_n + \theta_n)^2 e^{-i\theta_n d} - (\beta_n - \theta_n)^2 e^{+i\theta_n d}. \quad (\text{B.17})$$

We now can find  $\tilde{a}_{jn}$  and  $\tilde{b}_{jn}$ . From the continuity of the tangential electric field at  $z = q + d$ , we have

$$\tilde{b}_{jn} = \tilde{\Omega}_{jn}(q + d), \quad (\text{B.18})$$

which simplifies to

$$\tilde{b}_{jn} = \frac{4\beta_n \theta_n \delta_{jn}}{\Delta_n} \quad j = 1, \dots, M; \quad (\text{B.19})$$

and from the continuity of the tangential electric and magnetic fields at  $z = q$ , we have

$$\tilde{a}_{jn} = \frac{\left(\frac{d}{dz}\tilde{\Omega}_{jn}(q) - i\beta_n\tilde{\Omega}_{jn}(q)\right)}{-2i\beta_n}, \quad (\text{B.20})$$

which simplifies to

$$\tilde{a}_{jn} = \frac{2i(\theta_n^2 - \beta_n^2) \sin(\theta_n d)\delta_{jn}}{\Delta_n}. \quad (\text{B.21})$$

Using (B.10) and (B.11) and letting  $\tilde{\Omega}_{jn} = \tilde{C}_{jn}e^{-i\theta_n[z-(q+d)]} + \tilde{D}_{jn}e^{i\theta_n[z-(q+d)]}$  instead of (B.14) shows that  $\tilde{C}_{jn} = \tilde{A}_{jn}$  and  $\tilde{D}_{jn} = \tilde{B}_{jn}$ , from which it follows that  $\tilde{c}_{jn} = \tilde{a}_{jn}$  and  $\tilde{d}_{jn} = \tilde{b}_{jn}$ .

To find the hatted scattering matrix elements used in (B.1)-(B.4), we need only multiply  $\tilde{u}_L$  and  $\tilde{u}_R$  by the appropriate phase constants to obtain  $\hat{u}_L$  and  $\hat{u}_R$  with

$$\hat{a}_{jj} = e^{2i\beta_j q} \tilde{a}_{jj} \quad (\text{B.22})$$

$$\hat{b}_{jj} = e^{-i\beta_j d} \tilde{b}_{jj} \quad (\text{B.23})$$

$$\hat{c}_{jj} = e^{-2i\beta_j(q+d)} \tilde{c}_{jj} \quad (\text{B.24})$$

$$\hat{d}_{jj} = e^{-i\beta_j d} \tilde{d}_{jj} \quad (\text{B.25})$$

where we use the fact that each coefficient is zero when  $j \neq n$ . Physically, this means that the  $j^{\text{th}}$  incident mode only excites the  $j^{\text{th}}$  reflected and transmitted modes inside and outside the slab.

### B.3 Conservation of Power for Lossless Slab

As in appendix A, we wish to use the conservation of power to verify the numerical accuracy of our scattering matrix elements. To this end, we use the well known result that the scattering matrix in the case of a **lossless** slab is unitary; that is,  $SS^H = I$  where

$$S = \begin{bmatrix} \hat{\mathbf{A}} & \hat{\mathbf{D}} \\ \hat{\mathbf{B}} & \hat{\mathbf{C}} \end{bmatrix},$$

$S^H$  is its Hermitian matrix and each block of  $S$  is an  $M \times M$  diagonal matrix composed of its corresponding elements given by (B.22)-(B.25). In particular, we use the following relationships to establish the validity of our results for each  $j \in (1, \dots, M)$ :

$$|\hat{a}_{jj}|^2 + |\hat{b}_{jj}|^2 = 1 \quad (\text{B.26})$$

$$|\hat{c}_{jj}|^2 + |\hat{d}_{jj}|^2 = 1 \quad (\text{B.27})$$

$$\hat{a}_{jj}\hat{d}_{jj}^* + \hat{d}_{jj}\hat{c}_{jj}^* = 0 \quad (\text{B.28})$$

$$\hat{d}_{jj}\hat{a}_{jj}^* + \hat{c}_{jj}\hat{b}_{jj}^* = 0 \quad (\text{B.29})$$

where  $*$  indicates the complex conjugate and  $\hat{b}_{jj} = \hat{d}_{jj}$  by the symmetry of the scattering matrix.

## APPENDIX C

### SOLUTION OF PARTIAL DIFFERENTIAL EQUATION FOR SECOND ORDER TEMPERATURE

#### C.1 Summary of Method

We solve a Poisson equation with inhomogeneous boundary conditions in  $z$  and no flux boundary conditions in  $x$  and  $y$  for  $v_1$ , the bounded second order correction in the small Biot number expansion of the slab temperature. Both the forcing term and the boundary conditions in  $z$  are parameterized by  $v_0(\tau)$ , the leading order temperature in the slab. This initial-boundary value problem was first stated in chapter 4. By a change of dependent variable, we convert to a Poisson equation in  $w$  with strictly homogeneous boundary conditions. After assuming a steady state leading order temperature, we find a solution by the method of eigenfunction expansion. The resulting infinite series coefficients in  $z$  are then determined by an infinite sequence of second order linear ordinary differential equations. A finite number of these series terms, depending on the value of  $M$ , the number of propagating modes in a lossless slab, are then sufficient to determine a bounded solution for  $v_1$ .

#### C.2 Transformation of Problem

Letting

$$v_1 = w - \frac{L(v_0)}{d} \left(1 + \frac{2q}{d}\right) z + \frac{L(v_0)}{d^2} z^2 \quad (C.1)$$

transforms the problem in  $v_1$  to one in  $w$  with homogeneous boundary conditions, that is,

$$\nabla^2 w = \frac{1}{d^2} \left[ \frac{d}{d\tau} v_0 - pf|u_0|^2 - 2L \right], \quad (x, y, z) \in \mathbf{S} \quad (C.2)$$

$$\frac{\partial}{\partial z} w = 0, \quad z = q, \quad -a/2 < x < a/2, \quad 0 < y < h \quad (C.3)$$

$$\frac{\partial}{\partial z} w = 0, \quad z = q + d, \quad -a/2 < x < a/2, \quad 0 < y < h \quad (\text{C.4})$$

$$\frac{\partial}{\partial x} w = 0, \quad x = \pm a/2, \quad q < z < q + d, \quad 0 < y < h \quad (\text{C.5})$$

$$\frac{\partial}{\partial y} w = 0, \quad y = 0, h, \quad q < z < q + d, \quad -a/2 < x < a/2 \quad (\text{C.6})$$

$$w(x, z; 0) = 0. \quad (\text{C.7})$$

We assume that the leading order temperature has reached a steady state  $v_s$ , satisfying equation (6.5), and expand  $|u_0|^2$  in equation (C.2) using the propagating mode solution for  $u_0$  derived in section (5.2.4), i.e.,

$$u_0(x, z; v_s) \approx \sum_{n=1}^M T_n e^{i\beta_n q} \left\{ f_n e^{i[\theta_n(v_s)](z-q)} + g_n e^{-i[\theta_n(v_s)](z-q)} \right\} \phi_n(x) \quad (\text{C.8})$$

where  $\phi_n(x) = \sqrt{\frac{2}{a}} \sin n\pi \left( \frac{x}{a} + \frac{1}{2} \right)$ . This transforms equation (C.2) into

$$\nabla^2 w = \frac{-2L}{d^2} - C \sum_{n=1}^M \mathcal{F}_n(z) (1 - \Upsilon_{2n}) + C \sum_{n=1}^M \sum_{m=1, (m \neq n)}^M \mathcal{Q}_{nm}(z) (\Upsilon_{n+m} - \Upsilon_{|n-m|}) \quad (\text{C.9})$$

with  $C = \frac{pf}{ad^2}$ ,  $p = \frac{-2L}{f||u_0||^2}$ ,  $\Upsilon_k = \cos[\lambda_k(x + \frac{a}{2})]$ ,  $\lambda_k = \frac{k\pi}{a}$ ,  $k = |n \pm m|$  or  $2n$ ,

$$\begin{aligned} \mathcal{F}_n(z) &= |T_n|^2 \left\{ |f_n|^2 e^{-2(\text{Im } \theta_n)(z-q)} + |g_n|^2 e^{2(\text{Im } \theta_n)(z-q)} \right. \\ &\quad \left. + 2\text{Re} \left[ f_n g_n^* e^{2i(\text{Re } \theta_n)(z-q)} \right] \right\}, \end{aligned} \quad (\text{C.10})$$

$$\begin{aligned} \mathcal{Q}_{nm}(z) &= T_n T_m^* e^{i(\beta_n - \beta_m)q} \left\{ f_n f_m^* e^{i(\theta_n - \theta_m^*)(z-q)} + g_n g_m^* e^{-i(\theta_n - \theta_m^*)(z-q)} \right. \\ &\quad \left. + f_n g_m^* e^{i(\theta_n + \theta_m^*)(z-q)} + g_n f_m^* e^{-i(\theta_n + \theta_m^*)(z-q)} \right\} \end{aligned} \quad (\text{C.11})$$

and where we have used the trigonometric identities  $\phi_n^2 = (1 - \Upsilon_{2n})/2$  and  $\phi_n \phi_m = (-1/a)(\Upsilon_{n+m} - \Upsilon_{|n-m|})$  for  $n \neq m$ .

### C.3 Solution

We let

$$w = \sum_{k=0}^{\infty} A_k(z; v_s) \Upsilon_k(x). \quad (\text{C.12})$$

Substituting this ansatz into the boundary value problem (C.2)-(C.6) determines an infinite sequence of second order linear ordinary differential equations in  $z$  for the  $A_k$  subject to zero flux conditions at the slab faces. The form of the forcing function for the  $k^{\text{th}}$  differential equation depends on  $M$  and on the values of  $m$  and  $n$  in expressions (C.10) and (C.11). Solutions for each of the  $A_k$  are superpositions of a finite number of solutions to the following two point boundary value problems:

$$\begin{aligned} \frac{d^2}{dz^2} A_0 &= -\frac{2L(v_s)}{d^2} - C \sum_{n=1}^M \mathcal{F}_n(z), \\ \frac{d}{dz} A_0(q) &= \frac{d}{dz} A_0(q+d) = 0, \end{aligned} \quad (\text{C.13})$$

$$\begin{aligned} \frac{d^2}{dz^2} A_{2n} - \lambda_{2n}^2 A_{2n} &= C \mathcal{F}_n(z), \\ \frac{d}{dz} A_{2n}(q) &= \frac{d}{dz} A_{2n}(q+d) = 0, \end{aligned} \quad (\text{C.14})$$

$$\begin{aligned} \frac{d^2}{dz^2} A_{n+m} - \lambda_{n+m}^2 A_{n+m} &= C \mathcal{Q}_{nm}(z), \\ \frac{d}{dz} A_{n+m}(q) &= \frac{d}{dz} A_{n+m}(q+d) = 0, \end{aligned} \quad (\text{C.15})$$

$$\begin{aligned} \frac{d^2}{dz^2} A_{|n-m|} - \lambda_{|n-m|}^2 A_{|n-m|} &= -C \mathcal{Q}_{nm}(z), \\ \frac{d}{dz} A_{|n-m|}(q) &= \frac{d}{dz} A_{|n-m|}(q+d) = 0, \end{aligned} \quad (\text{C.16})$$

$$\begin{aligned} \frac{d^2}{dz^2} A_k - \lambda_k^2 A_k &= 0, \quad k > 2M, \\ \frac{d}{dz} A_k(q) &= \frac{d}{dz} A_k(q+d) = 0 \end{aligned} \quad (\text{C.17})$$

where  $n, m \in (1, \dots, M)$  and  $n \neq m$ . Computations are simplified by noting that  $\mathcal{F}_n = 0$  when  $n$  is even and  $\mathcal{Q}_{nm} = 0$  when either or both of  $n$  and  $m$  are even. This is due to the fact that  $T_n = 0$  for all even  $n$ . In these cases, boundary value problems

(C.14)-(C.16) become homogeneous and, along with (C.17), admit only the trivial solution. The net result is that the odd numbered  $A_k$  are zero.

**Solution for  $A_0$ .** The solution to (C.13) is

$$A_0(z) = c_2(\tau) + v_1(z) + zv_2(z) \quad (C.18)$$

with

$$\begin{aligned} v_1(z) &= C \sum_{n=1}^M |T_n|^2 \left\{ |f_n|^2 I_n^1(z) + |g_n|^2 I_n^2(z) + 2 \left[ \delta_1 I_n^{31}(z) + \delta_2 I_n^{32}(z) \right] \right\} + \frac{L(v_s)}{d^2} (z^2 - q^2), \\ \delta_1 &= (\operatorname{Re} f_n)(\operatorname{Re} g_n) + (\operatorname{Im} f_n)(\operatorname{Im} g_n), \quad \delta_2 = (\operatorname{Re} f_n)(\operatorname{Im} g_n) - (\operatorname{Im} f_n)(\operatorname{Re} g_n), \\ I_n^1(z) &= \frac{1}{-2 \operatorname{Im} \theta_n} \left[ ze^{-2(\operatorname{Im} \theta_n)(z-q)} - q \right] - \frac{1}{(-2 \operatorname{Im} \theta_n)^2} \left[ e^{-2(\operatorname{Im} \theta_n)(z-q)} - 1 \right], \\ I_n^2(z) &= \frac{1}{2 \operatorname{Im} \theta_n} \left[ ze^{2(\operatorname{Im} \theta_n)(z-q)} - q \right] - \frac{1}{(2 \operatorname{Im} \theta_n)^2} \left[ e^{2(\operatorname{Im} \theta_n)(z-q)} - 1 \right], \\ I_n^{31}(z) &= \frac{1}{2 \operatorname{Re} \theta_n} \left\{ z \sin[2(\operatorname{Re} \theta_n)(z-q)] + \frac{1}{2 \operatorname{Re} \theta_n} (\cos[2(\operatorname{Re} \theta_n)(z-q)] - 1) \right\}, \\ I_n^{32}(z) &= \frac{1}{-2 \operatorname{Re} \theta_n} \left\{ (z \cos[2(\operatorname{Re} \theta_n)(z-q)] - q) - \frac{\sin[2(\operatorname{Re} \theta_n)(z-q)]}{-2 \operatorname{Re} \theta_n} \right\}, \\ v_2(z) &= -C \sum_{n=1}^M |T_n|^2 \left\{ \frac{|f_n|^2}{-2 \operatorname{Im} \theta_n} (e^{-2(\operatorname{Im} \theta_n)(z-q)} - 1) + \frac{|g_n|^2}{2 \operatorname{Im} \theta_n} (e^{2(\operatorname{Im} \theta_n)(z-q)} - 1) \right. \\ &\quad \left. + 2 \operatorname{Re} \left[ \frac{f_n g_n^*}{2i \operatorname{Re} \theta_n} (e^{2i(\operatorname{Re} \theta_n)(z-q)} - 1) \right] \right\} - \frac{2L(v_s)}{d^2} (z - q) \end{aligned}$$

and where  $c_2(\tau)$  can be found by imposing the solvability condition that guarantees the existence of the third order temperature  $v_2$ . The constant  $c_1$ , which multiplies the linear term originating from the homogeneous solution of (C.13), is found to be zero by applying either of the boundary conditions in (C.13). The solvability condition that guarantees the existence of  $A_0$  gives the same expression for  $\|u_0\|^2$  as obtained from its definition in terms of an integral over the slab. We note that  $A_0$  is bounded as  $\operatorname{Im} \theta_n \rightarrow 0$  since terms with  $\operatorname{Im} \theta_n$  in the denominator very nearly cancel each other, implying that  $A_0$  is close to zero throughout the slab.

**Solution for  $A_{2n}$ ,  $n = 1, \dots, M$  odd.** The solution to (C.14) is

$$A_{2n}(z) = (h^-)e^{\lambda_{2n}(z-q)} + (h^+)e^{-\lambda_{2n}(z-q)} + A_{2n}^1 + A_{2n}^2 + A_{2n}^3 \quad (\text{C.19})$$

with

$$\begin{aligned} A_{2n}^1 &= s_n e^{-2(\text{Im } \theta_n)(z-q)}, & s_n &= \frac{C|T_n|^2|f_n|^2}{(2\text{Im } \theta_n)^2 - \lambda_{2n}^2}, \\ A_{2n}^2 &= t_n e^{2(\text{Im } \theta_n)(z-q)}, & t_n &= \frac{C|T_n|^2|g_n|^2}{(2\text{Im } \theta_n)^2 - \lambda_{2n}^2}, \\ A_{2n}^3 &= \eta_1 \cos[2(\text{Re } \theta_n)(z-q)] + \eta_2 \sin[2(\text{Re } \theta_n)(z-q)], & \eta_1 &= \frac{2C|T_n|^2\delta_1}{-4(\text{Re } \theta_n)^2 - \lambda_{2n}^2}, \\ & & \eta_2 &= \frac{2C|T_n|^2\delta_2}{-4(\text{Re } \theta_n)^2 - \lambda_{2n}^2} \quad \text{where } \delta_1 \text{ and } \delta_2 \text{ are defined in the solution for } A_0, \\ h^\pm &= \frac{h_2 - h_1 e^{\pm\lambda_{2n}d}}{\lambda_{2n} \sinh(d\lambda_{2n})}, \\ h_1 &= (s_n - t_n)\text{Im } \theta_n - \eta_2 \text{Re } \theta_n, \\ h_2 &= \text{Im } \theta_n [s_n e^{-2(\text{Im } \theta_n)d} - t_n e^{2(\text{Im } \theta_n)d}] + \text{Re } \theta_n [\eta_1 \sin(2\text{Re } \theta_n d) - \eta_2 \cos(2\text{Re } \theta_n d)]. \end{aligned}$$

When the denominators in the expressions for  $A_{2n}^1$  and  $A_{2n}^2$  are zero, that is, when  $\lambda_{2n} = n_1 \nu f(v_s)$ , the solutions become

$$A_{2n}^1 = \tilde{s}_n(z-q)e^{-2(\text{Im } \theta_n)(z-q)}, \quad \tilde{s}_n = \frac{C|T_n|^2|f_n|^2}{-4\text{Im } \theta_n}, \quad (\text{C.20})$$

$$A_{2n}^2 = \tilde{t}_n(z-q)e^{2(\text{Im } \theta_n)(z-q)}, \quad \tilde{t}_n = \frac{C|T_n|^2|g_n|^2}{4\text{Im } \theta_n} \quad (\text{C.21})$$

where  $\tilde{s}_n$  and  $\tilde{t}_n$  replace  $s_n$  and  $t_n$  in the remaining terms of (C.19). The large terms generated by  $\tilde{s}_n$  and  $\tilde{t}_n$  when  $\text{Im } \theta_n \ll 1$  very nearly cancel each other so that the solution (C.19) remains bounded as  $\text{Im } \theta_n \rightarrow 0$ . This behavior dictates that there is no resonant temperature condition. Furthermore, the factor  $(z-q)$  in (C.20) and (C.21) does not introduce any appreciable change in the qualitative behavior of the solution for  $A_{2n}$ .

**Solutions for  $A_{n+m}$  and  $A_{|n-m|}$ ,  $n, m = 1, \dots, M$  odd,  $n \neq m$ .** The solutions to (C.15) and (C.16) are

$$A_{|n\pm m|} = (J_1^\pm) e^{\lambda_\pm(z-q)} + (J_2^\pm) e^{-\lambda_\pm(z-q)} + \sum_{j=1}^4 A_j^\pm(z) \quad (C.22)$$

where the + and - superscripts and subscripts correspond to  $n + m$  and  $|n - m|$  respectively. The quantities in (C.22) are

$$\begin{aligned} A_j^\pm(z) &= e^{-(\text{Im } \Theta_j)(z-q)} \left\{ R_{1j}^\pm \cos[(\text{Re } \Theta_j)(z-q)] + R_{2j}^\pm \sin[(\text{Re } \Theta_j)(z-q)] \right\}, \\ R_{1j}^\pm &= \frac{\pm \mathcal{L}_j [\lambda_\pm^2 - (\Theta_j^*)^2]}{\Delta_j^\pm}, \\ R_{2j}^\pm &= \frac{-i(\pm \mathcal{L}_j) [\lambda_\pm^2 + (\Theta_j^*)^2]}{\Delta_j^\pm}, \\ \Delta_j^\pm &= [(\text{Im } \Theta_j)^2 - (\text{Re } \Theta_j)^2 - \lambda_\pm^2]^2 + 4(\text{Im } \Theta_j)^2 (\text{Re } \Theta_j)^2, \\ J_1^\pm &= \frac{e^{-(\lambda_\pm)d} (S_1^\pm) - S_2^\pm}{2(\lambda_\pm) \sinh(d\lambda_\pm)}, \\ J_2^\pm &= \frac{e^{(\lambda_\pm)d} (S_1^\pm) - S_2^\pm}{2(\lambda_\pm) \sinh(d\lambda_\pm)}, \\ S_1^\pm &= \sum_{j=1}^4 (-R_{1j}^\pm \text{Im } \Theta_j + R_{2j}^\pm \text{Re } \Theta_j), \\ S_2^\pm &= \sum_{j=1}^4 e^{-(\text{Im } \Theta_j)d} \left\{ (-R_{1j}^\pm \text{Im } \Theta_j + R_{2j}^\pm \text{Re } \Theta_j) \cos[(\text{Re } \Theta_j)d] \right. \\ &\quad \left. + (-R_{1j}^\pm \text{Re } \Theta_j - R_{2j}^\pm \text{Im } \Theta_j) \sin[(\text{Re } \Theta_j)d] \right\} \end{aligned}$$

with

$$\mathcal{L}_1 = \zeta_{nm} f_n f_m^*, \quad \mathcal{L}_2 = \zeta_{nm} g_n g_m^*, \quad \mathcal{L}_3 = \zeta_{nm} f_n g_m^*, \quad \mathcal{L}_4 = \zeta_{nm} g_n f_m^*,$$

$$\zeta_{nm} = CT_n T_m^* e^{i(\beta_n - \beta_m)q},$$

and

$$\Theta_1 = \theta_n - \theta_m^*, \quad \Theta_2 = -(\theta_n - \theta_m^*), \quad \Theta_3 = \theta_n + \theta_m^*, \quad \Theta_4 = -(\theta_n + \theta_m^*).$$

The solutions for  $A_0$  and  $A_{2n}$  are real. The solutions for  $A_{|n\pm m|}$  are complex, but occur in conjugate pairs so that superposition of the  $A_k$ 's for each  $k = 0, \dots, 2M$  determines a real  $w$  in accordance with (C.12). Finally, the complete solution for  $v_1$  is determined from (C.1).

## REFERENCES

1. J. Mobley, L. Lakemacher, M. DeMent, L. Foister editors, *The American Ceramic Society: 100 years*, American Ceramic Society, Westerville OH, 1998.
2. L. Feher, *Industrial materials processing: materials processing dynamics*, Abstract of seminar given at New Jersey Institute of Technology, 1998.
3. J. Svoboda, H. Riedel, *Pore-boundary interactions and evolution equations for the porosity and the grain size during sintering*, *Acta Metall.*, 40, 2829, 1992.
4. K.G. Ayappa, A. Chatterjee, T. Basak, *Analysis of microwave sintering of ceramics*, *AIChE Journal*, vol. 44(10), 2302-2311, 1998.
5. G.A. Kriegsmann, *Microwave heating of ceramics: a mathematical theory*, in *Microwaves: Theory and Applications in Materials Processing*, edited by D.E. Clark, F.D. Gac and W.H. Sutton, *Ceramic Transactions* 21 (American Ceramic Society, Cincinnati, OH, 1991), 117-183.
6. G.A. Kriegsmann, *Thermal runaway in microwave heated ceramics: a one-dimensional model*, *Journal of Applied Physics*, vol. 71(4), 1960-1966, 1992.
7. G. Kriegsmann, *Cavity effects in microwave heating of ceramics*, *SIAM Journal of Applied Mathematics*, vol. 57(2), 382-400, April 1997.
8. G.A. Kriegsmann, C. Hile, *A hybrid numerical method for loaded highly resonant single mode cavities*, *Journal of Computational Physics*, vol. 142, 1998.
9. A.C. Metaxas, R.J. Meredith, *Industrial Microwave Heating*, Peter Peregrinus Ltd., London, 1988.
10. , F. Liu, I. Turner, M. Bialkowski, *A finite difference time-domain simulation of power density distribution in a dielectric loaded microwave cavity*, *Journal of Microwave Power and Electromagnetic Energy*, vol. 29(3), 138-148, 1994.
11. M.F. Iskander, M. Subirats, M.J. White, J.O. Kiggans, Jr., *FDTD simulation of microwave sintering in large(500/4000 liter) multimode cavities*, *Journal of Microwave Power and Electromagnetic Energy*, vol. 32(3), 161-170, 1997.
12. M.J. White, M.F. Iskander, Z. Huang, H.D. Kimrey, *A three dimensional multi-grid FDTD code for modeling microwave sintering of materials*, *IEEE Antennas and Propagation International Symposium*, Baltimore MD, vol. 1, 120-122, 1996

13. W. Fu, A. Metaxas, *Numerical prediction of three dimensional power density distributions in a multi-mode cavity*, Journal of Microwave Power and Electromagnetic Energy, vol. 29(2), 67-75, 1994.
14. W. Fu, A. Metaxas, *Numerical solution of Maxwell's equations in three dimensions using the method of lines with applications to microwave heating in a multi-mode cavity*, International Journal of Applied Electromagnetics and Mechanics, vol. 6, 165-186, 1995.
15. H. Zhao, I. Turner, F. Liu, *Numerical simulation of the power density distribution generated in a multimode cavity by using the method of lines technique to solve directly for the electric field*, IEEE Transactions on Microwave Theory and Techniques, vol. 44(12), 2185-2194, 1996.
16. R. Cravey, R. Sternlicht, C. Ryan, *Finite element analysis of overmoded waveguide using Silvester's algorithm*, IEEE Trans MTT-35, 205-206, 1987.
17. D. Rodger, *Finite element method for calculating power frequency 3-D electromagnetic field distributions*, IEE Proc. vol. 130 part A (5), 233-238, 1983.
18. X. Jia, P. Jolly, *Simulation of microwave field and power distribution in a cavity by a three dimensional finite element method*, Journal of Microwave Power and Electromagnetic Energy, vol. 27, 11-22, 1992.
19. W.B. Fu, *An analytical study of the propagation of microwaves through a dielectric-filled waveguide*, Cambridge University Electrical Engineering Department Report, February 1993.
20. F. Paolini, *Calculation of power deposition in a highly overmoded rectangular cavity with dielectric loss*, Journal of Microwave Power and Electromagnetic Energy, vol. 24(1), 21-32, 1989.
21. Z. Shou-Zheng, C. Han-Kui, *Power distribution analysis in rectangular microwave heating applicator with stratified load*, Journal of Microwave Power and Electromagnetic Energy, vol. 23(3), 139-143, 1988.
22. R.J. Meredith, *A three axis model of the mode structure of multi-mode cavities*, Journal of Microwave Power and Electromagnetic Energy, vol. 29(1), 31-44, 1994.
23. L. Feher, G. Link, M. Thumm, *Microwave raytracing in large overmoded industrial resonators*, Proc. Meeting American Ceramic Society, Microwaves: Theory and Application in Materials Processing III Symposium, Cincinnati, 1995.
24. L. Feher, G. Link, M. Thumm, *Theoretical aspects of microwave raytracing calculations in screened structures*, Proc. Latsis Symposium on Computational Electromagnetics, Zurich, 236-241, Sept 19-21, 1995.

25. W.D. Kingery, H.K. Bowen, D.R. Uhlman, *Introduction to Ceramics*, Wiley, New York, 1976.
26. G. Strang, *Linear Algebra and Its Applications*, 3rd edition, Harcourt Brace Jovanovich, Orlando FL, 1988.
27. N. Amitay, V. Galindo, *On energy conservation and the method of moments in scattering problems*, IEEE Transactions on Antennas and Propagation, vol. 17(6), 747-751, 1969.
28. G. Kriegsmann, *The Galerkin approximation of the iris problem: conservation of power*, Applied Mathematics Letters, vol. 10(1), 41-44, 1997.